Chem Soc Rev

REVIEW ARTICLE

View Article Online
View Journal

Cite this: DOI: 10.1039/c5cs00350d

Characterisation of gold catalysts

Alberto Villa,[a] Nikolaos Dimitratos,[b] Carine E. Chan-Thaw,[a] Ceri Hammond,[b] Gabriel M. Veith,[c] Di Wang,[d] Maela Manzoli,[e] Laura Prati[a] and Graham J. Hutchings*[b]

Au-based catalysts have established a new important field of catalysis, revealing specific properties in terms of both high activity and selectivity for many reactions. However, the correlation between the morphology and the activity of the catalyst is not always clear although much effort has been addressed to this task. To some extent the problem relates to the complexity of the characterisation techniques that can be applied to Au catalyst and the broad range of ways in which they can be prepared. Indeed, in many reports only a few characterization techniques have been used to investigate the potential nature of the active sites. The aim of this review is to provide a critical description of the techniques that are most commonly used as well as the more advanced characterization techniques available for this task. The techniques that we discuss are (i) transmission electron microscopy methods, (ii) X-ray spectroscopy techniques, (iii) vibrational spectroscopy techniques and (iv) chemisorption methods. The description is coupled with developing an understanding of a number of preparation methods. In the final section the example of the supported AuPd alloy catalyst is discussed to show how the techniques can gain an understanding of an active oxidation catalyst.

Received 29th April 2015

DOI: 10.1039/c5cs00350d

www.rsc.org/chemsocrev

1. Introduction

Au exploded in importance for the field of catalysis with the discovery in the 1980s of its activity in two fundamental reactions, namely the oxidation of CO to CO_2 and the hydrochlorination of ethylene.[1–3] The use of Au in catalysis has now been extended to many reactions such as the oxidation of alcohols and aldehydes, hydrogenation of aldehydes, epoxidation of propylene, and carbon–carbon bond formation.[4–15] Despite progress on all these reactions a fundamental problem has remained stubbornly unsolved, *i.e.* the variability of catalyst activity with synthesis and processing. This variability results from different catalyst structures.[16–19]

The aim of this review is to help to capture a range of unique information obtained from a number of analytical methods which when combined could offer an improved understanding of the structure and reactivity of Au catalysts. This review will include transmission electron microscopy (TEM), X-ray photoelectron spectroscopy (XPS) and X-ray absorption spectroscopy (XAS), ultraviolet-visible (UV-Vis), Fourier transform infra-red (FTIR) spectroscopies, Raman spectroscopy and chemisorption techniques. It is important to realise why these characterisation methods are necessary and when they are required. We are not advocating that all catalysts are extensively characterised. This is not the case as it is important only to expend such efforts only when an active catalyst has been identified. We then suggest that by the appropriate selection of techniques a more detailed understanding of the origin of the catalysis can be attained. The purpose of this review is to introduce the most commonly used techniques used in the study of heterogeneous catalysis and using Au catalysts as the vector demonstrate the principles of the techniques and how they can be used to positive effect. Although many more techniques have been used in the study of heterogeneous catalysis (*e.g.* electron paramagnetic resonance and Mössbauer spectroscopy) we have not tried to be comprehensive as many techniques have not been extensively applied in the study of Au catalysts.

TEM is an important tool to investigate metal nanoparticle morphology, including size, shape as well as the effect of the metal support interaction.[20–22] XPS and XAS provide information on the catalyst surface, including the Au oxidation state, support oxidation state, particle stability, and catalyst electronic structure.[23,24] UV-Vis spectroscopy is a fundamental tool to

---

[a] *Dipartimento di Chimica, Università degli studi di Milano, via Golgi 19, 20133, Milano, Italy*
[b] *School of Chemistry, Cardiff University, Main Building, Park Place, Cardiff, CF103AT, UK. E-mail: Hutch@cardiff.ac.uk*
[c] *Materials Science and Technology Division, Oak Ridge National Laboratory, Oak Ridge, TN 37831, USA*
[d] *Institute of Nanotechnology and Karlsruhe Nano Micro Facility Karlsruhe Institute of Technology (KIT), Hermann-von-Helmholtz-Platz 1, 76344 Eggenstein-Leopoldshafen, Germany*
[e] *Dipartimento di Chimica, Università degli Studi di Torino, Via Pietro Giuria 7, 10125, Torino, Italy*

investigate the oxidation state of Au but also can give information of Au size and shape and the optical properties.[6] FTIR spectroscopy represents a powerful technique to examine the coordination of the surface Au sites at an atomic level. In particular, the analysis of FTIR spectra of adsorbed probe molecules allows an understanding of the nature and abundance of the exposed active sites as well as to have detailed information on their structure and chemical environment.[25,26] Chemisorption measurements are of primary importance for scientists studying reaction mechanisms, since the proper interpretation of heterogeneously catalysed reaction kinetics requires a precise knowledge of the number of active atoms exposed on the surface.[27,28] Raman spectroscopy can give information on the properties and the surface morphology of the metallic Au nanoparticles.[29,30] Lastly, we will provide a summary of bimetallic Au–Pd catalysts for alcohol oxidation paying a particular attention to the correlation between structure and activity of the active sites. The correct selection and use of the appropriate techniques can provide a powerful toolbox to characterise in depth Au-based catalysts and understand the role of metal precursor, solvent, heat treatment effect and support for controlling the final stage of the nanoparticle morphology in terms of particle size, oxidation state and metal support interaction. In the final section we show how this can be achieved using supported AuPd catalysts as an example.

Dr Alberto Villa is an Assistant Professor at the University of Milan. He received his PhD in Industrial Chemistry in 2007 from the University of Milan, where his thesis focused on the development of gold-based catalysts for liquid phase reactions. After a Post doc at the Fritz Haber Institute of Berlin (2008–2009), he accepted a position at the University of Milan. His current research focuses on the development of noble metal free heterogeneous catalysts for biomass transformation. He has (co)authored over 70 publications in peer-reviewed journals.

Dr Nikolaos Dimitratos studied chemistry at the University of Bath and received a PhD at the University of Liverpool in 2003. He was a postdoctoral researcher at the University of Milan and Cardiff University. His current research field is catalysis, covering areas of synthesis, characterisation and reactivity in oxidation and hydrogenation reactions. He is currently University Research Fellow in the area of catalysis and nanoparticle synthesis at Cardiff University.

Dr Carine E. Chan-Thaw is an assistant a Research Fellow at the University of Milan. Her PhD research was carried out at the Fritz Haber Institute under the supervision of Prof. Robert Schlögl. She received a European PhD in Chemistry, 2008, from both the Université de Strasbourg and the Technische Universität Berlin. She accepted a Post-doctoral fellowship at the Technische Universität Berlin where she worked on testing nitrogen rich highly porous framework for liquid phase oxidations. She is currently investigating on the valorization of biomass.

Dr Ceri Hammond received his PhD from Cardiff University in 2012. After a Post doc at ETH Zürich (2011–2014), he accepted a position at the Cardiff Catalysis Institute as a University Research Fellow. Since October 2014, he also holds dual affiliation as a RSC Research Fellow at Stanford University. His research team specializes in several aspects of applied catalysis, inorganic materials, and in situ spectroscopy.

Dr Gabriel M. Veith is a R&D Staff member at the Oak Ridge National Laboratory in the Materials Science and Technology Division. He received his PhD in Chemistry in 2002 from Rutgers University in New Jersey focusing on the synthesis and characterization of layered high-oxidation state iron compounds. His current research focuses on understanding interfaces in energy storage and conversion materials such as catalysts and batteries and the development of new synthesis methodologies.

Dr Di Wang received his PhD in 2001 with Prof. Fanghua Li from institute of Physics, Chinese Academy of Sciences. From 2001 to 2009, he worked as postdoctoral researcher with Prof. Schlögl in Fritz Haber Institute of the Max Planck Society for TEM characterization of heterogeneous catalysts to understand the correlation between structure and catalytic behaviors. Since 2009, he has worked as research scientist in Institute of Nanotechnology and Karlsruhe Nano Micro Facility (KNMF), Karlsruhe institute of Technology. His research activities are focused on using aberration corrected HRTEM techniques, high spatially resolved EDX and EELS spectroscopy, HAADF STEM and tomography for the structural characterization on a wide range of nanomaterials, particularly supported nanocatalysts. He has (co)authored over 80 publications in peer-reviewed journals.

Dr Maela Manzoli is a Research Technician, she joins the Department of Chemistry of the University of Turin. She received her PhD in Chemistry in 2001. She developed her skills in the study of the surface properties of supported metal nanoparticles as well as in their textural, morphological and structural characterization. She is coauthor of more than 75 papers in peer-reviewed journals.

Prof. Laura Prati is an Associate Professor of Inorganic Chemistry at the Università degli Studi di Milano since 2001. She received her specialisation in "Tecniche Analitiche per la Chimica Organica Fine" from the Politecnico of Milano in 1985 and was awarded a PhD in Industrial Chemistry in 1988. She was awarded a PhD in Industrial Chemistry in 1988. She is applying from several years to low impact environmental catalytic methodologies as alternative processes of the stoichiometric ones based on organic synthesis. Her scientific interests focus principally on specific design of heterogeneous catalysts.

Professor Graham J. Hutchings FRS has specialised in the field of heterogeneous catalysis for over 40 years. During his initial industrial career with ICI Petrochemicals (1975–1981) and AECI Ltd (1981–1984) he made initial discoveries on gold catalysis. Since 1984 he has been involved in academic research and has published over 600 papers and patents. He was elected as a Fellow of the Royal Society in 2009. He is currently Professor of Physical Chemistry and Director of the Cardiff Catalysis Institute at Cardiff University.

2. Characterization tools

2.1 Transmission electron microscopy advances applied to Au catalysts

With the fast development of TEM it has become a routine and very important technique for the catalyst characterization, especially complementary to other *in situ* and *ex situ* spectroscopic techniques. Its value is the study of the structure of catalysts at different spatial scale from atomic level to macro reactor as well as different time scale from elementary steps on the single active site to the life cycle in a real reactor.[31] The correlation between the structures down to an atomic level with the activity and selectivity of the catalyst are expected to ultimately lead to the capability of tailoring the highly efficient multi-functional and synergistic catalysts. High-resolution transmission electron microscopy (HRTEM) and high angle annular dark field (HAADF) STEM images can reveal the atomic configurations of small particles with state of the art spherical aberration corrector[32,33] for the objective lens and/or for the probe forming lens. With elastically scattered electrons by a crystal, an HRTEM image directly reflects the lattice structures of metal particles. Specifically, crystallinity, phases and crystallographic orientations of the sample, as well as the defection of structures such as dislocation, planar defects and interface, and cluster configuration can be readily resolved.[34] Surface facets and features such as roughness and decoration by other species can also be resolved by profile imaging.[35] In the STEM mode, the electron beam is focused to a sub-nm probe on the sample and the electrons, which are scattered to a certain range of solid angles after interacting with the specimen, can be selectively detected. The image is then formed by scanning the beam in a certain area with collected electron signals representing the intensity for each scanned point. When the collection angle is high, typically >100 mrad, HAADF STEM image is obtained where the intensity of the image can be directly correlated to the atomic number and sample thickness along beam direction forming so called "*Z*-contrast" image.[36] Therefore, there is large contrast between a low *Z* support like carbon and a high *Z* material *i.e.* Au. Combining HRTEM and STEM data can provide insights to the morphology, crystal structure, surface modification and capping, disordering due to defects or metal–support interaction.

On state of the art instruments energy dispersive X-ray spectroscopy (EDX) and electron energy-loss spectroscopy (EELS) can be acquired simultaneously. This provides chemical specificity to identify atoms and the electronic structure/oxidation state of the catalyst and support. Recently, combining probe corrected STEM and in column silicon drift detector[37] has improved the spatial resolution and detector efficiency greatly so that core–shell structures, segregations and random alloys within individual particles can be unambiguously distinguished.

2.1.1 Statistical size measurement of Au nanoparticles. Au materials that are used as heterogeneous catalysts usually consist of a support and Au nanoparticles. With small particle sizes (<10 nm), classical particle size measurements using the Sherrer-equation fitting X-ray diffraction is unreliable due to the broad reflections and statistical averaging, which makes the measurement of the size distribution difficult. Therefore, high-resolution TEM and STEM are more suitable methods since they offer the direct measurement of the particle size and particle dispersion based on electron micrographs. Due to its high contrast, HAADF STEM has become the more preferred imaging mode for particle size measurement and electron tomography.[38] HRTEM usually reveals various nanoparticle types, *e.g.* single crystal *vs.* multiply twinned and well faceted *vs.* rough surface, in a catalyst. Several quantitative analytical methods have been developed to precisely describe the particle morphology, *e.g.*, by integrating the intensity from the area of cluster to quantify the number of atoms in it, or by the blurring propagation method.[39,40] Particularly, the blurring propagation method is useful in analysing low-dose STEM images. It smooths the noise in an image by artificially broadening it with a Gaussian distribution function, which may take various standard deviation values, σ_{gb}. By fitting the particle intensity profile after blurring also with a Gaussian function and plotting the measured standard deviation σ_{meas} *vs.* the various σ_{gb}, the pure contribution from the particle can be extracted after deconvoluting the beam spread function. Additionally, conventional size measurement relying solely on the diameter determined from the projected 2D image is not sufficient to reflect any deviation from spherical shape, *e.g.*, flattening of the particle due to wetting. With the development of probe aberration corrected STEM, even single metal atoms or small clusters consisting of few atoms can be resolved.[41]

2.1.2 Crystal structure of Au nanoparticles. Bulk Au has a face centered cubic (fcc) structure. It can be envisaged as sequential stacking of close packed atomic planes along the [111] direction. Changes in this sequence leads to formation of a stacking fault or twin boundary in a nanoparticle. Since twinning does not change the interatomic distance between the nearest atoms at the twin boundary, the formation energy of a twin boundary is very small therefore twinning and de-twinning take place easily in Au crystals. The equilibrium shape of a Au particle in vacuum is determined by the minimum total surface free energy of the crystal with a given volume. The resultant shape is well known as the Wulff construction[42,43] for a large single crystal particle. When the particle size decreases, the structure becomes much more complicated than that expected from equilibrium considerations.[43] Firstly, with decreasing particle size, the energy of edge and corner atoms becomes more dominant since the facet area shrinks along with the particle size. Secondly, (111) faceting becomes more favorable at the expense of (100) and (110) facets, which leads formation of multiply twinned particles, *e.g.* decahedra and icosahedra,[44,45] when the gain in free surface energy is enough to compensate the extra energy introduced due to twin boundaries and distortion. Furthermore, for supported nanoparticles, the influence from interface and perimeter atoms is of more importance. Adsorbents can also change the morphology of the metal particles.

With these complicating factors, Au nanoparticles exhibit various shapes. Generally cuboctahedron, decahedron and icosahedron, as well as various combinations and modified types based on these, are the mostly observed.[44,46] Cuboctahedral particle is a single crystal and can be recognized by eight triangular {111} facets and six square {100} facets. A decahedral particle consists of five tetragonal parts of fcc Au, which are joined together around a five-fold zone axis along one sharing edge from each tetragon in ⟨110⟩ direction. Such a decahedron then has all its exposed surface as {111} facets. As a requirement of an exact five-fold symmetry, the angle between the neighboring twinning interface need to be 72°, while the angle between two {111} planes is 70.53°. Obviously, a decahedral particle is strained and the strain increases with the increasing radius.[47] Therefore a decahedral particle is not favored in energy when its size is above certain diameter. Very often, truncation takes place close to the outermost twinning interface to reduce its area therefore to lower the strain. Icosahedral particles can be built by twenty tetrahedra with all of them sharing one apex in the center of the particle. It is also distorted compared to fcc lattice, but in a more complicated way due to more twin boundaries, more possibilities of truncation and unequally sized tetragonal components. Depending on the projection direction, either HRTEM image or nanodiffraction may reflect the 2-fold, 3-fold and five-fold symmetry of the particle along different directions. Schematic diagrams of these three basic types of Au particle configuration are shown in Fig. 1a–c and the corresponding HRTEM images by aberration corrected TEM are shown in Fig. 1d–f.

Since the structure of most of Au nanoparticles are much more complicated than single crystal fcc structure, the interpretation of HRTEM images of the randomly oriented particles are not straightforward. Very often two or more twinning components, with one sitting on another along the electron projection direction, may lead to artificial lattice spacings and the angle between lattice planes, which arise from the interference of lattices in different twinning components but not representing the true lattice structure in the crystal. An example of such artifacts has been shown previously,[48] where the angle between the two sets of (111) planes was *ca.* 56° instead of *ca.* 71° as expected in an fcc single crystal. Image simulation based on the modeled structure indicates that such lattice characteristics are produced by two overlapping fcc lattices forming a twin boundary in between.

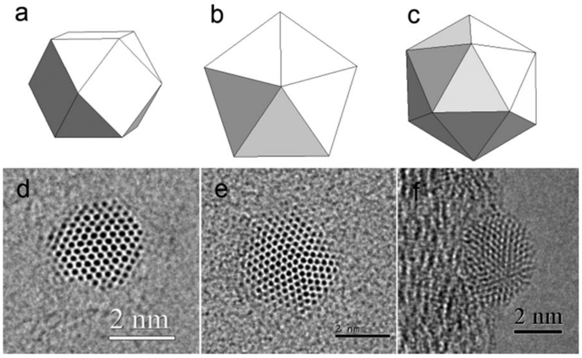

Fig. 1 Schematic diagrams (a–c) and corresponding experimental images (d–f) of three basic types, *i.e.*, cuboctahedron, decahedron and icosahedron, of Au particle configuration.

In the case of icosahedral particles, the lattice fringes in HRTEM images are even more complicated, especially when the particle is on random orientation other than the symmetric axes. HRTEM simulation is very useful to determine the structure of a multiply twinned particle. The simulation results of metals particles on a number of projections have been nicely published in ref. 45 and 49. The structures of real Au catalyst particles are further complicated by truncating the tetrahedron to form new exposed edges and by formation of steps, kinks and even isolated atoms on the surface. Moreover, for small clusters and particles, the structure can be deformed from the highly symmetric shape to form disordered structural isomers. All these structural features, which make nanoparticles so different from just large flat facets, should be taken into consideration when correlating the structures with their catalytic behavior.

2.1.3 Interface and surface structures of supported Au nanoparticles. Au nanoparticles can be synthesized on supports such as TiO_2, Al_2O_3, SiO_2, Fe_2O_3, CeO_2, carbon, nitrides, sulfides, sulfates and phosphates. Using methods such as impregnation, sol immobilization, and vacuum evaporation.[50–55] The resulting properties vary significantly depending on the synthesis method and subsequent processing. The classic explanation of a "size effect" is not sufficient to explain the catalytic behavior of supported Au particles.[56–60] This implies that the activity is determined by specific sites either on the Au surface or on the interface between Au and support. Recently, it has been reported that CO adsorption is the same for Au monolayer islands and extended Au surfaces. It is suggested that the difference in activity comes from uncoordinated Au sites.[61] The number of such sites will be strongly dependent on the shape and the roughness of the particle; the support properties may also have marked influence in terms of an electronic modification or stabilization/promotion of a particular active binding site. There are also experiments and theoretical calculations showing that Au adatoms and clusters on ultrathin oxide films on metal substrates can be charged either positively or negatively depending on the work function between oxide and metal substrate.[62] The charged Au atoms form regular array due to electrostatic repulsion. This effect may deeply modify the structures, therefore properties of the supported species.

In order to understand the metal support interaction and its effects on catalyst activity, HRTEM and HAADF STEM have been widely used to explore the atomic structure at the metal support interface using profile imaging.[35,50,51,63] This technique observes the outermost part of the supported catalysts in TEM, normally avoiding overlapping with other crystallites and carbon film from TEM grid, and to image the interface being parallel to the electron beam as well as the surface configurations. Importantly, the application of image corrector is able to eliminate the phenomenon known as "delocalization"[64] to provide electron micrographs where interface configuration can be sharply resolved. One must be aware that the profile image shows projected structure. It is not straightforward to distinguish whether the imaged surface of a particle is an edge of two intersected facets or is a real terminating plane which is parallel to the beam. Considering this issue, HAADF STEM image has the advantage that the intensity of an atom column can be quantified to obtain the number of the atoms in one column therefore the shape of nanoparticles can be determined. With HRTEM, image simulation is often helpful to verify the constructed interface model.[65,66]

The equilibrium shape of a supported macroscopic crystal is defined by the surface energy of the facets and the interaction with the substrate as quantified by the adhesion energy.[42] In addition, the adsorption of foreign atoms or molecules, and the presence of strain at the interface due to a misfit between the lattices of the support and of the deposited crystal further modify the shape of the supported particles. The adsorbed molecules often reduce the anisotropy of the particle and leads to a more spherical shape.[67,68] Au particles synthesized in existence of protective agent clearly show the decoration of the residue on the particle surface, even after washing the catalysts under mild conditions.[69] The residual protective agent was also observed to decorate on the perimeters at the interface, which could assist the adhesion of particles to the support. In contrast, Au particles deposited on polished TiO_2 surfaces by vacuum evaporation show different interface structure dependent on the particle size. For the particle smaller than a few nanometers, Au atoms preferentially attach to specific sites on TiO_2 surface and form an epitaxial hetero interface. As the Au size becomes larger, the Au–TiO_2 interface loses lattice coherency in order to accommodate the large lattice mismatch between the two dissimilar crystals.[51]

Carbon-based materials, *e.g.* activated carbon, carbon nanotubes (CNTs) and carbon nanofibers (CNFs) have been widely used as catalyst support as it is possible to manipulate them by specific chemical and thermal treatments aimed to tune the surface chemistry. Theoretical studies on the interaction between Au clusters and graphite show that the stability and the structure of Au are highly dependent on the Au cluster size and the defects on graphitic layers.[70–72] The exact type of carbon support exerts a great influence on the catalytic properties even when the Au particles are preformed by a sol-immobilization method.[73] Therefore, the preformed nanoparticles offer an ideal initial structure to investigate the structural modification introduced by different carbon support. Colloidal Au nanoparticles preformed with polyvinyl alcohol (PVA) as the stabilising agent were supported on two types of carbon nanofibers with different degree of graphitization. The investigation of these materials with an aberration corrected transmission electron microscopy showed that the degree of the surface graphitization greatly influences the structures of the supported Au particles. As shown by the HRTEM images in Fig. 2, the more ordered graphitic layers of the carbon nanofiber surface lead to Au particles being preferentially immobilized on the {111} plane, and exhibiting more facet area. On the contrary, a disordered carbon nanofibers surface leads to random orientation of supported particles. Hence, this leads to similarly sized Au nanoparticles with different morphology supported on very similar supports, and this permits the determination of the effect of support surface structures on the particle shape. Investigation of the selectivity of these catalysts in the liquid phase oxidation of glycerol, highlighted the higher C_1 and C_2 product selectivity on the Au{111} surface, which involves C–C bond cleavage.[68] With this we can obtain new insights into the well-known effect of Au nanoparticle size on the selectivity of this reaction, the larger particles with larger faceted surfaces being more selective to C_1 and C_2 products than the smaller ones. Moreover, tubular CNFs show an advantage of presenting nanostructured surfaces of different nature for the internal surface and the external one.[74–77]

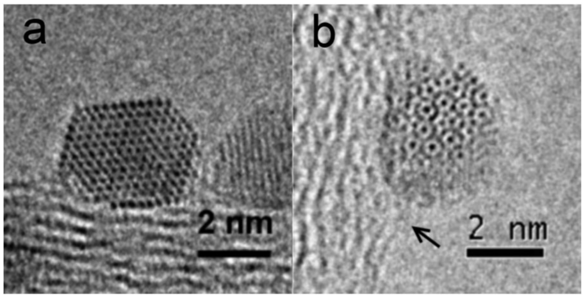

Fig. 2 Aberration corrected HRTEM images of Au particles supported on CNFs. (a) Au particle exhibits (111) facets epitaxially parallel to the ordered graphitic layer; (b) Au particle exhibits rough surfaces on the disordered graphitic surface of CNFs. Adapted with permission from ref. 68. Copyright 2013 Wiley-VCH Verlag GmbH & Co. KGaA, Weinheim.

On CNFs functionalized with nitrogen species,[72,73] Au nanoparticles synthesized by sol immobilization (SI) and incipient wetness impregnation (IW) were selectively deposited exclusively outside and in-/outside of carbon nanofibers respectively with a significant effect of their catalytic performance in both gas and liquid phase reactions.[74–76]

The presence of the capping agent (PVA) increases the hydrodynamic radius of the particles (20–30 nm), thus limiting their internal diffusion inside the channel (diameter 20–50 nm). On the contrary, incipient wetness impregnation forces the Au precursor to enter the N-CNFs channel, interacting mainly with the inner surface. Small nanoparticles with a similar mean diameter of 3.2–3.4 nm were observed on the two catalysts. In order to confirm the resultant structures by selective deposition, HAADF STEM electron tomography was used to study the 3D structure of carbon nanofiber supported Au catalysts synthesized by SI and IW procedures.

HAADF STEM tomogram was reconstructed from tilt series images in a tilting angle range between at least $\pm 70^\circ$ with a step of 2°. From the cross-sectional slice intersecting a few particles on the representative CNFs for each catalyst, it was clearly visualised that for the impregnated Au/CNFs particles were found both inside and outside the CNFs, while for Au(PVA)/CNFs, particles were found exclusively on the outer surface of the CNFs. From these comparative studies a confinement effect has been demonstrated where Au nanoparticles trapped within N-functionalized carbon nanofibers (N-CNFs) are more active for polyol oxidation and promote selectivity towards di-acid products whereas Au nanoparticles (AuNPs) trapped on the outer surface show as major by-products derived from C–C cleavage. The behaviour of NPs confined inside N-CNFs channels can be assigned to the frequent collisions as well as to different electron density.[78,79]

As a vacuum is present in most electron microscopes, it is challenging to study the morphology of nanoparticles in different atmospheres at an elevated temperature. Environmental TEM (ETEM) therefore has been developed to bridge this gap and to explore the "real" structure of catalysts under reaction conditions. In general there are two types of apparatus to perform environmental TEM experiments. One is based on a closed cell TEM holder[80,81] and the other is based on differential pumping scheme.[82] For the closed cell, specially designed TEM holder allows gas or liquid to be injected onto the catalyst specimen enclosed between two thin electron transparent windows (*e.g.* C or SiN), which are separated by spacer of appropriate size. This setup allows a gas pressure up to 1 bar, as well as the observation of catalyst in liquid environments. The other setup is to construct dedicated ETEM by modifying the column. In this case, the gas pressure is usually controlled below 3000 Pa in the vicinity of the sample.[83]

Au nanoparticles on different supports exposed to various atmospheres have been studied with ETEM. For CO oxidation on Au/CeO_2, with 1 vol% CO in 1 mbar CO/air, Au particles showed well faceted surfaces. In pure O_2, the particle tended to be round. This trend was also observed that the particle became less faceted with decreasing the CO partial pressure. In contrast, the morphology of Au/TiC, which is not active in CO oxidation, seemed to be unaffected by the gas environments.[84] Au/TiO_2 exhibited dynamically changed morphology during CO oxidation in a windowed environmental cell.[85] The application of aberration corrected ETEM has achieved atomic resolution for surface reconstruction due to the presence of CO molecules.[86] More and more application of ETEM techniques will undoubtedly provide unique structural information under reaction conditions therefore will help unravelling the origin of Au special catalytic properties.

2.1.4 Structure of Au-based bimetallic catalysts. Alloying Au with a second metal, or even by more metals, has greatly increased the possibilities to tailor the structure and therefore, potentially, the reactivity of the catalysts. The structural complexity increases at the same time. In addition to particle size and shape, the composition, distribution and surface ordering should be taken into consideration as all can affect the activity, selectivity and stability of the catalysts. In order to correlate specific sites on the bimetallic materials to catalytic properties, it is necessary to characterize the catalyst at nano scale or even at the atomic scale. Efforts have been dedicated to synthesize different types of bimetallic nanoparticles and to characterize them with a range of experimental techniques such as, X-ray absorption spectroscopy including both extended X-ray absorption fine structure (EXAFS) and X-ray near edge structure (XANES) and advanced TEM techniques.[87–94] It has been revealed that the structure of bimetallic catalysts is dependent on the support materials, the synthesis procedures and the post preparation treatment. Therefore it is important to follow the synthesis of the catalyst from the initial to the final stage.[88,90,92,95] Inhomogeneity in composition and distribution is usually related to the ratio of alloyed metals and the specific particle size.

For example, for the catalysts prepared by co-impregnation of the supports using incipient wetness with aqueous solutions of $PdCl_2$ and $HAuCl_4$ with calcination at 400 °C, the Au–Pd particles on TiO_2 and Al_2O_3 as supports were found to exhibit a core–shell structure, Pd being concentrated on the surface. In contrast, the Au–Pd/carbon catalyst exhibited Au–Pd nanoparticles which were homogeneous alloys. On the contrary, the structure of bimetallic catalysts synthesized by sol immobilization method can be controlled by the sequence of reduction of metal precursors, namely $PdCl_2$ and $HAuCl_4$.

Random alloy, Au core–Pd shell and Pd core–Au shell structure can be formed by reduction of mixed precursor solution, reduction of $PdCl_2$ in existence of Au(0) and reduction of $HAuCl_4$ in existence of Pd(0), respectively.[89] A STEM-EDX spectrum image analysis from ref. 89 is presented in Fig. 3, where both reconstructed RGB maps of Au and Pd, and integrated EDX spectra from the center and periphery of the particle confirmed a Pd core–Au shell structure.

A similar successive reduction method has been used to produce three-layer core–shell particles, which consist of an alloyed inner core, an Au-rich intermediate layer, and a Pd-rich outer shell as revealed by HAADF STEM and EDX analysis.[96] The order of metal addition and reduction during initial sol formation affects not only the activity, but also the selectivity.

A series of catalysts with Au : Pd ratios varying from 9.5 : 0.5 to 2 : 8 were synthesized following a two-step procedure. By HRTEM and STEM-EDX mapping it has been suggested that good alloy particle can be formed for the Au : Pd ratio of 9 : 1,

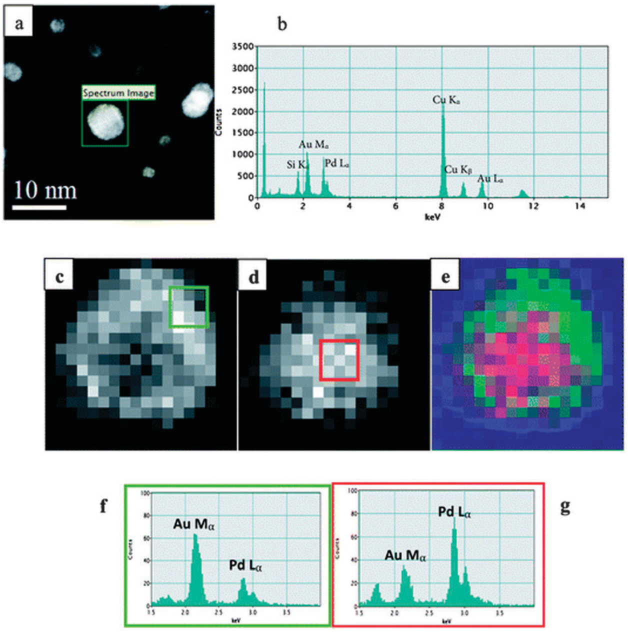

Fig. 3 (a) An ADF image of an Au{Pd} nanoparticle selected for STEM-XEDS mapping; (b) the overall XEDS spectrum from the nanoparticle showing the presence of both Au and Pd; (c and d) the Au and Pd elemental maps of the nanoparticle obtained after MSA processing: (e) an RGB reconstruction showing the distribution of Au (green) and Pd (red)-the blue channel is neutral; (f and g) the cumulative XEDS spectra from 3 × 3 pixels (indicated by squares in (c & d)) from the center and periphery of the particle respectively. Reproduced with permission from ref. 89. Copyright 2011, The Royal Society of Chemistry.

8 : 2, and 6 : 4, while the catalyst with Au : Pd = 9.5 : 0.5 and Au : Pd = 2 : 8 consist segregated Pd particles and were considered as the reason of low activity and quick deactivation in oxidation of glycerol.[48]

In the liquid phase oxidation of benzyl alcohol, a model reaction that we describe in Section 3, it was found that the compositions of catalyst particles change dynamically as the reaction proceeds.[97] Physically mixed Au/AC and Pd/AC was used as starting catalyst. *In situ* formation of surface Au–Pd bimetallic sites by re-precipitation of Pd onto Au nanoparticles was verified by STEM-EDX mapping on the catalysts after 0.5 h and 1 h of reaction, showing the possibility of synthesising alloy bimetallic nanoparticles even from a physical mixture. Fig. 4 shows the STEM image, Au and Pd maps and the superimposed two maps of a few alloy particles formed after one h reaction. Pd concentration increased with time on the initial Au particles. Negligible Au leaching was observed. When bimetallic sites are formed Au stabilises Pd atoms, thereby preventing Pd aggregation and leaching, which leads to deactivation of the catalyst.

With the improvement of resolution both for TEM and STEM, transmission electron microscopy has become a powerful yet routine instrument for catalyst characterization. With atomic resolution, we are able to observe single atoms and small clusters consisting of very few atoms. However, whether these isolated atoms/species play a dominate role in reaction is as yet unknown. One should not forget that TEM can only examine very thin specimens from an area of only a few tens of microns and the signals for chemical analysis come from the whole depth of the sample rather than from the surface only. Furthermore, theoretical simulations are necessary to interpret the experimental results. Therefore, other complementary techniques, such as XRD, XPS, X-ray absorption spectroscopy, can be beneficial to the investigation of catalyst structure (geometrical environment, oxidation state) and understanding the reaction mechanisms not only for the synthesis of nanoparticles but also for establishing structure–activity relationship.

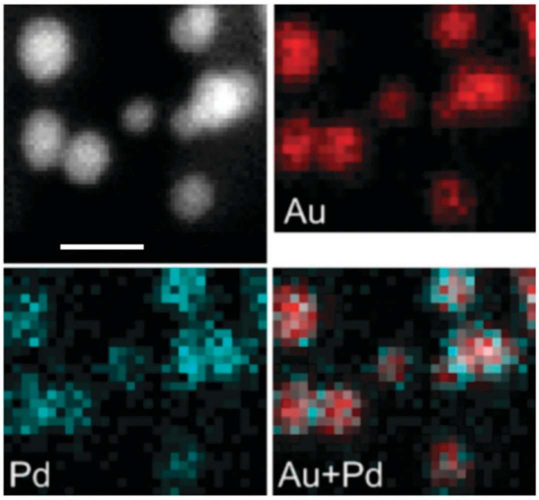

Fig. 4 STEM images, Au and Pd maps and the superimposed two maps from one piece of original Au/AC in the physically mixed catalyst after one h reaction of benzyl alcohol oxidation. Reproduced with permission from ref. 97. Copyright 2010, The Royal Society of Chemistry.

2.2 XAS/XPS characterization of Au catalysts

It is critical to understand the oxidation state of the Au catalyst as well as the particle size and structure. Electron microscopy, discussed in Section 2.1, is particularly amenable to estimating Au particle diameters and structural changes in the Au nanoparticles with time. However, microscopy studies only sample a small concentration of the total catalytic particles within a sample. To improve the understanding of Au catalysts there are a number of laboratory or National Facility measurements which can be employed including, UV, IR and Raman and chemisorption studies (discussed in Sections 2.3, 2.4 and 2.6, respectively) along with X-ray photoelectron spectroscopy (XPS) and X-ray absorption spectroscopy (XAS). XPS and XAS studies are particularly well suited for evaluating Au oxidation states, catalyst coarsening, and synthesis methodology. In addition, with higher resolution studies, and more computationally intensive analysis, the shape of the nanoparticles and binding of adsorbates can be deduced from the analysis of XAS data and high pressure XPS measurements. Examples from the literature will be discussed to highlight some of the results that can be gleaned from these measurements particularly related to heterogeneous Au catalysts.

2.2.1 XAS. The basics of XAS and extended X-ray absorption fine structure/X-ray near edge structure (XANES)/(EXAFS) measurements and analysis are beyond the scope of this review but have been summarized previously.[98,99] Instead we will focus on some key spectroscopic information and analysis of Au catalysts. Fig. 5 shows representative Au-L_3 XAS data collected for four Au standards, Au0, AuCl, $AuCl_3$, Au_2O_3. The data shows a large white-line signal (marked with an A) which is shifted to lower energy for the oxidized Au species. This shift to lower energies, as opposed to higher energies typically observed for oxidized species, is due to a 2p to 5d transition that precedes excitation from the bulk electrons.[100] The Au^+ spectrum has a smaller A-feature likely due to fewer 5d holes.

The inset plot of Fig. 5 shows a comparison between a Au foil and Au supported on silica. The spectra are very similar in shape and energies indicating that the Au nanoparticles are metallic in nature. However, there are slight intensity reductions and positive energy shifts (features A, B, C) due to a reduction in the Au–Au coordination number (CN) from 12 for bulk Au to 6–8 for the supported nanoparticles. This reduction in CN causes a decrease in Au–Au bond distances and a shift in the spectral features to higher energies.

The Au coordination number, determined from fitting the XAFES data provides information about the particle size, which can be related to the TEM data, and the stability of the particle with time/heating. It had been widely noticed that the Au–Au coordination number (CN) was significantly smaller than bulk Au–Au (12). Concomitant to this reduction in Au–Au CN there was a decrease in Au–Au bond distances from 2.88 Å to distances as low as 2.72 Å.[101] In 2006 Miller *et al.* performed

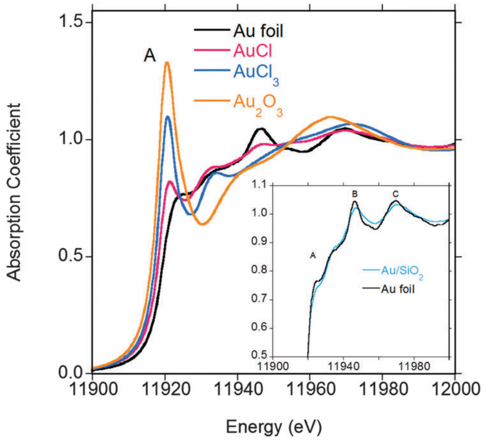

Fig. 5 Au-L$_3$ XAS data collected for various standards. Inset: XAS data collected for Au foil and a 2.5 nm supported Au catalyst.

a detailed set of experiments on reduced Au clusters supported on various metal oxides.[101] Building upon a model for Pt clusters that correlated Pt–Pt CN with hydrogen chemisorption values to estimate metal dispersion they demonstrated that the Au–Au CN could be used to estimate Au dispersion. They found a clear onset for the decrease in Au–Au CN corresponding with a dispersion of about 30%. This is roughly a 3 nm Au particle and correlates with increases in catalytic activity reported by many authors. The origin of this change in Au–Au bond length is likely due to a change in electronic structure of the Au clusters due to atomic rearrangements resulting in new electronic structures.

Given that XAS/EXAFS measurements are sensitive to the bulk properties of the catalyst, one can use this method to more accurately follow the evolution or stability of Au catalysts with time or annealing. For example, Guzman and Gates showed that Au clusters deposited on MgO from Au$(CH_3)_2$(acac) precursors and decomposed at 100 °C and 300 °C had CNs of 4.0 ± 0.4 and 9.4 ± 0.9 (3 nm diameter clusters) respectively.[102] However, the material with a CN of 4 coarsened during the catalytic activation to a CN of 10 indicating the instability of these small clusters. Schwartz *et al.* followed the change in Au chemistry as a function of temperature for Au precursors anchored on various TiO_2 phases.[103] They found reduced Au precursors all coarsened at 300 °C in air. For example, Au bound to Degussa P25 TiO_2 had an initial CN of 6.7 but rapidly evolved to a CN of 9.7 in less than 1 h. They were able to correlate activity with Au size and found the onset at 3 nm similar to other Au catalysts studies.[103] Perhaps, most significantly, they were able to correlate the resulting Au CN/particle size with the pH used during the deposition precipitation (DP) of the Au precursor. They found an increase in particle size when the pH was more acidic than pH ∼ 6. This work confirmed previous studies[104,105] of the importance of the precursor and surface chemistry. In another example, the stability of 2.5 nm Au catalyst supported on fumed silica was evaluated on samples annealed at 500 °C in air for various periods of time.[106] The XAS data showed no change in the Au–Au CN after a month, which confirmed TEM studies on a smaller number of particles. In addition, using XAS measurements Sá *et al.* were able to demonstrate the ability to re-disperse large Au clusters using methyl iodide.[107] These data was confirmed with TEM studies confirming the virtual atomic distribution of Au species enabling catalyst recycling.[107]

Determination of the Au coordination number has enabled the development of some geometric models of supported Au catalysts. Indeed, Carlsson *et al.* employed XANES results in conjunction with scanning transmission electron microscopy (STEM) data to generate one such data set.[108] They investigated Au catalysts prepared by deposition–precipitation supported on TiO_2, $MgAl_2O_4$ and Al_2O_3. Over 2000 particles were imaged and analysed using the STEM providing a particle size distribution. The thickness of the particles was estimated by analysing the intensity of the Au atoms in a cluster relative to the background. As the STEM signal is roughly proportional to Z^2 the integrated intensity is proportional to the number of Au atoms in the particle. This particle size and thickness data is combined in a model that represents the geometric shape with resulting coordination numbers of the Au atoms. To confirm and refine the model the data was compared to Au–Au CN values from the EXAFS data. Together this data results in a cluster model where hypothetical 2 nm Au clusters on TiO_2, $MgAl_2O_4$ and Al_2O_3 have particle heights of 5.4, 4.8 and 3.1 nm respectively.[108] From this analysis one can clearly see large differences in catalyst structures depending on the interactions with the support metal oxide. Clearly, Al_2O_3 provides the strongest interaction driving the resulting sites available for coordination with reactants. However, the benefit of this analysis is an estimate of the number of atoms at different positions on a nanoparticle, *i.e.* edge, corner, face, bulk.

A similar geometric analysis was performed by Shekhar *et al.* investigating Au/Al_2O_3 and Au/TiO_2 catalysts for water-gas shift (WGS) reactions.[109,110] TEM and EXAFS data were used to estimate the average size of an Au catalyst. Assuming all the surface Au is catalytically active the reaction rate should vary as a function of the inverse diameter (d^{-1}). The data however revealed the rate varied as a function of $d^{-1.7}$(TiO_2) and $d^{-1.2}$(Al_2O_3) indicating that the Au surfaces do not exhibit the same rate.[109] Building geometric models of the clusters based on measured particle sizes the team was able to estimate the number of low Au–Au CN perimeter and corner sites on the Au clusters (where the perimeter and corner sites interfacing with support) and the face/surface sites of the Au clusters. They concluded that the active catalytic sites were the corner sites, which were an order of magnitude more active for Au/TiO_2 than those on Al_2O_3. The origin of this increase was due to the influence of surface water. A similar analysis of MoO_x promoted Au/SiO_2 catalysts for the reverse water-gas shift reaction revealed that the same Au–metal oxide interface sites were catalytically active.[111] Furthermore the selective addition of Mo–O species to the Au surface increased the number of interfacial sites and the resulting catalytic activity.

Beyond the study of particle sizes, XAS enables one to follow oxidation states as a function of temperature or treatments based on the A-feature of the XAS spectra (Fig. 5). This is particularly important for catalyst fabrication and the catalyst during use. For example, the Guzman and Gates work showed that Au clusters deposited on MgO from $Au(CH_3)_2$(acac) precursors and decomposed at 100 °C in helium then exposed to different reaction gases had different Au oxidation species.[102] For example, based on the white line the as-prepared sample was predominantly Au^{3+} as was a sample heated in O_2 at 100 °C. The same sample reduced in H_2 showed only Au^0 species, however, under CO and a mixture of CO + O_2 the Au was reduced to a mixture of Au^0 and Au^+. Following CO oxidation *in situ* analysis of the XAS data indicated that at steady state there was a mixture of Au^+ and Au^0 supporting a reaction mechanism where Au is in a mixed oxidation state during a catalytic reaction. Other studies found an induction period for the reduction of Au species in H_2 and CO to form Au which help catalyse further reduction of Au cations.[112]

An interesting study by Bus *et al.* was performed which followed the evolution of the $HAuCl_4$ precursor chemistry for species trapped on TiO_2 and Al_2O_3 at pH 7 as a function of temperature.[113] In this work they found that Au^{3+} trapped on TiO_2 rapidly reduced at room temperature in H_2. By analysing the Au–Au CN the found when half the Au^{3+} was consumed (20 min) the Au–Au CN was about 4.3. Upon further reduction the Au–Au CN increased to 7.9. This indicates the reduction mechanism proceeded through a rearrangement of the Au^{3+} species to form small Au clusters, which continued to coarsen under H_2. Other Au/TiO_2 samples annealed at higher temperatures showed significant coarsening. For example, annealing in H_2/He mixtures at 60 °C resulted in Au CN's of 10.0, while more oxidizing atmospheres (5% O_2 in He) resisted coarsening agglomeration below 61 °C the samples rapidly agglomerated forming large particles when the Au–O precursor decomposed completely above 280 °C (Au CN 9.5). In contrast, similar Au precursors on Al_2O_3 resisted coarsening and Au^{3+} decomposition with heating. For example heating the Au^{3+} in an O_2/He mixture to 350 °C resulted in an Au–Au CN of 4.6 and a significant fraction of oxidized Au. Similar results were reported by Calla and Davis, which showed the need to use temperatures higher than 225 °C to fully reduce the Au.[114] Other XAS studies found a similar support dependence on reduction rate of the Au^{3+} precursor. Indeed, Delannoy *et al.* demonstrated that Au rapidly reduced on TiO_2 while CeO_2 precursors reduced much more slowly at 300 °C and on Al_2O_3 were unreducible.[115] Other studies have found similar high temperature reductions of Au on CeO_2 are required to produce a catalyst with the best activity. For example mixtures of ionic and metallic Au formed at 300 °C on CeO_2 a mixture of oxidized and reduced Au yielded the most active catalyst.[116] These studies reveal the importance of support chemistry in stabilizing and preventing agglomeration during catalyst synthesis and provide a mechanism to optimize catalyst development. Finally, other studies have evaluated the choice of reduction method given the well document stability in light for Au catalysts.[117,118]

The XAS measurements discussed above focus on the bulk properties of the supported Au catalyst. Given that catalysis is a surface dependent process there has been a significant effort to try and understand the bonding of various adsorbates (*i.e.* CO, O_2, H_2, *etc.*) on the Au under operating conditions. By carefully collecting and analysing XAS data of the Au catalyst with and without adsorbates numerous groups, in conjunction with theoretical modelling studies, have been able to estimate changes in surface chemistry due to these adsorbates.[119] This can be accomplished because most of the Au in the nanoparticles is not involved with molecular interactions with the adsorbate and their intensity/signal can be subtracted out of the spectrum. The resulting difference enables understanding of the surface chemistry during a reaction.

For example, Weiher *et al.* exposed Au catalysts supported on TiO_2, SiO_2 and Al_2O_3 to various ratios of CO : O_2.[120] The only sample that was suitable for analysis was the Au/Al_2O_3 which again had the smallest particle size (CN ~ 5.5 compared to TiO_2 ~ 9.2) enabling catalytic activity and high enough activity for a weakly bound species to be observed, unlike SiO_2 supported clusters.[121] For the Au/Al_2O_3 sample there was an increase in the white line region, 11 923 eV, of the XAS spectra compared to the spectra collected in non-interacting helium. This increase is likely to be due to back-donation of electrons from the Au to the CO as the CO binds to the surface. Despite the evidence of electron donation to the CO the Au remained in the metallic state. Similar studies with high concentrations of O_2 over Au/Al_2O_3 catalysts showed an increase in the white line region due to a charge transfer from the Au to O_2 forming a transient Au–O bond.[122] This Au–O rapidly reacts away with the presence of CO. The remaining CO selectively binds to the Au surface due to back-bonding as reported earlier. Miller *et al.* showed a similar ability of small Au clusters to oxidize in the presence of O_2 albeit only to a level of about 10%.[101] Subsequent work on smaller Au clusters (CN = 6.8) supported on TiO_2 showed a similar back-donation of electrons to bound CO species and a much weaker O_2 absorption that was readily replaced by the addition of CO.[121] This data indicates that similar Au–O and Au–CO complexes exist on both reducible and non-reducible supports. Therefore, the differences in activity of Al_2O_3 and TiO_2 supported catalysts have to be due to interface effects or some other fundamental difference in catalyst structure. Similar results were reported for Au catalysts used for the selective oxidation of propane.[123] Analysis of the adsorbed and sorbate-free surfaces revealed the presence of bound surface oxygen. The concentration of the oxygen changed with time as the catalyst was broke in and reached a steady state. These changes in electronic structure are important for industrial applications to optimize reactor performance.

An example using detailed XAS measurements is the evaluation of the differences in H_2 adsorption over Pt and Au supported nanoparticles.[124] As expected H_2 chemisorbs over Pt catalysts (Pt/SiO_2 and Pt/Al_2O_3) resulting in a structural rearrangement of the Pt cluster with more than one H per surface Pt. In contrast, H_2 adsorbs much more weakly on Au/SiO_2 and Au/Al_2O_3 catalysts with less than 1H bound per surface Au atom. The inability to bond 1H per surface atom indicates that the hydrogen is confined to low coordination corner or edge type sites.

The examples discussed above have focused on monometallic Au clusters. Newer catalysts based on Au:M alloys, such as Au:Pd have gained considerable interest. Similar examples, as those listed above, can be found in the literature regarding the synthesis of alloy nanoparticles and the resulting oxidation states. However, one of the strengths of XANES measurements is the ability to estimate the Au–Au and Au–Pd interactions within a cluster. One recent example is the work from Maclennan *et al.* who studied the oxidation of crotyl alcohol.[125] EXAFS data revealed a reduced average coordination number for the catalyst nanoparticle (~9.5). Analysis of the XAS data reveals slight shifts in edge energies possibly due to electron transfer between the Au and Pd. Such transfers will influence the adsorption of reactants as discussed above. Further fitting of the data indicates the extent of mixing between the Pd–Au depending on starting ratios and the segregation of Pd species (Pd : Au = 1 : 1) to the surface during synthesis. This level of structural information is virtually impossible for electron microscopy.

2.2.2 XPS. A second powerful X-ray spectroscopy to characterize Au catalysts is XPS. This instrument is operated under UHV conditions and using the XPS one can gain insights to the oxidation states of Au catalysts as well as following the coarsening of the catalyst particle *ex situ*. XPS probes the top few nanometers of the surface, which limits its utility to catalysts confined to the external surface, as opposed to within pores. However, given that the method probes the surface one can easily characterize the surface chemistry of the support material, which is critical for mediating the activity of Au catalysts. Furthermore, residual surface impurities, *e.g.* Na, Cl, *etc.*, are readily detected which may influence catalyst lifetime and stability. Fig. 6 representative XPS data sets collected for the same standards shown in Fig. 5 above. From this data one sees a clear increase in XPS binding energy of the Au with increasing oxidation state due to screening effects.

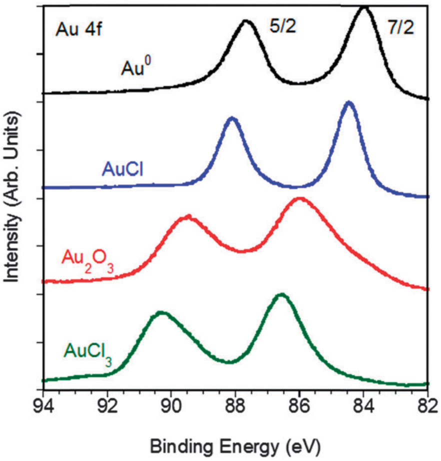

Fig. 6 Representative XPS data collected for Au, AuCl, Au_2O_3, and $AuCl_3$ reference materials using a pass energy of 5.85 eV and an Al X-ray source. The shifts to higher binding energy are due to changes in Au oxidation state and ligand withdrawing strength. Note the wide peaks evident from Au_2O_3 are due to the reduction of Au^{3+} to Au^0.

As noted above the binding energy of the Au 4f species can reflect the Au oxidation state. Changes in the binding energy can be used to follow the synthesis of the Au nanoparticles by methods like deposition–precipitation.[105] The DP method entails adjusting the pH of an aqueous suspension of support material and $HAuCl_4$ to precipitate a Au hydroxide species onto the support surface.[105] The Au hydroxide species is then reduced to form the Au catalyst. This transition in the Au oxidation state is easily followed by XPS. For example, Zwijnenburg *et al.* deposited $Au(OH)_3$ on TiO_2 and followed the Au 4f signal as a function of thermal treatment.[126] They report the Au 4f binding energy shifting from 84.2 eV to 83.3 eV upon annealing from 150 °C to 400 °C indicating a reduction in the Au oxidation state. Similar studies were performed by Park and Lee looking at the formation of catalysts on Fe_2O_3, TiO_2 and Al_2O_3.[127] For catalysts grown on Fe_2O_3 and heated to 100 °C the Au 4f peak shows up around 86.5 eV consistent with Au^{3+} in the oxide. Upon annealing at 200 °C the intensity of the 86.5 eV peak decreases while the peak at 84 eV increases indicating that the Au^{3+} reduces directly to Au^0. At 300 °C the Au is completely reduced. Interestingly, the use of Al_2O_3 supports necessitated heating the catalyst to 200 °C to fully reduce the Au precursor highlighting the role of support in catalyst synthesis. Finally, Fu and co-workers used XPS to show that $Au^{\delta+}$ and Au^+ were the catalytically active species for water-gas shift reactions after an elegant leaching experiment with cyanide.[128] The NaCN selectively removed all the Au^0 from a catalyst bed leaving only the oxidized Au as measured by XPS, which remained catalytically active.

In many of the studies reported for Au catalysts the binding energies of the fully reduced Au species were significantly different than 84.0 typically observed for Au foils. These values range from 84.5 to 82.9 eV.[118,126,129–141] These values would indicate a negatively charged Au nanoparticle. This is not supported by XAS results on these materials which show that the Au is metallic Au^0. The origin of these shifts is attributed to initial or final state effects.[28,142] Initial state effects would lead to negative binding energy shifts and are due to quantum size effects. Smaller particles have a higher fraction of under-coordinated surface atoms, as indicated from the XANES data. This under-coordinated Au shifts the Fermi level lower energy reducing the energy needed to emit surface electrons from the metal resulting in a lower binding energy BE.[28] This hypothesis is be supported by Radnik *et al.* who claim that the more spherical the nanoparticles, the lower the binding energy (down to 83.0 eV for Au on TiO_2).[132] Alternative models of initial state effects attribute the shifts to lower BE to lattice strain.[143] As the Au cluster relaxes on the metal oxide the Au-Au bonds change to conform to the oxide surface. The shorter metal-oxide bonds cause a reduction in the Au–Au bond length similar to what is measured from the XANES analysis. This reduction in bond length increases electron density on the Au–Au bond which is probed by the spectrometer. Final state effects lead to a positive BE shift and are due to the difficulty in neutralizing the electron hole produced on the Au particle with an electron from the support.[28] Given that many of the catalyst supports are electrically insulating oxides, and the fact that these BE shifts are observed for all catalysts despite dramatic differences in activity, the electronic effects may play a secondary role in the observed XPS data. Alternatively, the smaller a Au particle becomes the lower the screening efficiency the remaining Au atoms provide to neutralize the hole created by the emitted electron. This process would also result in a positive BE shift.[144] Another, more general way to view this effect would be through the polarization of a metal cluster by the Madelung potential of the support.[145] In this model changes in the local chemistry from doping or impurities results in a change in electric potential for all the atoms in the lattice, including those of the catalyst cluster.[146]

All the different concepts regarding the origin of the BE shifts can be supported by one analysis or another; the problem is that no model describes all of the experimental data. For example 2.4 nm Au particles supported on TiO_2 have a Au 4f binding energy of 83.2 eV.[118] The initial binding energy reported for Au was 83.2 eV for 2.4 nm particles, consistent with initial state effects. Over 6 days the Au clusters coarsened to form 22 nm Au clusters but the binding energy was reduced further to 82.9 eV.[118] These final particles are too large to exhibit initial state effects or final state effects due to a lack of screening electrons. There is one way to determine which model is correct. This involves measuring the Auger parameter (α) of the catalyst particle which will overcome any charging effects which may shift peaks.[147–149] To our knowledge only one XPS study investigating the Auger parameter for supported Au catalysts has been attempted.[126] By measuring the difference between the binding energy of the Au 4f photoelectron species (83.47 eV) and the kinetic energy of the $M_5N_{67}N_{67}$ transition (2015.61 eV) the experimental α was 2099.08 eV which is in agreement with Au foil (2099.15 eV) indicating that the clusters were predominantly metallic.[126] The conclusion was the shift in Au 4f binding energy was due to the low coordination of the Au clusters.

Beyond determining electronic structures XPS can be used to follow the extent of particle coarsening with time particularly if there are no changes in support surface area.[106] It is well known that Au catalysts are sensitive to light but the exact mechanisms or processes that occur are not well understood. One way to follow the changes in Au chemistry is to measure XPS spectra as a function of time. This was performed for light sensitive Au/TiO_2 catalysts where the Au to Ti ratio was measured as a function of time and light exposure.[118] This data showed that the Ti : Au ratio rapidly increased with time indicating that the Au particles were coarsening and forming larger Au clusters. The apparent decrease in Au concentration was due to most of the Au being confined within the larger >20 nm particles and hence not measured by the XPS. This trend was confirmed with electron microscopy studies.

The results discussed above were collected on laboratory sources. The future of XPS studies involves the use of high pressure XPS systems built using of differentially pumped apertures.[150–152] One of the first examples investigated the adsorption of O_2 on Au/TiO_2 materials.[153] They found no direct reaction with O_2 on the Au surface at 13 mbar however, X-rays could help activate O_2 enabling a more reactive oxygen species which could form a Au–O bond. Recent work out of Germany extended the study of oxygenates to ozone over Au foil.[154] it was found that the O_3 reacted to from an oxide which rapidly decomposes when the O_3 source is removed. Willneff *et al.* studied Au catalysts supported on P25 as a function of temperature and CO + O_2 pressure.[155] They found the electronic structure of the Au catalysts changed as a function of temperature. Indeed, there appears to be two Au species at room temperature but only one Au species at 77 °C with a slightly higher binding energy than Au^0.

2.3 UV-Vis spectroscopy

2.3.1 Why UV-Vis spectroscopy. Another spectroscopic technique that can be used to corroborate Au particle size, shape and oxidation state that can be derived from XPS and XAS is ultra violet visible spectroscopy (UV-Vis). UV-Vis is also a fundamental tool in catalysis as the UV-Vis spectra contain information on the catalyst itself *via* the electronic and vibrational transitions of the species present. From their d–d and charge transfer transitions derive oxidation states and coordination. Estimation on the dispersion of supported oxidic or metallic species is possible. Au exhibits the phenomenon of surface plasmon resonance (SPR) which gives access to particle size and shape. Molecularly dispersed spherical small AuNPs in water is therefore characterized by a ruby colour and a broad absorption band at about 520 nm in the visible region. According to the position and width of this band, quantification of AuNPs in liquid phase is established. Spherical AuNPs have a unique characteristic SPR band at about 520 nm; whereas ellipsoidal ones have two bands at about 520 nm and 670 nm (Fig. 7). Au nanorods have also two characteristic plasmon bands at 520 nm and in the range 600–1600 nm ascribed respectively to transverse and longitudinal plasmon bands (Fig. 7).

Indeed, the wavelength of the SPR maximum increases intimately with particle diameter, and for uneven shaped particles such as Au ellipsoidal or nanorods, the absorbance spectrum shifts considerably into the red region of the spectrum when compared to a spherical particle of the same diameter. The first

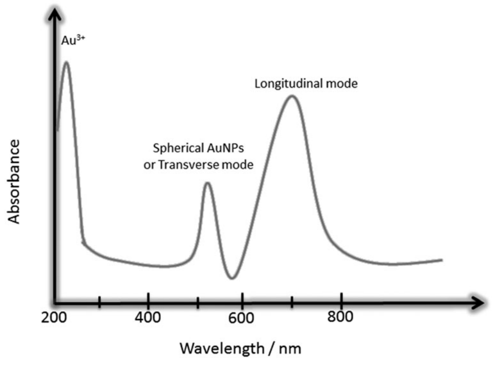

Fig. 7 Representative extinction spectrum of a mixture of aqueous $HAuCl_4$ (band at about 222 nm), spherical AuNPs (about 520 nm) and uneven shaped AuNPs with typical bands assigned to transverse (about 520 nm) and longitudinal mode (about 670 nm).

SPR band is due to the polarization along the shorter axis and the second one, is due to the polarization of the longer axis.

Interpretation of diffuse reflectance (DR) UV-Vis spectra of a solid in catalysis research can be incomplete because species may not absorb or exhibit very broad absorption and interfere with other features. Fundamentals of transitions in the UV-Vis region are well described in textbooks and articles.[156] This part of the review aims to demonstrate UV-Vis can further provide information on AuNPs oxidation states, shape and particle size. This is possible through the SPR band that reflects the extinction spectra of AuNPs.

2.3.2 Some fundamentals in the determination of Au nanoparticle size and oxidation state using UV-Vis. The Mie theory[157–159] distinguishes two ranges of Au nanoparticle size. When Au nanoparticles are smaller than 15 nm, the scattering component that is also an optical property, is negligible that only absorbance is taken into account. In the case of very small particles (<2 nm) as well as Au bulk, this resonance does not give rise to an absorption because of a low electron density, therefore less dipole oscillations of the free electrons, in the conduction band. The SPR band at about 520 nm is indeed less enhanced to almost non-existent for Au particles smaller than 2 nm.[160,161] With AuNPs size of 2–20 nm, the conduction electron density increases and results to the excitation of the surface resonance absorption in the visible light region (400–600 nm) at a higher wavelength than 520 nm.

The band position as well as the intensity and the bandwidth are influenced by the AuNPs size, oxidation states or any possible aggregation of AuNPs in solution. These optical properties of spherical AuNPs in aqueous solutions can be analysed both theoretically and experimentally. Indeed, several methods were reported to calculate the particle diameter (d) from UV-Vis spectra, and determine the particle concentration (N). Haiss *et al.* evidenced that for Au hydrosols particles of 35 to 110 nm size, there is a perfect match between the experimental data and the calculated position of the SPR peak.[158] We therefore reported here both equations they proposed to determine Au particle size (d) and one for the concentration (Fig. 8).

In the case of d_1, C_{Au} is the initial Au concentration (in mol L^{-1}), A_{SPR} is the SPR absorbance $C_1 = 4.70$ and $C_2 = 0.314$ are Haiss' theoretical fit parameters, and they estimated an error of about 6%. In the case of d_2, λ_{SPR} is the SPR wavelength, $\lambda_0 = 512$; $L_1 = 6.53$ and $L_2 = 0.0216$. The latter values are all Haiss' theoretical fit parameters for $d > 25$ nm. They reported only a 3% average absolute error in calculating the mean experimentally observed AuNPs diameters. As a direct consequence of determining d from the above equations, the number density of the particles per unit volume (N) can be defined from the experimental absorbance at 450 nm (Fig. 8). At this wavelength, Haiss and co-authors found a better agreement between theory and experiment. For more details about these equations, the reader is invited to refer Haiss *et al.*[158]

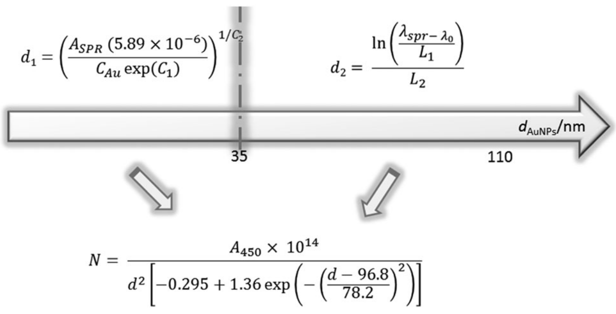

Fig. 8 Equations proposed by Haiss and coauthors[158] to calculate AuNPs size (d) according to the expected range of size of the nanoparticles and to obtain the AuNPs concentration (N).

Oxidation states of Au species can be deduced looking at precise wavelength value of the maximum absorbance as well as the bandwidth, information on the AuNPs UV-Vis spectrum as is the case with Au/Fe_2O_3 catalysts for the CO oxidation and the water gas shift reactions.[162]

2.3.3 Oxidation state determination. The UV-Vis spectrum of Au/Fe_2O_3 sample suspended in ethanol exhibits bands at 245, 385 and 545 nm. The first band can be assigned to electronic transition of d–d type in the Fe^{3+} ion and ascribed to the $E_g \rightarrow T_{2g}$ transition,[163] the second band corresponds to oxidized states of Au in the form[164] Au^+ and $Au_n^{\delta+}$ and the third band to the SPR of Au(0).

In a typical process of preparation of Au nanoparticles, the nanoparticles are stabilized to avoid any aggregation of the nanoparticles and therefore increase their stability. To attain the requested stability, stabilizers also called capping agents or protecting groups (for example PVA in catalysis or ligands for biosensors or nanomedicine fields) are utilized and their contribution on the absorbance spectra recorded by a UV-Vis spectrometer will be discussed. This information are of importance for the sol immobilization method. Once stabilized with PVA, the Au^{3+} ($AuCl_4^-$ anion) characterised by a band at $\lambda_{\max} = 222$ nm (Fig. 7) are reduced to Au(0) sol Au which has a SPR band in the range 490–520 nm. The vanishing band at 222 nm to the benefit of the second one recorded by UV-Vis spectrometer corroborates the presence of only Au(0) in solution.[159] This method was revealed a fast and reliable way to confirm that the sol contains only Au(0) before the immobilization on the support.[165–167]

Moreover, a study of the SPR band can deliver a fast assessment about the Au size evolution. Gasparotto *et al.* investigated on the electrocatalytic activity of AuNPs for the borohydride oxidation where the polyvinyl pyrrolidone (PVP) protected colloidal AuNPs were obtained through the reduction of Au^{3+} by glycerol in alkaline medium.[168] They concluded looking at the SPR band position which did not vary with increasing the glycerol concentration that the size and distribution of AuNPs were approximately similar.

2.3.4 Shape and pH effects. Larger AuNPs (>6 nm) are more selective during the glycerol oxidation than smaller particles.[4,68,166] Hence, a control of the size and shape of the AuNPs is of importance for understanding catalytic activity and selectivity. Au nanospheres and nanorods were synthesized by one-phase thiol etching of polydisperse PPh_3-capped Au nanoparticles and accurately characterized by UV-Vis. The typical

SPR band at about 520 nm was almost missing on the UV-Vis spectrum of spherical Au–PPh_3 because of very small Au nanoparticles (<2 nm). However, after the thiol etching process, optical absorption peaks at 680 nm and 700 nm were recorded for the Au nanorods and nanospheres, respectively. The different phosphine-thiolate protected Au nanorods and nanospheres were latter supported on CeO_2 in order to compare their respective performance in the catalytic CO oxidation.[169]

Qi *et al.* studied the catalytic reduction of 4-nitrophenol (4-NP) in the presence of $NaBH_4$ over α-cyclodextrin (α-CD) capped Au nanoparticles.[170] By increasing the concentration of α-CD (0.2 to 10 mM) the Au particle size decreases as evidenced by the blue-shift of the SPR band from 528 to 518 nm as shown in Fig. 9A. Indeed, with higher concentration of α-CD, an increase of the effective capping on the Au particle surface occurred that particle growth is diminished leading to the formation of small AuNPs. This blue-shift was concomitant with the diminution of the band intensity suggesting a decrease of Au nanoparticles concentration (Fig. 9A). During the synthesis of the α-CD capped AuNPs, the concentration of the added NaOH plays a fundamental role in the particle shape and size. Basic conditions are actually necessary for the reduction of the Au metallic salts by the CD. Shape modification result in the formation of irregular Au aggregates such as Au wire-like nanostructures as evidenced in Fig. 9B. When the solution pH was stabilised at about 10.5 (2 mM NaOH), 20 nm spherical AuNPs are formed. Increasing the pH to 12 (30 mM NaOH) many irregular aggregates of Au nanoparticles were formed. The formation of Au wire-like was evidenced by UV-Vis spectroscopy (Fig. 9B, curve g).

Curve f Fig. 9B represents a mixture of spherical AuNPs and nanoaggregates with two bands at about 520 nm and 700 nm. They are ascribed to the SPR band of spherical AuNPs and the fusion of Au nanoparticles into wire-like nanostructures.[171] The stronger basic conditions achieved by the addition of 30 mM of NaOH led to the formation of irregular 1D[172] and 3D aggregates as evidenced by the broad band at 650 nm in the UV-Vis spectrum (Fig. 9B, curve g).

The effect of the pH of the solution on the Au nanoparticles size effect and consequently on the position and width of the plasmon band maxima were also investigated.[173,174] Fenger *et al.*[175] prepared cetyltrimethylammonium bromide (CTAB) stabilized Au nanoparticles of different size by seeding growth method for the catalytic reduction of *p*-nitrophenol. The initial seed solution is relatively alkaline that when ascorbic acid, a mild reducing agent, is added the pH value of the colloidal solution is diminished that a blue-shift of the plasmon band is observed (smaller AuNPs are formed). Moreover, an increase of the AuNPs (from 10 to 56 nm) size should lead to a red shift of the SPR band. In their case, the position and the width of the plasmon band maxima remained almost unchanged as a direct consequence of the invalidation of the pH and size effects.

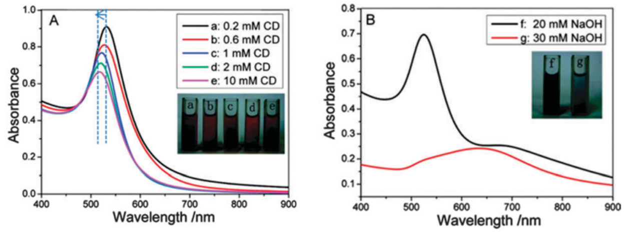

Fig. 9 (A) UV-Vis absorption spectra of the AuNPs prepared at different α-CD concentrations; (B) UV-Vis absorption spectra of the AuNPs prepared at different NaOH concentrations. Adapted with permission from ref. 170. Copyright (2009) American Chemical Society.

To ensure an improved deposition of the AuNPs on a support, adjusting the pH value of the colloid AuNPs solution below the isoelectric point of the support is necessary. In the case of Au/Al_2O_3, the SPR bands of AuNPs at about 520 nm became sharper and red-shifted as the pH value of the Au colloid solution decreased from 8.2 to 1.9; indicating the growth of AuNPs under very acidic conditions as confirmed also by TEM (5.7 nm to 8.7 nm).[173]

2.3.5 Reducing and capping agent effects. The important role of the reducing and capping agent on the control of Au nanoparticles has been previously highlighted and these can be studied effectively using UV-Vis. However, the influence of the capping molecule structure on the efficiency of the AuNPs catalyst has to be taken into consideration.[176–178] The catalytic performance of stabilized AuNPs was evaluated in the reduction of 4-nitrophenol (4-NP) by sodium borohydride under homogeneous conditions in water. An electron transfer takes place between 4-NP and $NaBH_4$ through the AuNPs and can therefore be monitored by UV-Vis spectroscopy. In the UV-Vis spectra, an absorption band at 384 nm corresponds to the reactant (4-NP), whilst the appearance of a band at 296 nm is assigned to the formation of the desired product, the *p*-aminophenol.[173] Diverse stabilizing agent have been used such as CTAB, amines derivatives as reported elsewhere.[176,177] The nature of the surface capping agent influences the SPR band. Lee *et al.* observed for example that the SPR bands at about 530 nm for all amines derivatives stabilized icosahedral 50 nm AuNPs are narrower (smaller full width at half maximum) than that of CTAB stabilized AuNPs.[177] Moreover, the amine derivatives-stabilized AuNPs are more active with a five times higher reaction rate than the one of CTAB stabilized AuNPs. Such difference in the catalytic performance can be explained by the surface characteristic of each stabilizer. CTAB contains long alkyl chains and could alter the access of the substrate onto the surface of the AuNPs, whilst the amine nitrogen containing stabilizer enhances this access.

The effect of the ligand has been also highlighted for the catalytic CO oxidation over thiol ligand-stabilized AuNPs deposited on CeO_2.[169] For this reaction, Au nanospheres where prepared through the etching of polydisperse phosphine protected Au with two different aromatic thiols ligands, namely thiophenol (PhS-H) and 2-naphthalenethiol (NapS-H). Au nanospheres prepared with PhS-H, $Au_{25}(SPh)_{18}$, show optical absorption bands at about 700, 460 and 425 nm whilst the one of AuNPs obtained by NapS-H, $Au_{25}(SNap)_{18}$, are observed at about 680, 500 and 400 nm (Fig. 10). The shifted peaks between the two Au nanospheres are ascribed to the different electronic properties and steric effects of PhS-H and NapS-H. The SPR which is sensitive to both geometric and dielectric effects changes position distinctively even with thin

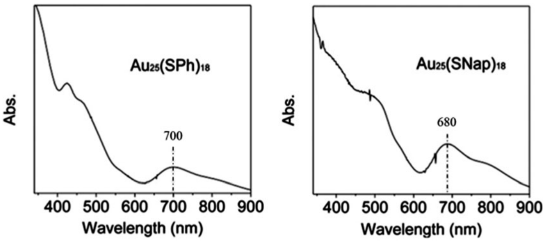

Fig. 10 UV-Vis spectra of the aromatic thiolate-protected $Au_{25}(SPh)_{18}$ and $Au_{25}(SNap)_{18}$ nanospheres. Reproduced with permission from ref. 169. Copyright 2015, The Royal Society of Chemistry.

shells. Indeed, any shell layer that differs from its refractive index to the surrounding medium will cause a shift in the surface plasmon transverse and longitudinal mode positions. Therefore, the peak position compared to the theoretic one obtained by the Mie theory are usually altered.[157–159] The calculations performed utilising the Mie theory are based on naked nanoparticles. Furthermore, the difference in the SPR band was also evidenced in the catalytic CO oxidation at 100 °C. $Au_{25}(SPh)_{18}$ prepared with PhS-H were more active (factor of 25) than the one obtained with NapS-H.

Dendrimers with surface amino groups were also used to stabilize AuNPs for the catalytic oxidation of Morin by H_2O_2.[178] Before their reduction by $NaBH_4$, a strong absorption band at 220 nm and a weak one at 290 nm were observed. They were ascribed to Au^{3+} and to the ligand-to-metal charge transfer (LMCT) bands of $[AuCl_4]^-$ ions between Au and chloro ligands, respectively. Dendrimers stabilized Au nanoparticles, after $NaBH_4$ reduction, do not present anymore the band at 220 nm implying that all $[AuCl_4]^-$ ions were completely reduced. When more poly(amidoamine) dendrimers are added, the absorption band at 290 nm increased and was ascribed to the formation of ion-pairs between the amino group of the dendrimer and $[AuCl_4]^-$. Stronger the interaction between the amine group and the Au particles, less dendrimer is used. The appearance of the band at 520 nm confirmed the presence of Au nanoparticles.

Size, pH, shape effect were discussed and as foreseen by the Mie theory, the position of the SPR band is also associated to the solvent medium refractive index (n) as demonstrated by the experimental results[161] and theoretical equation.[158] Indeed, the Au nanoparticles as well as nanorods revealed really sensitive to the dielectric properties of the their solvent. By varying the refractive index from 1.333 to 1.627 (water and carbon disulfide, respectively passing through toluene with an index of 1.496) red-shifts of the SPR band position and slight broadening of the band were observed.[161] These results are in perfect agreement with theoretical equation.[158] Because of such properties, Guo *et al.* demonstrated that not only AuNPs can catalyse the reduction of nitroarenes in water but also can be utilised as refractive index sensor.[161]

2.3.6 Diffuse reflectance UV-Vis spectroscopy. To characterize supported Au catalysts, diffuse reflectance ultraviolet visible (DR UV-Vis) spectroscopy was used to determine the state of Au nanoparticles and the presence of Au in the final support structure. This derives from the presence of the SPR absorption bands at about 520 nm for spherical AuNPs as it is the case of AuNPs in solution. The SPR wavelength of 520 nm can vary intimately with the size of the AuNPs or with the possible interaction with the support. The light absorption efficacy of the AuNPs depends on the nature of the support, and it can occur that the support itself exhibit little absorption of light in the range 400–800 nm.[179] When AuNPs are deposited on different supports, an absorption band at about 520 nm is observed in the UV-Vis range of the catalysts. This band depicts the SPR of the Au nanoparticles, hence the oscillation of the free electrons of the nanoparticles in the selected support.

Zhu and coauthors[180] prepared AuNPs supported on Al_2O_3, CeO_2, TiO_2, ZrO_2 and zeolite Y, and tested these catalysts under visible light for the reduction of ketones to alcohols, the deoxygenation of epoxides to alkenes, the reduction of nitro-aromatics to azo-compounds and the hydrogenation of azo-benzene to hydroazobenzene. Among several techniques of characterizations, they followed by DR UV-Vis the effect of the support and their respective activity in the cited above reactions. Comparing Au/CeO_2 and Au/TiO_2, the SPR band of Au/CeO_2 (Fig. 11, brown spectrum) is red shifted and the peak is more intense of the one of Au/TiO_2 (Fig. 11, green spectrum) suggesting thus a stronger SPR effect of Au/CeO_2. They excluded by TEM images any differences in the Au particle size. Consequently, they explained the strong absorption light of Au/CeO_2 by the possible strong interface action between AuNPs and CeO_2.[179]

A DR UV-Vis spectrum encloses information on the catalyst itself *via* the electronic and vibrational transitions of the species present, namely d–d and charge transfer transitions, that oxidation state and coordination can be obtained.[181] Hence, it is expected to detect a red or blue shift of the Au SPR band at 520 nm according to the support.

Furthermore, Zhu *et al.*[180] correlate the increase of the intensity of the SPR band at 520 nm with an increasing loading of AuNPs (from 0 to 5 wt%) on CeO_2 as shown in Fig. 12. Concomitantly with the increase of intensity of the SPR band at 520 nm, higher conversion is achieved with the increase of Au loading in the photocatalytic reduction of styrene oxide.

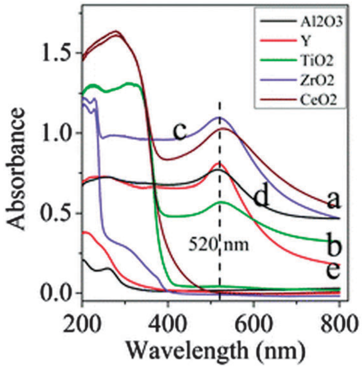

Fig. 11 UV-visible (UV/Vis) diffuse reflectance spectra of Au-NPs on different supports: (a) Au/CeO_2; (b) Au/TiO_2; (c) Au/ZrO_2; (d) Au/Al_2O_3; (e) Au/Y. Reproduced with permission from ref. 180. Copyright 2014, The Royal Society of Chemistry.

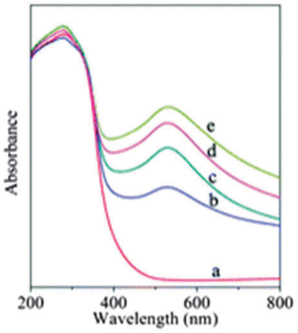

Fig. 12 UV/Vis diffuse reflectance spectra of Au/CeO_2 with various amounts of Au loads: (a) 0 (CeO_2); (b) 0.5%; (c) 1.5%; (d) 3%; (e) 5%. Reproduced with permission from ref. 180. Copyright 2014, The Royal Society of Chemistry.

As an example, the DR UV-Vis of Au/CeO_2 exhibits three characteristic bands; a sharp one at about 227 nm, a broad one at about 340 nm and a broad and weaker one at about 555 nm.[182] The first two bands belong to the support as reported in the literature.[183] CeO_2 exhibits absorption bands in the UV region (250–350 nm) which are ascribed to a charge-transfer transitions between O 2p and Ce 4f and interband transition with characteristic bands at about 250 nm ($O^{2-} \rightarrow Ce^{3+}$), 297 nm ($O^{2-} \rightarrow Ce^{4+}$) and 335 nm, respectively. Therefore, the authors ascribed in their study the one at 227 nm to $O^{2-} \rightarrow Ce^{3+}$ charge transfer transitions and the one at 340 to both $O^{2-} \rightarrow Ce^{4+}$ charge transfer transitions (312 nm) and to interband transition (331 nm). Finally, the broad band at about 555 nm characterizes the SPR of Au nanoparticles indicating thus that AuNPs are deposited on the support.

Tsukuda *et al.*[184] characterized also by DR UV-Vis Au supported on hydroxyapatite (HAP) for the selective epoxidation of styrene. Au_{25} clusters protected by 18 glutathionate (GS) ligands and labelled $Au_{25}(SG)_{18}$ were deposited on a HAP support; and the obtained composite was calcined to remove the GS ligands. The final Au loading was of 0.5 wt% and Au_{25} size of about 1.4 nm. The sharp peaks observed on the UV-Vis absorption spectrum of original solution of $Au_{25}(SG)_{18}$ disappeared on the DR UV-Vis spectrum of the corresponding calcined sample 0.5Au_{25}-HAP. The absence of the SPR band is justified by the generation of a structural isomer of Au_{25} during calcination or by an interaction between Au_{25} and the support. Similar catalysts were prepared by varying the preparation procedure, from impregnation to DP and adsorption. On the latter three samples a SPR band at about 550 nm, recorded by DR UV-Vis, was observed suggesting thus that the Au clusters on these catalysts are bigger than the one in 0.5Au_{25}-HAP. Likewise, Caruso *et al.* investigated on the synthesis of AuNPs on agarose hybrid network and porous AuNPs/TiO_2 by DR UV-Vis for photocatalytic application.[185] UV-Vis diffuse reflectance spectra of the calcined Au/TiO_2 strongly absorbed in the visible, at about 600 nm, that the presence of the SPR band validate the successful incorporation of AuNPs inside the TiO_2 matrix.

2.3.7 UV-Vis of bimetallic catalysts. Au based catalysts were demonstrated to be a valid catalyst in several reactions such as glycerol oxidation,[160] the selective epoxidation of styrene,[184] reduction of 4-nitrophenol.[176,177] It is reported that catalytic reactivity and stability for a range of catalytic processes, such as hydrogenation, oxidation, hydrogenolysis and reforming can be significantly improved.[15] Supported Au based bimetallic nanoparticles are attractive catalysts because catalytic reactivity and selectivity are improved as we mentioned in previous sections. Moreover, looking at any changes in the SPR bands important information can be deduced on the structure of the bimetallic system, *i.e.* physical mixture of two monometallic systems or formation of a bimetallic system. UV-Vis measurements is a powerful technique in the characterization of core–shell particles as it is possible to monitor the progress of the particle formation or shell deposition.[187]

A comparison of UV-Vis spectra of physical mixtures of Au and Pd monometallic particles is shown in Fig. 13a. The absorption at about 520 nm is ascribed to the SPR band of Au, a group 11 metal ($d^{10}s^1$). This band can be seen upon a

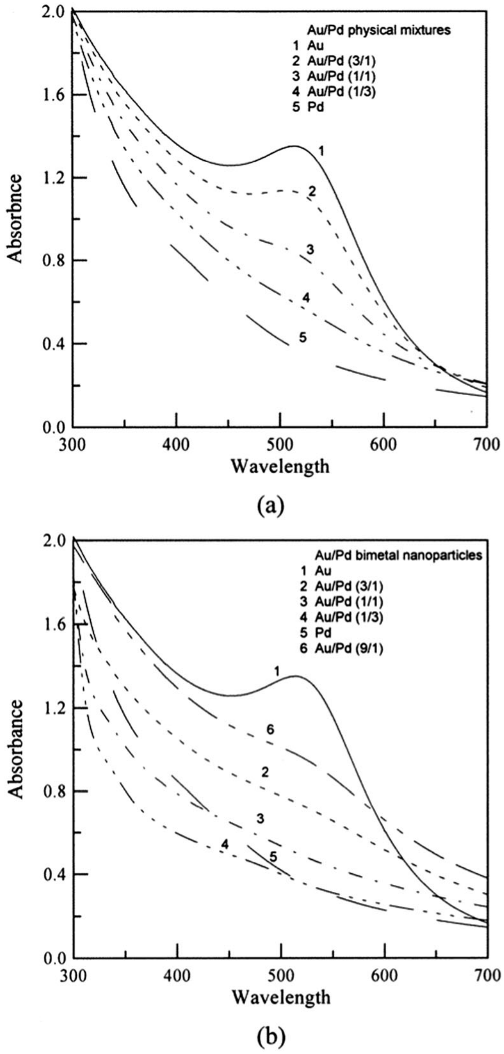

Fig. 13 UV-Vis spectra of (a) the physical mixture of individual Au and Pd nanoparticles and (b) Au–Pd bimetallic nanoparticles at various molar ratio. Reproduced with permission from ref. 188. Copyright©2001, American Chemical Society.

physical mixture Au–Pd (1/1) to almost disappear when a mixture of Au–Pd (1/3) was measured. Fig. 13b represents a bimetallic Au–Pd system. Only in the case Au–Pd (9/1) represented by the spectrum 6, the discrete but characteristic SPR band of Au at 520 nm is observed. The disappearance of the Au SPR band is justified by the presence of a group 10 metal (d^8s^2), Pd. Indeed, when in a bimetallic Au–Pd system the surface plasma energy of Au is suppressed it can be concluded that the surface of the Au–Pd bimetallic nanoparticles has more Pd atoms than the inner core.[188]

It is worth mentioning that such results do not directly suggest a core–shell structure, but can suggest the formation of bimetallic nanoparticles as reported by Toshima and Yonezawa[189] who investigated PVP stabilized Au–Pt and Au–Pd bimetallic nanoparticles. In their study, the SPR band of the PVP-stabilized Au/Pt bimetallic nanoparticle dispersion have a smaller peak area than the physical mixture of Au and Pt nanoparticles dispersions at the same ratio. This observation implies that in the structure of the Au–Pt bimetallic nanoparticle, at least both Au and Pt atoms bind to each other. The color change from red to bronze is an additional indication that Pd shell–Au core bimetallic nanoparticles were successfully prepared as reported by Schmid and co-workers and investigated for the partial hydrogenation of hex-2-yne.[190]

Au–Ag core–shell nanoparticles were synthesized and characterized by UV-Vis technique by Calagua *et al.*[191] to certify the Au–Ag core–shell structure. The SPR band for the AuNPs was at 521.4 nm whereas for Au–Ag nanoparticles, a discrete band at 570 nm and a pronounced band at 407.6 nm were observed. The pronounced band at 407.6 nm is ascribed to Ag where the SPR absorption band is at 410 nm. The red shift of the Au SPR band (from 521.4 nm to 570 nm) could be due to the existence of a region between core and shell. In this region, contribution of both metal takes place and not only the contribution of each individual metal.

The bimetallic Au–Ag system has attracted interest because the SPR band can be tuned between 520 nm for Au and 410 nm for Ag by varying the composition of the structure. Therefore, Au–Ag alloy can be easily prepared from Au(core)–Ag(shell) or Ag(core)–Au(shell). Wang *et al.* prepared for example Au–Ag alloy NPs through interface diffusion of core–shell structured Au/Au nanoparticles[192] where Ag NPs were used as starting 13 nm seeds. By reduction of $HAuCl_4$ with oleylamine at 50 °C, the core–shell structured Ag/Au (with 2 nm Au coating) nanoparticles were heated at 100 °C to facilitate Ag and Au diffusion in the core–shell structure for the formation of Au–Ag alloy nanoparticles. The process of the alloy formation was monitored by the plasmonic peak change in the UV-Vis spectra.

The SPR absorption band of the 13 nm Ag NPs is at 410 nm. The Au-coated Ag NPs have a SPR peak at 524 nm corroborating the formation of Au shell on the Ag seeds. To promote the diffusion of Au and Ag NPs, the Au–Ag core–shell structure is heated to 100 °C and immediately a slight blue shift of the SPR band from 524 nm to 520 nm occurred.

By increasing the heating time to 6 h, the SPR peak continues to shift to 460 nm, and remains stable but sharper upon 24 h (Fig. 14). The mutual diffusion between Ag and Au NPs ended to reach an equilibrium after 6 h where the Au–Ag alloy NPs are formed. This structure evolution form core–shell to alloy can easily be followed by color changes of the NPs dispersion. Indeed, at the beginning of the diffusion process, the solution containing the NPs is dark red, characteristic of Au colloidal dispersion. After 24 h the solution becomes yellow validating the diffusion of Ag into Au.

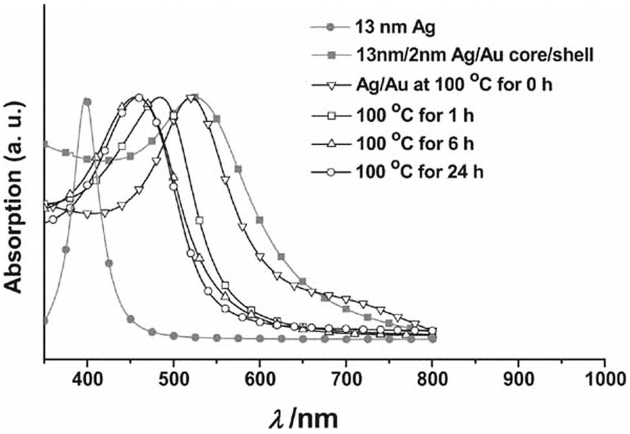

Fig. 14 UV-Vis spectra of the 13 nm Ag NPs and the 13 nm/2 nm Ag–Au core/shell NPs before and after annealing in oleylamine at 100 °C for 0, 1, 6, and 24 h. The composition of the NPs after 24 h annealing was measured to be $Au_{36}Ag_{64}$. Reproduced from ref. 192. Copyright©2009, Wiley.

In most cases, many studies of AuNPs catalysts focus mainly on the maximum SPR position. However, it is important to note that that the position of the SPR band can be easily altered by the dielectric properties of the environment,[161] the solution pH,[170,173,175] aggregation[170,172] and physical or chemical interactions on particles surface.[169,176–178] Indeed, some of these parameters can induce increase of the particle size, shape modification that the usual position SPR band at about 520 nm can be blue or red shifted, and new band at higher wavelength can be observed.[170] One feature is that optical spectroscopy is sensitive to the presence of Au nanoparticles larger than 2 nm. The lack of the SPR band at about 520 nm is an indication that AuNPs were not deposited over the support, or that their size is smaller than 2 nm, or that the concentration of Au clusters larger than 2 nm is relatively low. A red shift of the SPR band, a drop of the intensity (*i.e.* decrease in the concentration of nanoparticles) in the maximum absorbance, an increased width at half maximum and appearance of new absorption bands above 600 nm are all indications that nanoparticle aggregation and shape changes have occurred. UV-Vis spectroscopy is therefore a powerful tool to investigate Au nanoparticles size, shape, concentration and oxidation states. Information on the support through its d–d and charge transfer transitions are obtained.

In bimetallic systems, monitoring the evolution of the SPR bands provides valuable information on the structure. Physical mixture of two metallic nanoparticles, core–shell or alloy structure can be studied, suggesting that although UV-Vis spectroscopy is a simple and practical technique, it can provide information that can facilitate the researcher to plan the next steps of their research regarding the synthesis of materials as well as planning the next steps of more detailed characterisation such as SPS, TEM and XAS.

2.4 Probing the surface sites of supported Au catalysts by FTIR transmission spectroscopy

2.4.1 Why is FTIR spectroscopy a useful technique? Infrared spectroscopy detects the vibrational transitions induced in a material by interaction with an electromagnetic field in the infrared (IR) range. When employed in surface science, in contrast to XPS (Section 2.2.2) that probes only the top few nanometers of the surface, this IR technique provides information about the nature and structure of surface or adsorbed species as well as the strength of the chemical bonds. To be IR active, a change in the dipole moment of the species must occur, according to well defined selection rules. The position of a band (expressed in wavenumbers, cm^{-1}) in the IR spectrum is given by applying the equation of the anharmonic oscillator:

$$\nu = \frac{1}{2\pi c}\left(\frac{k}{\mu}\right)^{1/2}$$

where ν is the frequency, c is the speed of light, k is the force constant of the bond between the two atoms which make up the oscillator and μ is the oscillator reduced mass. Therefore, the position of a band depends on both bond strength and mass (isomeric effect).

The experiments we describe have been carried out in the mid IR frequency range, between approximately 700 and 4000 cm^{-1}, in which most of the molecular vibrations absorb light. The discussion will be focused on the advancing research in the characterisation of Au catalysts obtained by transmission Fourier transform Infrared (FTIR). In these instruments the full collimated infrared beam is processed by a Michelson interferometer, that is the heart of a spectrophotometer, before focusing it onto the sample.[193] The source is normally a glow-bar IR lamp. Modern FTIR instruments generally use mercury–cadmium–telluride (MCT) detectors for signal detection, because they are quite sensitive and cover most of the mid IR frequency range. Actually, modern instruments are able to provide signal-to-noise ratios low enough to detect absorption bands in the 10^{-4} absorbance units. To enhance sensitivity more intense sources such as synchrotron radiation[194] or tunable IR lasers[195] can be employed instead of regular glow-bar IR lamps. However, synchrotron facilities have restricted access and tunable lasers work only at certain frequencies.[26]

The main issues concerning FTIR measurements in transmission mode are usually related to the transparency of the examined catalysts and to the possibility to prepare self-supporting pellets. Examples of quartz cells employed in the case studies here illustrated are shown in Fig. 15.

Such cells are equipped with KBr windows (transparent to the IR beam) and allow thermal treatments in controlled atmospheres and spectrum scanning at ambient temperature or at controlled temperatures (from −173 °C to ambient temperature).

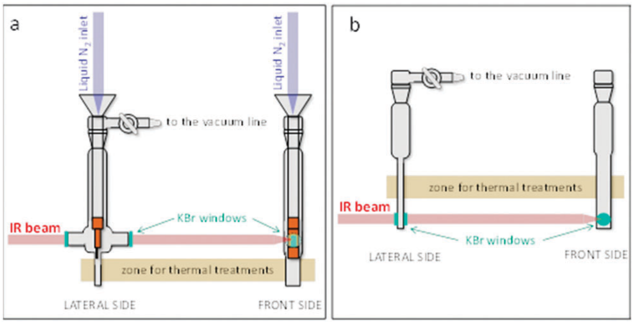

Fig. 15 FTIR cells; section a: cell for analyses at low temperature, section b: cell for analyses at room temperature.

2.4.2 FTIR spectroscopy of adsorbed molecules: the CO probe. CO is the probe molecule most extensively employed to study metal sites. CO adsorption should be either non-reactive, in this case carbonyl species are formed, or reactive, in which CO undergoes chemical transformations on the catalyst surface, giving rise mainly to the formation of carbonates and formates. CO is an ideal probe molecule because the position of the CO bands (due to the C–O stretching vibration, νCO) can provide specific information on both oxidation and coordination state and on the electrophilic properties of the accessible Au sites.[196,197] Additionally, CO is also a reactant in many reactions catalysed by Au, such as CO oxidation, CO preferential oxidation and water-gas shift reaction. Another advantage is that the vibrational spectrum of CO is not complex. The νCO is sensitive to the strength of the bond formed with the surface, and most of the supports are transparent in the C–O stretching region (usually between 1700–2250 cm^{-1}).

A change in the position of the band related to adsorbed CO respect to the molecule in gaseous phase (2143 cm^{-1}) can be interpreted by the Bhyholder Model which considers the adsorbing site (a metal site)–CO bond as a result of two main contributions.[198] The former is due to a σ donation, that originates from the overlapping between the 5σ full orbital of the carbon atom (with weak anti-bonding nature) and the empty d orbital of the metal site with opportune symmetry (d_{z^2}), as shown in Scheme 1, that implies an electron density transfer from the CO molecule (lone pair on C atom) to the metal centre with an increase of the bond strength. Thereafter, the position of the CO band undergoes to a blue shift if compared to the free molecule.

The latter is a π back-donation ($d\pi \rightarrow p\pi$) with bonding character, due to the overlapping among two full d orbitals of the metal and the anti-bonding 2π* degenerate molecular orbitals of CO (Scheme 1). Such interaction introduces electron density into the anti-bonding CO orbital and the (C–O) bond strength is decreased and the νCO is red shifted with respect to the free molecule.

Depending on the nature of the adsorption site, one of these two factors, *i.e.* σ donation or π back donation, can prevail over the other: for metal ions with high oxidation state donation

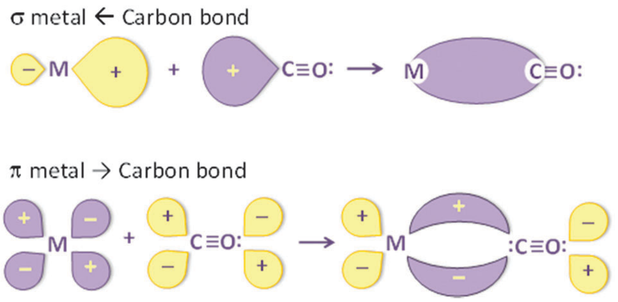

Scheme 1 Metal–carbonyl bond: formation of a σ metal←carbon bond and of a π metal→carbon bond. The other CO molecular orbitals are omitted for the sake of clarity; the violet orbitals are full, the yellow one is empty.

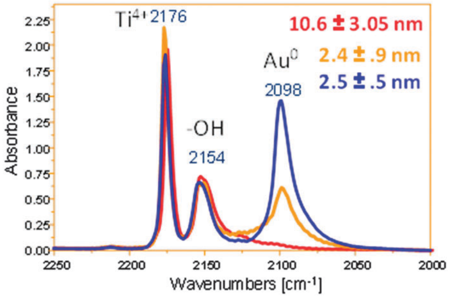

Fig. 16 FTIR absorbance spectra in the carbonylic region of 4 mbar CO adsorbed at 100 K on Au/TiO$_2$ calcined at 200 °C (orange curve), at 300 °C (blue curve) and at 600 °C (red curve).

prevails (reduced Au) whereas metal atoms, neutral or partially negatively charged, bestow back donation. Generally, the CO extinction coefficient is high. However, it strongly depends on the nature of the bond with the surface. In addition, the CO molecule is small and its adsorption is mediated by steric hindrance. Linear bonded CO molecules are associated with wavenumbers in the approximate range 2000–2170 cm^{-1}, doubly bridged ones with the 1880–2000 cm^{-1} region and finally multiply-bridged CO species with that below 1880 cm^{-1}. Due to the nature of Au catalysts, this review will discuss linear bonded carbonyls species, whose bands are reversible to the outgassing. CO is able to reduce cationic Au, *i.e.* Au^{3+} and/or Au^{+} sites,[199,200] therefore it is advantageous to perform experiments at low temperature in order to minimize reactive adsorption of CO. Moreover, it is well known that CO adsorption at low temperature (the working temperature reached by our cell is around 100 K) also can identify sites on which the probe molecule is weakly adsorbed. With respect to the expected position of the CO band, frequency shifts (usually blue shifts) can occur with increasing coverages. These shifts can be due to (i) adsorbate–adsorbate repulsion; (ii) local electric field modification brought about by other adsorbate molecules; (iii) changes in the metal–adsorbate bonding geometry; (iv) vibrational coupling *via* common bonding electrons; (v) change in the metal adsorbate bond strength depending on the nature of the metal (chemical shift) and (vi) dipole–dipole coupling (the CO molecule is represented as a dipole).[201] In addition, due to dipole–dipole coupling, the absorption could be not proportional to the number of molecules, invalidating the possibility to apply the Lambert–Beer's law. Moreover, the coupling of molecules with different ν can produce small shifts, whilst an intensity transfer from low ν modes to high ν modes can occur. Dipole–dipole interactions can also change when CO is adsorbed on corners and edges (more isolated sites) giving rise to an irregular broadening of the band at lower ν. All these effects can complicate the interpretation of FTIR spectra and the use of isotopic ^{12}CO and ^{13}CO mixtures is sometimes recommended. As for the spectra presented in the following, the background before the inlet of the probe was subtracted.

2.4.3 Insights concerning the nature of Au sites: effect of the Au nanoparticle size. The FTIR spectra of CO adsorption on three Au/TiO$_2$ catalysts calcined in air at different temperatures and simply outgassed at ambient temperature are shown in Fig. 16.

This experiment is taken from a pioneering study, in which the catalysts were prepared with the same Au loading (1 wt%) by deposition–precipitation and calcined at increasing temperature (200, 300, and 600 °C).[202] As a consequence, different Au particle sizes were obtained, as specified in the figure, where the Au average size obtained by TEM is reported. The samples were simply outgassed at ambient temperature and the spectra were obtained after interaction with 4 mbar of CO at −173 °C, normalized on the intensity of the absorption band at 2150 cm^{-1}, due to CO interaction by hydrogen bond with the surface OH groups. This band can be taken as a measure of the exposed hydroxylated titania area. The band at 2176 cm^{-1}, whose frequency region is typical of CO adsorption on cationic sites, is related to CO adsorbed on Ti^{4+} ions.[203] No shift by reducing the CO pressure is observed, indicating that these sites are not perturbing each other and are therefore isolated. A component of such absorption was assigned to CO on Au perimeter sites close to the support.[202]

The band at 2100 cm^{-1} is assigned to CO chemisorbed on metallic Au sites.[202,204,205] It is completely absent on the 600 °C sample and it is stronger on the 300 °C than on the 200 °C sample. The 600 °C sample is characterized by metallic particles larger than 10 nm and with edge$_{\text{Au atoms}}$/total$_{\text{Au atoms}}$ ratio < 0.1, by assuming an ideal Wulff geometry.[206] The complete absence of this band indicates that only the step sites are able to adsorb CO even at a temperature as low as −173 °C, while Au terrace sites, which constitute the majority of the exposed Au sites for the 600 °C sample, do not adsorb CO at all.[207] The lower intensity of the band at 2100 cm^{-1} related to the sample calcined at 200 °C if compared to that of the one treated at 300 °C can be explained by assuming that on this catalyst a significant fraction of Au is still not metallic but in an oxidized state, in spite of a smaller mean diameter of the metallic Au particles. By interaction with CO at −173 °C, these Au species remain in their oxidized form, unable to adsorb CO. On the contrary, the 300 °C sample has been prepared at a temperature high enough to produce metallic Au species and consequently shows the highest intensity of the band at 2100 cm^{-1}, in agreement with EXAFS and XANES results on samples prepared at the same temperature.[208]

2.4.4 What can be learned from different spectroscopic features of the CO band on Au sites. The results concerning a series of Au catalysts on different supports are here illustrated. The catalysts are prepared by deposition–precipitation and annealed at 400 °C. Table 1 lists the Au loading, Au average particle sizes and CO chemisorption data (mol_{CO}/mol_{Au}).[209]

The absorption coefficients of supported Au species (nanoparticles, neutral or negatively charged clusters) can be determined by comparing the integrated areas of the CO bands, previously normalized to the Au content, with volumetric CO chemisorption data.[210,211] When the spectra are normalised by the use of the absorption coefficients, the intensity of the CO absorption band can be directly connected to the abundance of the adsorbing species according to the Lambert–Beer's law. The FTIR spectra of 0.5 mbar CO adsorbed at −116 °C on Au/TiO_2 (top curve), Au/ZrO_2 (middle curve) and Au/CeO_2 (bottom curve) are shown in Fig. 17. This pressure is the one at which the saturation of Au sites is reached. Indeed, a further increase in the CO pressure does not produce any increase in intensity of the CO band on Au (data not shown). All the samples underwent previously to reduction in H_2 at 250 °C, hydration at ambient temperature and successive cooling to −116 °C. This pre-treatment is the most suitable for a comparison among different Au catalysts on different supports, since the mild reduction eliminates the oxygen bonded to the surface of very small Au particles,[212] while the hydration saturates the support cationic sites, preventing CO chemisorption. Hence, the spectra display the carbonyl species adsorbed on Au.

Table 1 Properties of the Au catalysts

Catalyst	Au loading (wt%)	SSA ($m^2\ g^{-1}$)	Au size (nm)	mol_{CO}/mol_{Au}
Au/TiO_2	1.51	55	3.8 ± 0.8	0.033
Au/ZrO_2	1.94	92	1.6 ± 0.6	0.301
Au/CeO_2	3.0	118	>10 and <1	0.081

Reproduced from ref. 209.

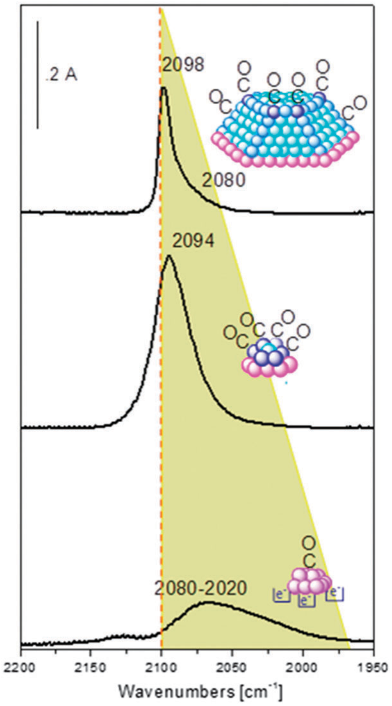

Fig. 17 FTIR spectra of 0.5 mbar CO adsorbed at −116 °C on Au/TiO_2 (top curve), Au/ZrO_2 (middle curve) and Au/CeO_2 (bottom curve). Spectra normalised with respect to Au content and absorption coefficients.

As shown in Section 2.4.3, CO adsorbs most strongly on surface coordinatively unsaturated sites, *i.e.* 6-fold corners and 7-fold coordinated edges. Commonly, the Au^0 sites chemisorb the CO probe giving rise to a band centred at 2100 cm^{-1} (red dashed line in the Fig. 17). Despite the same experimental conditions in which CO adsorption has been carried out, considerable differences as for the shape, the intensity and the maximum position of the bands in the 2100–2060 cm^{-1} frequency range are observed, as highlighted by the yellow triangle. In particular, as for Au/TiO_2 (top curve), in addition to the quite strong and narrow band at 2098 cm^{-1}, a shoulder at lower frequency is observed. Both absorptions are due to CO on Au sites[202] and through the combined analysis of FTIR absorption spectra of ^{12}CO–^{13}CO isotopic mixtures and of quantitative chemisorption data,[209] the presence of mutually interacting corners and edges sites on the supported Au particles with mean size 3.8 nm and whose absorption coefficient is 3.2 $cm^{-1}\ mol^{-1}$ ($\times 10^4$) has been demonstrated.

A Wulff-like model of an Au particle similar to those detected by TEM on titania[202] is depicted close to top curve in Fig. 17. A possible arrangement of the adsorbed CO on 6-fold coordinated corner atoms and on lateral edge sites is also given. The same experiment performed on Au/ZrO_2 (middle curve) gave rise to an intense band at 2094 cm^{-1} whose position is close to that observed on Au/TiO_2, however it is broader and more symmetric in shape. On this sample, the comparison of HRTEM data with CO chemisorption results indicate that there is a strong discrepancy on the amount of Au adsorbing sites, if assuming that only nanoparticles with average size of 1.6 nm are present (Table 1). CO chemisorption measurements demonstrated the additional presence of highly dispersed Au adsorbing sites, escaping from HRTEM detection. Basing on the behaviour during outgassing at −116 °C and/or upon heating at ambient temperature (not shown), as well as on the different absorption coefficient, 1.8 $cm^{-1}\ mol^{-1}$ ($\times 10^4$), the band at 2094 cm^{-1} is assigned to mutually interacting Au corner sites exposed at the surface of non-metallic neutral clusters exposing a large fraction of uncoordinated Au atoms (see also the model in the Fig. 17, close to middle curve).[209,213] Upon CO adsorption on Au/CeO_2, a broad and red shifted band is observed in the 2080–2020 cm^{-1} range. This catalyst is characterised by having a bimodal Au size distribution, as it contains highly dispersed clusters and big particles (Table 1). The latter species does not contribute to the overall FTIR spectrum, because particles >10 nm expose relatively few uncoordinated sites. The observed downshift in position of the band indicates that the sites are almost isolated and not interacting each other and that the bond between the probe and the site is changed as a consequence of an electron transfer from the reduced support to the metal, resulting in the formation of negatively charged Au.[214] Such effect is evident only if the Au dispersion is very high (a particle would disperse the negative charge on the overall mass). This band is hence due to CO on negatively charged clusters, where all atoms are exposed at the surface and are possibly flattened due to the strong interaction with reduced ceria (a representation is given close to bottom curve of Fig. 17).[214] The molar absorption coefficient of these species, 1.3 $\mathrm{cm^{-1}\ mol^{-1}}$ ($\times 10^4$), is similar to that related to the highly dispersed Au clusters on zirconia.[210,211] In this paragraph, spectroscopic evidence has been given that, besides the metal size and the nature of the support, also the Au oxidation state can affect the CO absorption band. Au oxidation state (metallic Au^0 or cationic Au^+) is a controversial and widely discussed factor that was considered for explaining the Au catalytic activity in many reactions,[215–217] therefore it should be intriguing to follow what happens when a similar system is contacted with an oxygen atmosphere.

2.4.5 Reactivity of highly dispersed Au: a case study. Fig. 18, section a shows the effect of $^{18}O_2$ inlet at −173 °C on CO preadsorbed at the same temperature during the first 10 minutes of interaction on Au/CeO_2. The use of $^{18}O_2$ rather than $^{16}O_2$ helps in discriminating between the oxygen atoms from the gaseous phase and those belonging to the support, to observe an eventual involvement of ceria in CO oxidation. The catalyst was previously submitted to reduction in H_2 at 200 °C and further cooling to −173 °C. No pre-hydration was performed, consequently the support sites are available to CO adsorption. It should be remembered that the O_2 molecule, owing to its symmetry, is IR inactive (no change of the dipole moment), therefore the discussion will be focused on the effects of O_2 inlet on the CO bands as well as on the produced species. The spectral range is extended to 2400 $\mathrm{cm^{-1}}$ in order to follow the reactivity of the catalyst in the CO oxidation by detecting the production of adsorbed molecular CO_2 already at −173 °C.

Upon $^{18}O_2$ co-adsorption, the broad band at 2020–2080 $\mathrm{cm^{-1}}$ (blue curve) gradually converts in a narrow peak at 2103 $\mathrm{cm^{-1}}$, *i.e.* CO on negatively charged Au evolved into CO on neutral Au (orange curve). Moreover, the band at 2140 $\mathrm{cm^{-1}}$, related to CO on Ce^{3+} sites,[218] is converted into CO on Ce^{4+} (band at 2159 $\mathrm{cm^{-1}}$).[218]

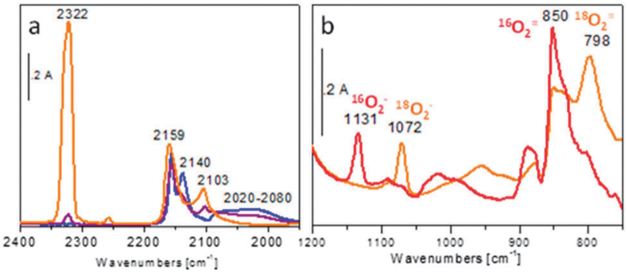

Fig. 18 Section a: effect of $^{18}O_2$ inlet (0.5 mbar) at −173 °C on CO (0.5 mbar) pre-adsorbed at the same temperature (blue curve) during the first 10 minutes of interaction (from violet to orange curves) on reduced Au/CeO_2. Section b: peroxo and superoxo species produced upon $^{18}O_2$ (orange curve) and $^{16}O_2$ (red curve) inlet at −173 °C on pre-adsorbed CO.

These spectroscopic features indicate that the simultaneous change in the nature of the Au sites and the re-oxidation of the ceria surface sites occurred upon interaction with O_2 at low temperature. Goguet *et al.* combining experimental and theoretical methods, proposed a change in the structure of the Au clusters by thermal activation above 250 °C.[219] The cluster is bound to the oxide surface *via* interface Au atoms on cerium vacancies in the oxide lattice.

The removal of these anchor points during oxidation is responsible for the clusters dewetting. It can be hypothesized that the flat Au anionic clusters, in close contact with the oxygen vacancies and the Ce^{3+} ions, change into more roundly shaped clusters after contact with oxygen. Structure changes of Au species supported on CeO_2 were observed during TEM electron beam irradiation.[220] It was found that the Au shape change is correlated with the oxidation state or the density of oxygen vacancies of CeO_2, where the rapid desorption and adsorption of oxygen were identified. The change in morphology, accompanied by simultaneous Ce^{3+} oxidation, as well as by $C^{16}O^{18}O$ isotopomer production already at low temperature (band at 2322 $\mathrm{cm^{-1}}$)[202] point out exceptional reactivity of the negatively charged Au sites towards O_2. This process is fully reversible, because flat anionic clusters are obtained if the sample is submitted again to thermal treatment in H_2 (not shown). Moreover, only $C^{16}O^{18}O$ is produced indicating that at −173 °C the oxygen atoms of the support do not participate to the reaction and anionic Au sites are able to efficiently activate both CO and O_2 reactants. However, peroxo and superoxo species[221,222] are observed at the surface of reduced CeO_2, too (section b, orange curve). The presence of such species (detectable only at low temperature) indicates that O_2 molecules are activated on oxygen vacancies of the support, possibly close to Au. The same phenomenon can be observed also upon $^{16}O_2$ inlet (section b, red curve). It has been reported that the presence of Au dramatically lowers the energy for oxygen vacancy formation on the surface.[223] Small amounts of carbonate species are observed, too (not labelled bands).

2.4.6 Effect of the Au oxidation state. Further experiments on the same Au/CeO_2 catalyst, previously oxidised at 400 °C, allow to get further insight on the effect produced by oxygen on the Au oxidation state. The FTIR absorption spectra produced by CO adsorption at ambient temperature on Au/CeO_2 treated in O_2 at 400 °C and by decreasing the CO coverage at the same temperature are reported in Fig. 19, section a.

Besides a band 2110 $\mathrm{cm^{-1}}$, related to CO on partially oxidized metallic Au[202] a broad absorption at 2166 $\mathrm{cm^{-1}}$ is observed. This band is blue shifted respect to the typical position of CO species on Au^0 (*i.e.* 2100 $\mathrm{cm^{-1}}$). Upon outgassing at ambient temperature it decreases in intensity and shifts at 2160 $\mathrm{cm^{-1}}$, being the reversible fraction due to CO on Ce^{4+} sites. The residual component at 2160 $\mathrm{cm^{-1}}$ is completely irreversible to the outgassing at ambient temperature (bold curve), giving an anomalous evidence of a strong bond between CO and the involved adsorption sites, since CO is usually reversibly adsorbed on Au. This band was assigned to CO on $Au_n(CO)^{m+}$ species, where $3 \leq n \leq 10$ and $3 \leq m \leq 8$, stabilized

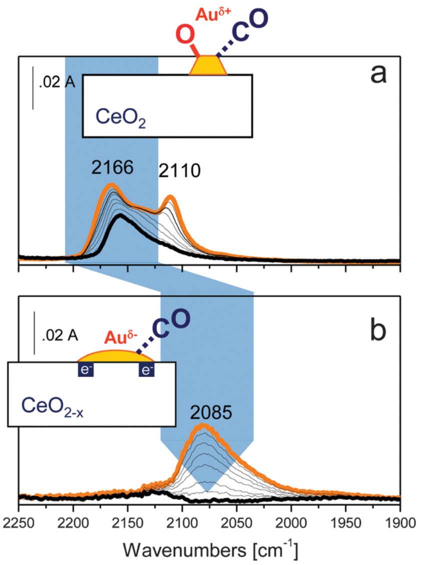

Fig. 19 FTIR spectra of oxidized (section a) and reduced (section b) AuCeO$_2$ collected after CO adsorption (15 mbar) at ambient temperature (orange curve), at decreasing pressures (fine curves) and under outgassing at r.t. (bold curve). The blue harrow is an eye guide to follow the pre-treatment-induced evolution of bands.

on the oxidized surface of ceria.[128,224–226] DFT calculations demonstrated that the binding energies per Au atoms of the cationic clusters are about 0.2 eV and 0.3–0.6 eV greater than those related to the neutral and anionic complexes, respectively. It was also showed that the calculated CO vibrational frequencies are larger than on neutral clusters.[227] CO vibrational frequencies of $Au_n(CO)^{m+}$ complexes in the gas phase ($3 \leq n \leq 10$ and $3 \leq m \leq 8$) have been estimated experimentally and corroborated the assignment as well.[228]

Finally, if Au/CeO$_2$ is treated in H$_2$ at 200 °C, the CO probe reveals that the small oxidized nanoparticles (band at 2118 cm^{-1})[111,195] and the cationic clusters (component at 2166 cm^{-1}) changed into negatively charged Au species (section b). The above experiments are significant, as in the last years the relevance of cationic Au as active sites for CO activation in the water-gas shift reaction has been pointed out.[215,216,225,226]

2.4.7 Characterisation of bimetallic Au–Pd catalysts. It has been reported that Au–Pd bimetallic systems are more active than monometallic Pd catalysts in the direct synthesis of H_2O_2,[229–235] whilst monometallic Au catalysts are relatively inactive.[236,237] The preparation of the bimetallic catalysts here examined involved the separate deposition of Pd by incipient wetness and of Au by deposition–precipitation followed by calcination at 500 °C.[237] The spectroscopic results are compared with those of a monometallic Pd catalyst to investigate the changes induced in the spectra due to the presence of Au. It has to be considered that Pd^0 carbonyls are characterised by a significant π back-donation of the Pd–CO bond, which accounts for a higher stability if compared to Au carbonyls. Therefore, CO will preferentially adsorbs on Pd and it is difficult to observe bands related to the presence of Au sites. On the contrary, Pd^{2+}–CO species have mainly a σ character with a weak π component and the related bands are observed at higher frequency.[199]

The FTIR spectra collected after CO adsorption at −93 °C on bare Pd/ZrO$_2$ (section a), 1Au–2Pd/ZrO$_2$ (first Au then Pd deposition, section b) and 1Pd–2Au/ZrO$_2$ (first Pd the Au deposition, section c) pre-treated in H$_2$ at ambient temperature (orange curves) and in H$_2$, then in O$_2$ at r.t. (blue curves) are shown in Fig. 20. These pre-treatments were accomplished in order to mimic the experimental conditions under which the catalytic tests have been performed. The yields of H_2O_2 followed the order: 1Au–2Pd/ZrO$_2$ > 1Pd–2Au/ZrO$_2$ ≫ Pd/ZrO$_2$.[237]

Generally, the spectra displayed similar features, in particular as for the position of the bands, typically in the range of CO adsorbed on top, twofold bridged or threefold bridged on Pd^0 sites. The bands can be assigned to linear CO species on Pd^0 sites exposed at the surface of (111) facets (bands at 2110–2090 cm^{-1}), to bridged CO on the Pd^0 edges (2001–1990 cm^{-1}), and to bridged CO species on Pd^0 exposed at the surface of either (100) or (111) facets (1945–1966 cm^{-1}). Finally, the absorptions observed below 1898 cm^{-1} are ascribed to CO adsorbed on different threefold hollow Pd sites.[238–240] In the case of 1Pd–2Au/ZrO$_2$ (section c) a band at 2169 cm^{-1}, assigned to CO adsorbed on the Zr^{4+} cations of the support, is also observed.[241]

The overall intensity of the spectra is decreased after pre-treatment in H$_2$ and O$_2$ (blue curves), suggesting the formation of a surface PdO oxide layer, unable to adsorb CO,[242] and where

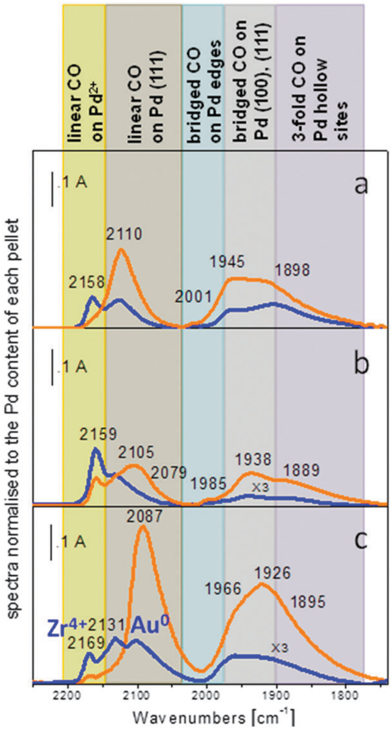

Fig. 20 FTIR spectra of CO adsorbed at −93 °C on Pd/ZrO$_2$ (section a), 1Au–2Pd/ZrO$_2$ (section b) and 1Pd2Au/ZrO$_2$ (section c) after pre-treatment in H$_2$ at ambient temperature (orange curves) and after pre-treatment in H$_2$ and O$_2$ at ambient temperature (blue curves).

oxygen can chemisorb molecularly according to temperature-programmed desorption results.[243] The estimated % intensity decrease for every carbonylic species is larger on the bimetallic samples (the blue spectra in sections b and c are multiplied ×3 for the sake of clarity) than in the case of the monometallic catalyst (50–70%, section a).

In particular 1Au–2Pd/ZrO_2 displays the largest decrease (95%, see section b) confirming that a large fraction of the surface is covered by an oxidic layer and indicating that the Pd sites of this sample are the most easily oxidized. This catalyst exhibits also two components at about 2160 and 2131 cm^{-1} (section b), assigned to CO adsorbed on Pd^{2+} and $Pd^{\delta+}$ sites.[242,244] The tendency of Pd sites to be more easily oxidised in the presence of Au can be related to an electronic effect caused by the Au atoms on the Pd ones,[245] owing to the higher electronegativity of Au (2.54) with respect to Pd (2.2). It was theoretically found that the Pd–Au bond is slightly ionic, and it is stronger than Au–Au and even Pd–Pd bonds.[246] Additionally, on this catalyst the bands in the range 2105–1980 cm^{-1} are red shifted with respect to the frequency of the same CO species on the monometallic sample, because of differences in the lateral interactions. This feature suggests that the Pd^0 sites are more isolated, due to the alloying of the two metals in this sample on the basis of the HRTEM and EDS data.[236] The band at 1985 cm^{-1} is thus assigned to CO bridge bonded on Pd couples exposed at the edges of the metal particles, modified by surrounding Au atoms. These couples of Pd edge sites are relevant to H_2 dissociation. If compared to other components, these sites are less affected by the H_2 and O_2 interaction as indicated by the calculated decrease of the band (25%). These results point out that the oxidic layer formed upon O_2 inlet activates molecular oxygen, whereas H_2 can be dissociated on clean Pd^0 edge sites of the metal particles. In a very recent paper, the formation of Pd–PdO interfaces where H_2O_2 synthesis can take place has been effectively demonstrated on a monometallic Pd catalyst supported on TiO_2.[247] For the 1Au–2Pd/ZrO_2 catalyst, FTIR spectra indicate that the effect of the addition of Au to Pd in enhancing the yield of H_2O_2 is sensitive to a core–shell composition,[248,249] according to Scheme 2.

The spectra related to 1Pd–2Au/ZrO_2 show quite different features (section c). The band at 2160 cm^{-1} (Pd^{2+} sites) is totally missing, due to the further Au deposition.[250] Moreover, an additional band at 2101 cm^{-1} due to CO adsorbed on the Au^0 sites of the small particles is present.[202] This component was not observed when the sample was pre-treated in H_2, because of the very high intensity and stability of the bands related to CO on Pd^0. Interestingly, the band related to CO bridged bonded to Pd edge sites is totally lacking, as a consequence of a decoration effect of Au.[251]

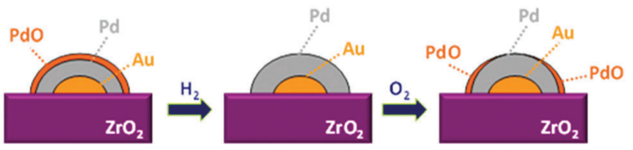

Scheme 2 Representation of the bimetallic phase of 1Au–2Pd/ZrO_2 upon hydrogen and then oxygen exposure.

The above findings demonstrate that FTIR spectroscopy is efficient to investigate the surface of Au–Pd bimetallic catalysts.[252] The spectroscopic characterisation pointed out the occurrence of an electronic effect induced by Au on Pd sites that results in an enhancement in the catalyst reactivity towards H_2O_2 production. This effect is sensitive to the preparation method, as for the order in which Au and Pd are deposited on ZrO_2.

2.5 Chemisorption methods

Quantifying the number of exposed metal active sites, their distribution on the catalyst surface, and determining the metal particle size are primordial parameters in understanding reaction activity and mechanisms. To reduce the amount of active components without interfering with the activity, a better dispersion of the metal (D) on a supposedly inert support is an alternative. Chemisorption of suitable gases on Au based catalysts can deliver information on these central parameters. Indeed, metal dispersion also called fraction exposed is expressed as

$$D = \frac{N_S}{N_T}$$

where N_S is the surface metal atom per unit weight of catalyst and N_T is total metal atoms per unit weight of catalyst. This parameter is significant for the catalyst activity in a selected reaction. Homogeneously dispersed metal implies a larger fraction of metal atoms available for chemisorption of gases and subsequent catalytic reactions, therefore the higher D the higher the predicted activity. Moreover, interaction between the support and the nanoparticles enhances the catalytic activity as reported for the glycerol oxidation over Au/NiO.[253] Additionally to this dispersion, the mean size of Au particles is of importance in diverse catalytic reactions.[186] Indeed, the improved catalytic performance of a catalyst is often justified by the size of the metal particles and the amount of low coordinated Au sites.

More detailed reports can be found in the literature about the selective chemisorption of small molecules on Au based catalysts.[210,254] In this paragraph we will briefly overview a traditional method, the selective chemisorption of a suitable gas on the surface of the Au based catalyst. Chemisorption is established on the interaction of small molecules with small Au particle smaller than 5 nm. The chemisorption of these molecules under conditions can be either associative (*e.g.* CO) or dissociative (*e.g.* H_2, O_2) and results in the formation of a relatively strong chemical bond between the adsorbate molecule with the exposed Au atoms on the surface. As chemisorption is always exothermic, the heat released is related to the strength of the bond; stronger the bond greater the heat. However, species that are strongly held through electronic bonds on the accessible active sites, *i.e.* generating a monolayer coverage, are less reactive. Therefore, the strength of the bond is a critical variable. What is experimentally carried out is the accurate measure of the number of probe molecules that vanish from the gaseous phase in contact with the catalyst under selected conditions of temperature and pressure. In other terms, the amount of gas that is necessary to form a monolayer of adsorbate on an active site is quantified. Special attention is dedicated to the choice of the gas as well as the conditions of measurements which can be performed either as a static (volumetric) or as a dynamic (flowing gas) chemisorption.

2.5.1 O_2 chemisorption. Starting from the dissociative chemisorption of oxygen on Au catalysts, research activities reported on the necessity of a thermal activation in order to chemisorb O_2 on Au.[255] Using a static O_2 adsorption measurements in a pressure range of 4–8 mbar, Fukushima *et al.*[256] reported that the amount of O_2 adsorbed on different Au based supports (silica, magnesia and alumina) increases concomitantly with the increase of temperature (from 170 °C to 450 °C). By increasing the temperature, the adsorption becomes reversible at 340 °C where the isobar reaches a maximum. The authors assumed a dissociative oxygen adsorption that forms a monolayer with a stoichiometry $Au_S : O$ = 2 and 1 at 200 °C and 300 °C, respectively.

Berndt *et al.* also reported that less amount of oxygen is adsorbed at 50 °C than at 200 °C because of the partial coverage of the Au surface.[257]

A temperature of about 340 °C would be the maximum taking into account that O_2 starts to desorb with increasing temperatures.[256] Shastri and Schwank[258] investigated on 2.2 wt% Au/SiO_2 and observed that O_2 strongly adsorbs at 200 °C. O_2 which still sticks on the Au sites after evacuation at 200 and 100 °C completely desorbs at 20 °C. Au dispersion on Al_2O_3 was as well studied by measurements of oxygen chemisorption.[257] Strongly adsorbed oxygen was observed at 200 °C at low range pressure (4–16 mbar) by static O_2 measurements as shown in Table 2. The amount of chemisorbed oxygen was obtained from the difference between the total oxygen adsorption (both chemisorbed and physisorbed) and the physically adsorbed gas. Dispersion of Au nanoparticles on different Au content alumina catalysts was deduced and directly correlated to the activity during the selective oxidation of ethylene glycol to glycolic acid. To alternatively evaluate the oxygen monolayer or coverage on Au surfaces hence dispersion,[257,259] and the Au particle size[259] hydrogen pulse titration on samples were carried out at 200 °C[257] or 300 °C.[259] Assuming a stoichiometry Au_S:O = 2 and a formation of O_2 monolayer at 200 °C on Au/Al_2O_3 with a Au loading of 0.70, 0.94 and 2.14, mostly small Au particles were formed (Table 2). Indeed, the Au particles size were in the range 2.0 to 3.6 nm. From O_2 adsorption on $0.70Au/Al_2O_3$, a size of 2 nm was obtained compared to 2.5 obtained from H_2 titration, size in good agreement with TEM values (1–2 nm).

2.5.2 H_2 chemisorption. Dissociative chemisorption of H_2 by Au particles in Au/Al_2O_3 was highlighted by Bus *et al.* together with X-ray absorption spectroscopy (XAS) technique to show the formation of Au–H bonds.[260] A static volumetric technique was used after reduction and evacuation at 200 °C. H/Au values in the range of 10% to 73% were determined. At fixed pressure, the H/Au value increases or stabilizes with increasing the temperature. They proposed that at similar Au loading, the larger the Au particle size weaker the H_2 adsorption was observed suggesting that H_2 dissociates and adsorbs at low-coordinated edge and corner positions of the Au atom and this was confirmed by theory.[261] It is worth mentioning that the chemisorption of H_2 molecules does not occur on bulk Au and large particles within the temperature range 27–200 °C.[256] Lin and Vannice succeeded to adsorb few amount of H_2 on 30 nm Au on TiO_2 at 27 and 200 °C. Only 1% of the total amount of Au was covered and better H_2 uptake was obtained at the highest temperature.[262] At the opposite with 4 nm mean Au clusters size on Al_2O_3,[263] 14% of the surface Au atoms adsorbed almost irreversibly hydrogen at 0 °C. It can be concluded that H_2 chemisorb on Au nevertheless weakly and in low concentration.

2.5.3 CO chemisorption. To determine the concentration of Au active sites and the mean Au particle size, CO chemisorption on supported Au is an alternative to an expensive TEM study. Several studies reported that CO is weakly chemisorbed on Au. For example, Chiorino and coauthors[209] performed some volumetric CO pulse chemisorption experiments at −116 °C and obtained only 3.3% of CO adsorbed on Au sites on Au/TiO_2 (with a Au mean size of 3.8 nm obtained by TEM); about 3 times more on Au/CeO_2 and almost 10 more time on Au/ZrO_2 (with a Au mean size of 1.6 nm obtained by TEM) as reported in Table 1. Moreover, CO pulse chemisorption carried out at −116 °C on previously hydrated samples can be considered as a method for the quantitative determination of the Au sites also on Au/ZrO_2 catalysts.[211] Furthermore, it is also assumed that low-coordinate sites with coordination number of CN = 6 (*i.e.* corners or kinks) and CN = 7 (edges or steps) are involved during the adsorption.[209,210]

Shastri *et al.* reported the adsorption of CO at 50 °C on Au titania catalysts.[264] A reference experiment was performed on mere TiO_2 which showed some uptake of CO at room temperature but insignificant at 50 °C.

Table 2 Static O_2 chemisorption at 50 °C and 200 °C on different Au loading alumina catalysts[257]

Catalyst	O_2 chemisorption 323 K (μmol g^{-1})	O_2 chemisorption 473 K (μmol g^{-1})	Au dispersity[a] Au_S:Au (%)	Au surface area[a] (m^2 g^{-1})
$0.30Au/Al_2O_3$	0.6	1.7	45	0.36
$0.70Au/Al_2O_3$	0.9	5.3	60	1.11
$0.94Au/Al_2O_3$	1.1	6.6	55	1.38
$2.14Au/Al_2O_3$	2.3/2.5	8.7/8.8	32	1.83
$2.78Au/Al_2O_3$	2.8	11.2	32	2.33

[a] Calculated from O_2 adsorption at 200 °C with a Au_S:O = 2 stoichiometry and 1.15 × 10^{19} Au_S per m^2.

A high vacuum volumetric system in the range 7 to 13 mbar was utilized. Only a weak adsorption of CO was observed and only after 5 min desorption occurred. They could however conclude the mean Au particle size by assuming a stoichiometry Au/CO = 1/1. Lisuka *et al.* reported on CO adsorption on pre-oxidized 3.3 wt% Au/TiO_2 (Au mean size particle of about 3.5 nm measured by TEM) using a constant pressure system (about 15–20 kPa) at different temperatures (−20, −10, 0 and 30 °C).[265] With increasing the temperature (−20 °C to 30 °C), the amount of CO adsorbed (3.66 to 3.44 mL g^{-1}) on Au/TiO_2 decreases reflecting an increase of the adsorption coefficient (22 to 127). They demonstrated that a large portion of CO is adsorbed on TiO_2 support, therefore reversibility of the adsorption of CO is observed; the irreversible part representing only 10% of the total amount of adsorbed CO. These 10% correspond to CO_2 formation at 0 °C on the surface of Au particles as well as the accumulation of carbonate and carboxylate species on TiO_2. Margitfalvi and coauthors quantified the amount of CO that they could adsorb on different Au/MgO catalysts.[266] As a remind, a static volumetric measurement is based on the difference of the total adsorbed gas (both chemisorbed and physisorbed) and the only physically adsorbed gas. To reach the saturation level of CO, they had to use a relatively high pressure (up to 1.3 bar of CO). Although they noticed some CO chemisorption this Au free MgO, a lower chemisorption capacity compared to the Au based MgO is specified.

It is worth mentioning that the necessity of high CO pressure requires a long time experiment. CO chemisorption by using the pulse-flow technique reveals to be a suitable alternative. Most of the time, the CO pulse chemisorption is combined to spectroscopic experiments because of the strength of the IR absorption. Indeed, the vibration of the triple bond and the sensitivity of the CO location on the Au particle and the support surface are easily monitored by FTIR.[210,211]

2.5.4 Sulfur containing probe chemisorption. Rodriguez *et al.* demonstrated using photoemission spectroscopy, that sulfur adsorbed on Au(111) over a wide range of coverages.[267] DFT calculations confirmed that sulfur preferred the three-fold hollow site at low coverage.[268] Beyond a coverage of 0.35 mono layer (ML) the strength of the Au–S bond is reduced concomitantly with the formation of S_2 species. At coverages above a ML, sulfur oligomers began to form because sulfur preferred the on-top site.[269]

Several research groups have moved to thiols as probe molecules as the latter are frequently used to build self-assembled monolayers (SAM) on Au surfaces. Nuzzo *et al.* studied the adsorption of methanethiol and dimethyl disulfide and Au(111). The adsorption of methanethiol was reversible whilst dimethyl disulfide underwent decomposition on the surface.[270] Liu *et al.* adsorbed also methanethiol on Au(111) and observed similar chemisorption features as did Nuzzo and coauthors.[270,271] The decomposition products of dimethyl disulfide desorbed from the surface at 197 °C after an exposure at −173 °C. Such a decomposition could be attributed to defects.

Au–S bonds are strong (about 200 kJ mol^{-1}) so that thiols can be used to titrate Au surface sites.[272] In this respect, Chandler and coauthors investigated on the Au-thiol chemistry to better understand the chemistry of Au by controlled adsorption of phenylethyl mercaptan (PEM) on 1% Au supported on Al_2O_3, SiO_2 and TiO_2.[273] UV-Vis spectra were collected meanwhile the titration of the three Au catalysts suspended in hexane with PEM at 22 °C. The UV-Vis spectrum of PEM exhibits five distinct vibrational bands in the 240–280 nm region. They are all ascribed to the π–π* HOMO–LUMO transition with a pronounced band at 258 nm. Therefore, the absorbance at 258 nm is plotted as a function of added PEM and two trends can be distinguished. In the case of Au/Al_2O_3, approximatively below a value of 0.3 μmol added PEM, only a slight increase in absorbance is observed indicating that all the added PEM adsorbs onto gold. Above 0.3 μmol, the abrupt change in slope corresponds to the molar absorptivity of PEM implying that all the PEM added is free in solution. Following the PEM adsorption from hexane solution, the authors evaluated the total amount of surface Au available. Titration of Au/Al_2O_3 and Au/TiO_2 illustrated a similar thiol-binding constants and the number of surface Au atoms per adsorbed thiol *i.e.* surface stoichiometry (Au_S:S) was found to be 2. Further kinetic poisoning studies showed the Au/TiO_2 and Au/Al_2O_3 catalysts had similar active sites concentration (S:Au_{total} of about 13). Regarding Au/SiO_2, despite a higher surface thiol coverage (Au_S:S of about 1), the catalyst had a stronger thiol-binding constant.

2.5.5 Chemisorption on bimetallic Au Pd catalysts. The addition of a second metal atom (*e.g.* Pt, Pd) to the monometallic Au particles modifies the catalytic activity as compared to the monometallic Au particles. To gain a clear understanding of the molecular level reactivity of metal catalysts, the surface structure of the bimetallic system is investigated.

Freund *et al.*[274] examined the surface structure of Au–Pd nanoparticles formed on reducible CeO_2 metal oxide thin films by CO adsorption both by infrared reflection absorption spectroscopy (IRAS) and temperature programmed desorption (TPD) studies. 10 L (1 L = 1 Langmuir = 1.3 × 10^{-6} mbar) of CO was adsorbed on the catalysts. It is known that pristine ceria film do not adsorb CO since CeO_2(111) surface is oxygen terminated. Therefore, all results obtained by IRAS and TPD are directly associated with the metal deposits. CO which weakly adsorbs on Au/Ceria particles as CO molecules chemisorb only on low-coordinated Au surface atoms, desorbs at −108 °C (Fig. 21). The CO TPD spectrum of monometallic Pd particles is similar to the one of Pd supported on alumina[275] and silica[276] films. They observed that the addition of Au to Pd (Au : Pd ratio) weakens the CO adsorption. The higher temperature desorption at 187 °C assigned to Pd monometallic (Au : Pd 0 : 1) is shifted to 157 °C due to the presence of Au to definitely vanish (Au : Pd 1 : 0).

Concomitantly, as the Pd coverage decreases new desorption features appear at about 155, 205, 305 and 360 K in the spectra and progressively converge to the spectrum for monometallic Au particles (Fig. 21).

TPD was also used by Mullins *et al.*[277] to investigate the interaction of hydrogen with Pd/Au(111) surfaces.

Two initial Pd coverages were investigated, namely 1 monolayer (ML) and 2 ML onto Au(111) surface. The 1 ML Pd–Au surface was annealed to 227 °C (Fig. 22 left) exhibits a broad H_2

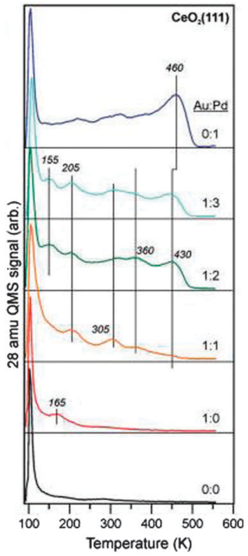

Fig. 21 TPD spectra of CO adsorbed at about 100 K on Pd, Au and Au–Pd particles supported on $CeO_2(111)$. Adapted with permission from ref. 274, Copyright©2010, American Chemical Society.

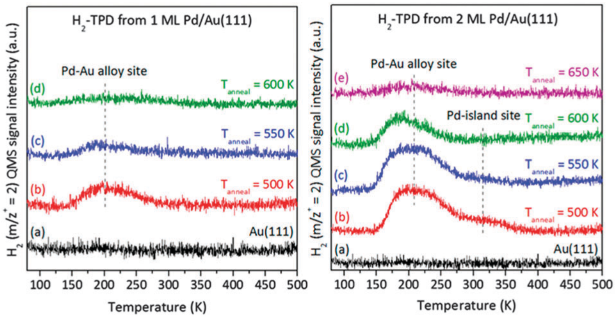

Fig. 22 H_2-TPD from annealed Pd/Au(111) bimetallic surfaces. The initial Pd coverage was 1 ML (left) and 2 ML (right). The surfaces were saturated with hydrogen by backfilling 1 Langmuir of H_2 at a surface temperature of −196 °C. The heating rate was 1 K s^{-1}. Reprinted with permission from ref. 277, Copyright©2013, American Chemical Society.

desorption peak at about −73 °C. H_2 desorption temperature for Au(111) and Pd(111) are in the range −163 °C[278] and 37–47 °C[279] respectively. The authors therefore assumed that the H_2 desorption peak observed at −73 °C consists of Au and Pd atoms, *i.e.* of Pd–Au alloy. This peak becomes less noticeable when the Pd–Au surface was annealed to higher temperature (277 and 327 °C) prior to H_2 exposure at −196 °C. Indeed, at this temperature, fewer Pd atoms reside on the surface.

Moving on to a Pd coverage of 2 ML (Fig. 22 right) therefore more neighbouring Pd sites, the H_2 desorption peak at about 210 K is similar but more pronounced to the one observed with 1 ML Pd–Au(111) surface. It could thus be hypothesized a similitude in the Pd–Au interface in both cases. At an annealing temperature of 227, 277 and 327 °C, another desorption peak ascribed to Pd(111) appeared at 42 °C suggesting the presence of Pd(111)-like islands on the surface. By increasing the annealing temperature, the amount of H_2 desorption decreases for both Au–Pd alloy and Pd-island sites, and to totally disappeared at 327 °C for the Pd island sites. This observation results of the loss of sites for dissociative adsorption of H_2. At 377 °C annealing, only a discrete desorption peak appears. The desorption temperature of Pd–Au alloy sites is lower than the one of Pd island. This implies that the H adatoms stronger binds to the Pd-island sites. The fact that H binds weakly to the Au–Pd alloy sites could be helpful for catalytic reactions involving hydrogen.

In summary the use of selective gas chemisorption on monometallic catalysts is a valuable technique to determine particle size and dispersion. Chemisorption can be considered as a routine experiment as it probes directly the catalyst active surface and the necessary instruments are affordable. In the case of bimetallic systems, nature of the system can be established *i.e.* core–shell, alloy or metal island.

2.6 Raman spectroscopy

Vibrational spectroscopic techniques, including infra-red spectroscopy, Raman spectroscopy, sum frequency generation spectroscopy and electron energy loss spectroscopy, are a class of extensively applied techniques for the study of heterogeneous catalysts.[280] In contrast to other vibrational techniques, such as FTIR spectroscopy, Raman spectroscopy is not based upon the absorption of photons by a sample. Rather, Raman spectroscopy arises from the inelastic scattering of light, which typically loses energy during scattering by exciting the vibrational modes of the scattering sample. The overall scattering event is summarised schematically in Fig. 23. Typically, monochromatic light of a frequency, ν, falls upon a sample, and is scattered back elastically at the same frequency, with no net energy change occurring.

In principle, it is as though the molecule has been excited to a virtual, unstable energy level, and decays back to the ground state without a change in energy. This process is known as Rayleigh scattering, and accounts for almost the entire photon beam. However, if the same molecule was to decay to the first vibrational excited level ($\nu = 1$), then it would effectively remove a particular amount of energy ($\nu - \nu_1$) from the photon beam, and hence the scattered light is observed at a frequency of $\nu - \nu_1$. This particular Raman peak is called the Stokes band, and the change in photon frequency is equal to the energy difference between the two vibrational states. Hence, information on the vibrational structure of a molecule is obtained. The reverse

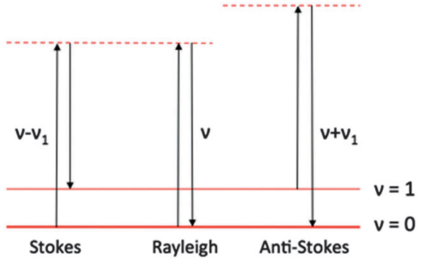

Fig. 23 Schematic representation of the Raman effect, and the fundamental genesis of the Stokes, the Rayleigh, and the anti-Stokes lines.

process, whereby a molecule already in the excited state is temporarily excited to a virtual state and then decays directly to the ground state, may also occur. In this case, the photon beam leaves with a higher frequency, equal to $\nu + \nu_1$. This peak is typically much less intense, due to the typical Boltzmann distribution of molecules between the vibrational ground state and the excited state. It is these inelastically scattered photons that carry the Raman scattering information.[281] We note that the scattering of monochromatic light with a change in frequency was first predicted in 1923,[282] and subsequently demonstrated experimentally in 1928.[283]

As with all vibrational spectroscopic techniques, not every molecular vibration is Raman active. However, in contrast to FTIR spectroscopy, where a change in dipole moment during vibration is required for absorption to occur, a vibration is Raman active if it changes the polarizability of the molecule. In simple terms, this generally requires that the molecule change in shape during its vibration. This generalised picture already emphasises the complimentary nature of Raman and FTIR spectroscopy: whereas IR spectroscopy is highly sensitive to the vibrations of polar molecules, such as CO and H_2O, and asymmetric vibrational modes, Raman spectroscopy is highly sensitive to symmetrical vibrations, non-polar molecules, such as O_2. An added advantage of this is that Raman spectroscopy can also monitor vibrations occurring in an aqueous phase, due to the low Raman cross section of H_2O.[284]

Raman spectroscopy also provides several unique advantages for probing aspects of heterogeneous catalysts,[285] particularly under *in situ* operating conditions.[286] (i) Raman spectroscopy is able operates in all phases (solid, liquid, gas, and mixtures), with minimal interference from non-adsorbed gas phase species; (ii) the technique operates over extremely large temperature ($0 < x < 828\ ^{\circ}\mathrm{C}$) and pressure ranges (UHV to >100 bar), and hence spectra under almost all relevant catalytic conditions may be collected; (iii) low frequency vibrations (fingerprint region spectra, $50 < x < 1100\ \mathrm{cm}^{-1}$, frequently obscured in FTIR spectra), where the vibrational bands of solid catalysts, such as M–O, M–OH, M=O and M–O–M vibrations, are readily observed, thus providing direct insight into the catalytic materials; and (iv) some of the most important reaction bonds in heterogeneous catalysis, such as metal–oxygen bonds, the O–O bond of various peroxides, and various metal–(hydro)peroxo ($M–O_x$) and metal-hydride vibrations, are Raman active. Despite these advantages, Raman spectroscopy has not yet reached the routine levels of UV-Vis and FT-IR, likely due to its persistent disadvantages, such as (i) poor sensitivity – only approximately one photon in 10^8 incident photons will be Raman-scattered, leading to time resolutions on the second timescale – and (2) fluorescence effects, which can mask potential weak Raman features. Although several methodologies, such as UV-Raman spectroscopy, are able to overcome both of these limitations, these remain outside the scope of this present review, and readers are directed to the review articles of Fan,[281] and Kim.[287]

2.6.1 Raman spectroscopy for the characterisation of Au catalysts. In common with all metals, metallic Au, as typically found in heterogeneous Au catalysts, does not itself possesses any Raman active modes that give rise to primary Raman bands. Despite this, Raman spectroscopy still offers unique opportunities to study the catalytic chemistry of supported Au particles. We note at this stage that the use of Au purely as a substrate for surface enhanced Raman spectroscopy (SERS),[288] or alternatively electrocatalytic SERS studies,[289] is largely beyond the scope of this review article. Nevertheless, examples of where the SERS-active Au nanoparticles act concurrently as SERS substrate and catalyst will be covered (*vide infra*). Similarly, electrocatalytic processes in which catalytically active elements are deposited onto SERS-active Au electrodes,[290,291] are also not covered when the active metal is not Au itself. Readers interested in the general area of SERS are directed to these other manuscripts.

2.6.2 Studying catalyst supports, and identifying metal–support interactions. In order to be employed as an active and stable heterogeneous catalyst, Au nanoparticles typically require deposition and immobilisation upon a suitable support material.[19] Relatively high surface area (mixed) metal oxides, such as TiO_2, Al_2O_3 Fe_2O_3 or SiO_2, or alternatively carbonaceous materials, such as activated carbon, graphene, graphite and carbon nanotubes (CNTs), are often employed (Fig. 24). Due to the selection rules for Raman spectroscopy, which favour vibrations from various metal–oxygen (M–O) and carbonaceous materials, and its particular advantages (*e.g.* fingerprint region analysis, *vide supra*), Raman spectroscopy is one of the most suitable and effective methodologies by which the composition of the support (species present, crystalline phase(s), non-crystalline surface phase) and its particular structure (defects, lattice vacancies) may be identified.[284,285] Indeed, the chemistry of (mixed) metal oxide catalysts and carbon-based (nano)materials are perhaps the fields where Raman spectroscopy has been most successfully employed. Although we will focus on particular examples of heterogeneous Au catalysts, readers interested in the more general subject area are directed to the recent, comprehensive reviews of Wachs (metal oxide catalysis)[284] and Ferrari[292] and Dresselhaus[293] (application of Raman for carbon-based materials).

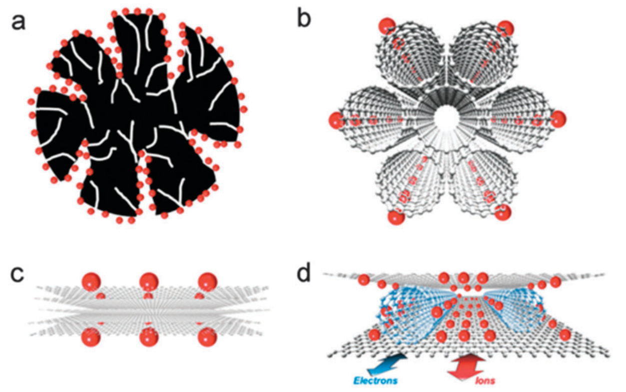

Fig. 24 Structural representation of various carbon-based nanomaterials, including (a) activated carbon, (b) single walled carbon nanotubes, (c) pristine graphene and (d) graphene/nanotube composites. Reproduced with permission from The Royal Society of Chemistry.[294]

Several established and emerging nanoparticle support materials are based on allotropes of carbon, including (i) activated carbon, (ii) graphene, (iii) graphene oxide, and (iv) carbon nanotubes. Indeed, given their unique structural, electronic and optical properties, coupled with their extremely high surface areas, mechanical and thermal strength, and tunable chemical properties (acidity, basicity *etc.*), it is unsurprising that carbon-based materials are such promising support materials.[295–297] Given that it also directly probes the lattice vibrations, Raman spectroscopy has emerged as an extremely sensitive method for probing the chemical, electronic and vibrational structure of several allotropes of carbon. Raman spectroscopy is also sensitive to the degree of graphitization in carbon materials.[298]

Moreover, Raman spectroscopy is a tremendously useful method by which the composition, structure and nature of various (mixed) metal oxides, regularly employed as supports for Au nanoparticles, can be probed. Indeed, as fingerprint region information can be obtained ($50 < x < 1100\ \mathrm{cm^{-1}}$), Raman spectroscopy is able to identify the M–O, M–OH, M$=$O and M–O–M vibrations of numerous metal oxides employed as Au nanoparticle supports, including TiO_2, Al_2O_3, CeO_2, and V_2O_5, amongst others.[284] It is a particularly suitable technique for studying metal oxides that possess many potential phases, such as iron oxide and vanadium oxides. Accordingly, Kozlova *et al.* employed Raman spectroscopy to determine the state and structure of the iron oxide support during CO oxidation catalysis.[299] Their results demonstrated that the optimal catalysis was observed when Au nanoparticles were deposited onto poorly crystallized iron oxide, containing a mixture of α-Fe_2O_3 and γ-Fe_2O_3 phases, and that the presence of the poorly crystalline γ-Fe_2O_3 phase was highly beneficial to catalytic activity. Zhu *et al.* were also able to employ Raman spectroscopy to understand how the composition and structure of their support materials (mixed titania and silica monoliths) varied upon increasing the amount of Ti in the monolith.[300] In this case, Raman spectroscopy was also key in identifying how the phase transformation of amorphous TiO_2 into highly crystalline anatase was positive for catalytic activity of the Au nanoparticles for CO oxidation.

In a series of manuscripts focused on total benzene oxidation over supported Au catalysts, Andreeva and colleagues regularly employed Raman spectroscopy. Their Au nanoparticles were typically supported on complex mixed metal oxides, including mixed oxides of V_2O_5/TiO_2, V_2O_5/ZrO_2, V_2O_5/CeO_2 and $V_2O_5/CeO_2/Al_2O_3$.[301–304] In each case, Raman spectroscopy was able to establish the composition of each support, and more critically, detect various amorphous phases that were otherwise undetectable by other bulk techniques, such as XRD. Interestingly, their studies also indicated a significant interaction between nanoparticles of Au and the V atoms of the support; a lengthening of the V$=$O bond (easily identified by Raman spectroscopy, as the position of a Raman mode is proportional to its bond order) was observed, and the addition of Au was also found to increase both the reducibility and reactivity of the VO_x units. This important interaction was proposed by the authors to be responsible for the ability of the Au-doped catalyst (Au–V_2O_5/CeO_2) to operate at substantially lower reaction temperatures than the Au-free analogues.

In addition to providing a suitable surface onto which various metal nanoparticles may be deposited, support materials, and metal oxides in particular, may also participate more intimately in the catalytic chemistry, either through direct participation (where the support is a co-catalyst, potentially responsible for the binding of reactants, the delivery of an component, or activation of a substrate), or through indirect participation through metal–support interactions.

Two notable examples of this are (i) the Mars–van-Krevelan mechanism, predominant in various catalyst based on reducible metal oxides, and (ii) how various metal oxide supports, particularly TiO_2 or CeO_2, are able to participate in oxidation reactions through the activation of gaseous O_2 on their defect sites. The second of these was very elegantly demonstrated with Raman spectroscopy, by Carrettin *et al.*[305] The authors demonstrated how both TiO_2 and Fe-doped TiO_2 were able to activate molecular oxygen on their defect sites, leading to the formation of both η^1-superoxide ($1123\ \mathrm{cm^{-1}}$) and peroxide ($969\ \mathrm{cm^{-1}}$) moieties. Although the support materials were inactive in the absence of nanoparticles of Au, they were able to deliver this activated oxygen to facilitate the oxidation reaction in the presence of Au. The authors were also able to utilise Raman spectroscopy, in addition to X-ray diffraction, to identify the positive role of doping TiO_2 with Fe; inclusion of iron led to an increase in the percentage of the rutile phase, known to have a higher density of oxygen vacancies, which the authors had found to be responsible for O_2 activation. Lee *et al.* also reported similar observations of O_2 activation over various defective metal oxide supports, including CeO_2.[306] In this case, the authors also observed an increase in oxygen vacancy concentration following Au deposition. We note that several reports in the literature have demonstrated how doping CeO_2 with various cations can lead to the creation of oxygen vacancies.

In addition to providing sites for oxygen activation, recent Raman measurements have also indicated that such defect sites may also behave as sites for selective Au deposition. Several reports have observed the quenching of oxygen vacancies visible in the Raman spectra of CeO_2 upon the deposition of Au, indicating that such defect sites may provide a route towards maximising dispersion of the noble metal during synthesis by anchoring the initial metal atoms. Nucleation around this initial nest atom is then likely.[307–309]

Metal–support interactions were also observed by Yang *et al.* who demonstrated that the deposition of Au onto Ti-containing hexagonal mesoporous silica (Ti-HMS) leads to a perturbation in the Ti–O–Si stretches present in Ti-HMS, and attributed this to the interaction between the Au nanoparticles and surface exposed Ti atoms. The authors later proposed this interaction to be responsible for the improved activity and selectivity of Au/Ti-HMS for the gas phase epoxidation of propylene with gaseous H_2 and O_2.[310] Comparable interactions between Au and Ce^{4+} cations were also reported by Laguna *et al.* In this case, the authors observed a shift in the F_{2g} signal of CeO_2 upon deposition of Au, which they attributed to an electronic interaction between the Au clusters and the metal oxide support.[307–309]

Interactions between Au and $Fe^{2+/3+}$ were also observed by Li *et al.*[311] During their studies of low temperature CO oxidation over FeO_x-supported Au nanoparticles, the authors demonstrated that a redox reaction from Fe^{3+} to Fe^{2+} was critical for the supported Au nanoparticles to display catalytic activity. This was identified through *in situ* Raman measurements of the catalyst, with alternating CO and O_2 feeds. The authors observed a colour change, related to the conversion of the Fe^{3+} ferrihydrite phase (bands at 380, 510, 710 and 1341 cm^{-1}) into Fe_3O_4 (Fe^{2+}, one band at 655 cm^{-1}) upon switching between O_2 and CO. Most notably, however, was the absence of this redox reaction in the absence of deposited Au nanoparticles, strongly indicating that the presence of Au on the FeO_x support facilitates this key reduction process. The authors accordingly provided the first evidenced that the interface between Au and the FeO_x support was essential for CO oxidation activity to be observed.

Similar indications that Au influences the redox behaviour of $Fe^{2+/3+}$ were also obtained by the team of Overbury.[312] In this case, Raman analysis indicated that the redox behaviour of $FePO_4$ (used as a support for Au) increased dramatically in the presence of the noble metal. By being able to perform the Raman measurements *in situ i.e.* in the presence of the reactant gasses (O_2, CO, mixtures) and at high temperatures, the authors were also able to identify previously unobserved Raman bands at 1611 cm^{-1}, which they subsequently attributed to the reduction of the $FePO_4$ support.

2.6.3 Probing nanoparticle-stabilising ligands. Although colloidal methodologies have been shown to be a particularly effective method of preparing small (2–6 nm) Au nanoparticles that exhibit excellent catalytic properties, ligands such as PVA or PVP, are typically required, in order to stabilise the nanoparticles against agglomeration during the synthesis procedure. Although stabilisation is essential for the success of the method, the presence of the ligands on the immobilised metal nanoparticles is highly detrimental to catalytic activity. With Raman spectroscopy, the group of Hutchings successfully monitored the effectiveness of various post-synthetic treatments (oxidative heat treatment, water reflux) to remove the layer of undesirable ligand from a 1 wt% Au/TiO_2 (P25) catalyst (Fig. 25).[313] In this case, Raman spectroscopy permitted a surface sensitive methodology by which the presence and concentration of surface-bound PVA could be identified, even following water reflux or upon high temperature heat treatment ($\leq$400 °C). Ansar *et al.* also performed similar analysis of organothiol-decorated Au nanoparticles. In this case, Raman spectroscopy demonstrated the complete removal homocysteine from the Au nanoparticles following $NaBH_4$-washing of the metal nanoparticles.[314] In both of these cases, a SERS contribution likely accounts for the very high ligand signals observed, despite their low concentration in the overall catalyst.

2.6.4 Monitoring catalyst preparation with Raman spectroscopy. Several important methodologies for the preparation of Au nanoparticle catalysts, such as impregnation, deposition–precipitation and sol-immobilisation, employ water as a relatively benign solvent. The role of water in each of these cases is to solubilise the required metal precursor (typically $HAuCl_4 \cdot xH_2O$, chloroauric acid) and to provide a suitable medium by which the solubilised metal precursor can interact with the desired catalyst support (as a slurry). Unfortunately, the presence of water seriously prohibits several vibrational spectroscopic techniques, with the notable exception of attenuated total reflection IR spectroscopy (ATR-IR). However, the low Raman cross section of water permits the measurement of Raman scattering even in an aqueous medium. This unique ability has allowed several research teams to monitor many aspects of Au catalyst preparation methodologies.

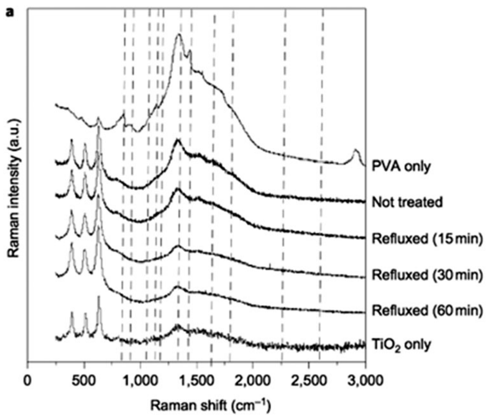

Fig. 25 Monitoring the presence of PVA present on a 1 wt% Au/TiO_2 catalyst by Raman spectroscopy. Figure reproduced with permission from Nature publishing.[313]

During their studies of the deposition–precipitation preparation methodology, the group of Louis employed Raman spectroscopy as a unique tool for following the speciation of Au throughout the synthesis.[315] By monitoring the two Raman bands of $HAuCl_4$ in an aqueous solution (322 and 347 cm^{-1}, attributed to the out-of-phase stretching mode and the symmetric stretching vibrations of Au–Cl in $[AuCl_4]^-$, respectively), the group were able to monitor the reduction of Au *in situ*, as a function of temperature, time and base (urea) concentration.[315] The same group subsequently utilised a similar approach to study the Au speciation of TiO_2- and Al_2O_3-supported Au following incipient wetness deposition.[316] Their studies revealed that following the impregnation step, Au was deposited in the form of Au chloride, and that post-deposition treatment with NH_3 was the most successful method of reducing Au^{3+} to Au^0, without overly removing Au from the material.

2.6.5 Au-catalysed reactions studied using *in situ* Raman spectroscopy. SERS is a phenomenon by which the Raman intensity of vibrations from a molecule close to a roughened metal surface are amplified by several orders of magnitude, through both electromagnetic and chemical enhancement mechanisms.[288,289] Despite the general usage of SERS being beyond the scope of this review, several recent articles have demonstrated how various Au-catalysed catalytic transformations can be monitored by SERS. In these cases, the Au-containing materials acts not only as heterogeneous catalyst, but also acts as

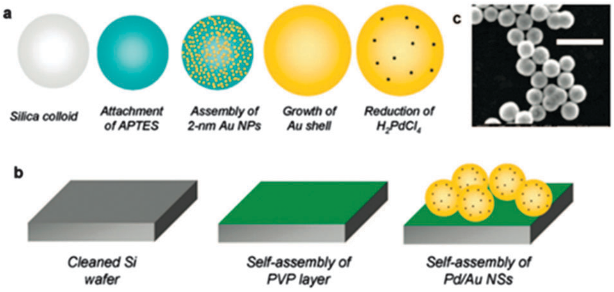

Fig. 26 Preparation procedure employed by Heck *et al.* to permit the production of SERS- and catalytically-active Pd/Au-nanoshell catalysts. Reprinted with permission from ref. 317. Copyright (2008) American Chemical Society.

a SERS substrate, substantially increasing the Raman scattering of both surface-bound intermediates, and liquid phase substrates near to the Au surface. In this manner, Heck and colleagues were able to monitor the catalytic hydrodechlorination of a chlorinated solvent, even in an aqueous medium.[317,318]

Their catalytic material, consisting of Pd islands grown on Au nanoshell films (Fig. 26), provided both the catalytic active sites, and also the SERS substrate required for enhancing the Raman scattering of various chemisorbed substrates and intermediates.

The SERS enhancement proved critical in allowing the authors to obtain suitable time resolution such that the reactions could be monitored *in situ*. The authors later extrapolated their approach to the study of biomass conversion, such as glycerol oxidation. In both cases, monitoring the reaction with Raman spectroscopy not only allowed various kinetic data to be obtained, but also proved critical in allowing various surface-bound intermediates, to be detected and followed throughout the time course. These observations have led to substantial new mechanistic insight into these two extremely interesting catalytic processes. Other comparable investigations were also recently performed, albeit for different catalytic reactions (typically the hydrogenation of 4-nitrobenzenethiol) (Fig. 27).[319,320]

3. A practical case: supported AuPd bimetallic nanoparticles synthesized by a range of preparation methods for the liquid phase oxidation of benzyl alcohol

The selective oxidation of alcohols to fine and specialty chemicals has attracted the attention of the academia and industry in the last 20 years.[321–323] The main issue with the current industrial processes for the selective oxidation of alcohols is the utilisation of stoichiometric inorganic reagents such as $K_2Cr_2O_7$, and the environmental concerns these chemical processes generate. Therefore, the development of new processes that prevent the use of toxic materials and substitute with new environmentally friendly routes such as the use of homogeneous and heterogeneous catalysts and green oxidants such as molecular oxygen, air or peroxides remain one of the key objectives of the current research.[324–326]

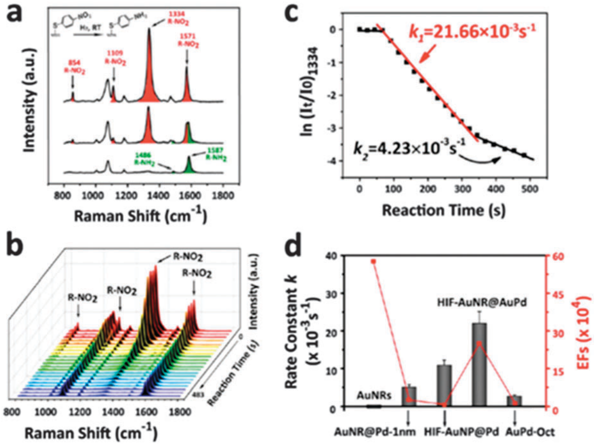

Fig. 27 (a) SERS spectra of the hydrogenation of chemisorbed 4-nitrothiophenol to 4-aminothiophenol over a Pd catalyst at different stages of the reaction. (b) Time online analysis performed by SERS measurements and (c) a first order rate plot based on the Raman intensity at 1334 cm^{-1} *versus* reaction time for the catalytic hydrogenation of 4-nitrothiophenol, and (d) normalized rate constants and SERS enhancement values of various Au-containing catalysts. Reprinted with permission from ref. 320. Copyright (2013) American Chemical Society.

There has been a substantial increase of interest in the synthesis of supported bimetallic Au–Pd and Au–Pt catalysts, and particularly their catalytic applications in the aerobic liquid phase oxidation of organic compounds such as alcohols, polyols.[4,9,15,95,327–335] The main reasons for the academic and industrial interest relies on the fact that (i) Au and Pd can form solid solutions in the whole range of Au/Pd atomic ratio; and (ii) the addition of second metal can alter the electronic and geometrical properties of the synthesized nanoparticle with the formation of alloy and core–shell structures. Therefore it is expected that catalytic activity, selectivity to the desired product and catalyst stability will be affected depending on the final morphology of the nanoparticles. In this review we present selected examples from the current literature for the oxidation of benzyl alcohol using supported Au–Pd nanoparticles under mild reaction conditions (Table 3). Where we focused our attention to describe the influence of the morphology of the Au–Pd nanoparticles in terms of catalytic performance, mechanistic and spectroscopic studies for elucidating the improved activity, control of selectivity and durability of the catalytic systems. Benzyl alcohol oxidation has attracted the scientific attention of many research groups due to the following reasons; it can be used as a model reaction to study the effect of catalytic performance in terms of activity, selectivity (a complex reaction network of products) and durability of the catalyst as it is shown in Scheme 3. Benzaldehyde is an important precursor in chemical industry and it is mainly produced *via* two chemical processes, (i) the hydrolysis of benzal chloride and (ii) toluene oxidation.[336,337] However, in both cases there are issues with poor selectivity and environmental concerns due to the chlorine contamination.

Table 3 Oxidation of benzyl alcohol using supported Au–Pd-based catalysts

Catalyst	T (°C)	Solvent	Conv. (%)	Sel% aldehyde	Ref.
Au–Pd/TiO_2	100	Solvent free	90	95	317
Au–Pd/C	120	Solvent free	80	65	320
Au–Pd/C	60	H_2O/NaOH	95	94	321
Au_{80}–Pd_{20}/C	60	$C_6H_5CH_3$	90	99	322
Au–Pd/PI	100	H_2O/Na_2CO_3	99	98	328
Au–Pd/SBA-15	80	Solvent-free	40	99	329
Au–Pd/Fe_3O_4	100	Solvent-free	65	94	336
Au–Pd/TiO_2	90	H_2O	75	96	337
Au–Pd/MgO	90	H_2O/K_2CO_3	75	95	338
Au@Pd@Ph-PMO	80	Solvent-free	100	93	340
Au@8Pd/SiO_2	90	Solvent-free	91	87	341
Au–Pd–GO/TiO_2	120	H_2O/NaOH	89	71	342

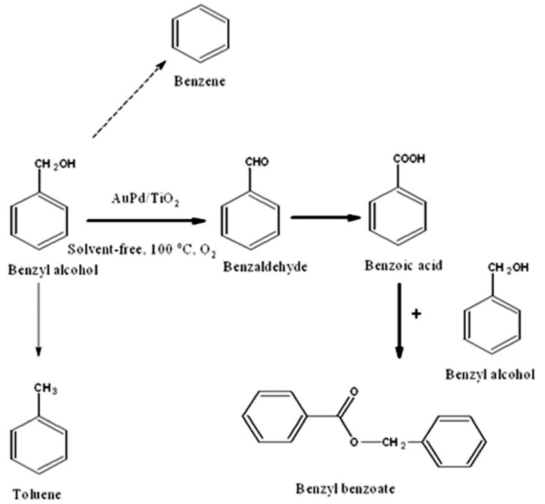

Scheme 3 Solvent-free oxidation of benzyl alcohol using Au–Pd-supported nanoparticles.

3.1 Au–Pd catalysts

Hutchings and co-workers[338] were one of the first groups to demonstrate the broad applicability of supported bimetallic Au–Pd nanoparticles synthesized by impregnation method in the solvent-free liquid phase oxidation of a range of alcohols. The synthesized catalysts (Au/Pd/TiO_2) were active and selective at solvent-free conditions using molecular oxygen as oxidant without the use of initiators (Scheme 3). Reported TOFs values of 269 000 h^{-1} showed the high efficiency of the bimetallic catalysts. The authors demonstrated by means of STEM/EDX and XPS that the high activity of the Au–Pd supported catalyst was due to the formation of supported Au core–Pd shell nanoparticles and the electronic promotion of Au for Pd (Fig. 28). In following studies, the influence of the Au–Pd weight ratio was studied and it was found that the most active catalyst was the one with Au–Pd weight ratio of 1/1, whereas the highest selectivity to benzaldehyde was observed with Au-rich catalysts.[339] In following studies Hutchings and co-workers investigated the synthesis of supported Au/Pd catalysts using colloidal methods, and showed the efficient aerobic oxidation of benzyl alcohol with very high TOFs at milder reaction conditions (120 °C).[340]

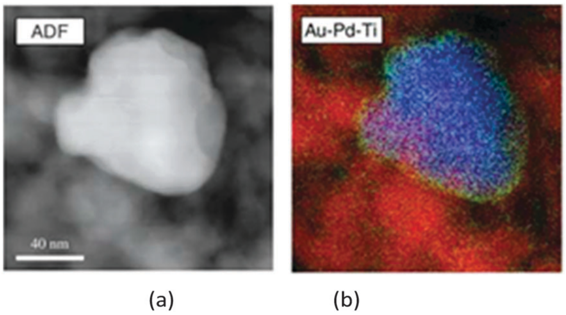

Fig. 28 (a) Montage showing the ADF-STEM image of a bimetallic particle and the corresponding reconstructed MSA-filtered Au/Pd/Ti composition map (Ti, red; Au, blue; and Pd, green). Reproduced with permission from ref. 338. Copyright 2006, The American Association for the Advancement of Science.

STEM-XDS and XPS studies confirmed the presence of random homogeneous alloys with metallic oxidation state for Au and the majority of Pd to be present in metallic state.

The higher activity of the supported Au–Pd catalysts synthesized by the colloidal method instead of the impregnation method was attributed primarily to the significant smaller particle size, narrow particle size distribution and metallic oxidation state of the two metals. A preparation approach for the synthesis of bimetallic hydrosols with the formation of core–shell structures, involving the sequential addition and reduction of the metal and deposition of the bimetallic sols on carbon and titania as the desired supports, was used for the synthesis of supported bimetallic Au/Pd nanoparticles.[341]

The catalytic activity for the aerobic oxidation of benzyl alcohol was carried out at mild conditions (120 °C, P_{O_2} = 10 bar), and the order of metal addition had a distinct effect on activity as well as selectivity.

The choice of support (carbon *versus* titania) was shown to affect significantly the activity and distribution of products, with carbon supported materials exhibiting an increase of activity by a factor of 2, and a lower selectivity to benzaldehyde at iso-conversion level compared to the analogous titania supported catalysts. Mechanistic studies showed that the reaction was zero order in oxygen and the oxidation of benzaldehyde was dependent on the concentration of oxygen at the surface.

A novel methodology was used for the synthesis of single-phase supported Au/Pd catalysts using a combination of a colloidal and seed-growth methods.[342] By comparison of the catalytic performance of supported Au/Pt and Au/Pd single phase nanoparticles (Fig. 29) in the selective oxidation of various primary alcohols (benzyl alcohol, cinnamyl alcohol and 1-octanol), the catalytic performance of Au/Pd catalysts was superior to analogue Au/Pt catalysts. A significant improvement in catalytic activity was discovered when water instead of toluene was used as the desired solvent. The reported TOFs values showed an increase by a factor of 1.5–6. In subsequent studies, the effect of Au_x/Pd_y molar ratio and the catalytic performance for a range of alcohol substrates was studied. They concluded that the most efficient Au–Pd composition was Au_{80}/Pd_{20}, which exhibited the highest catalyst activity.[343]

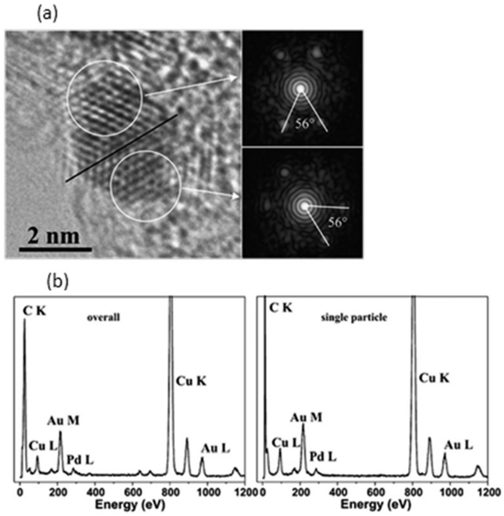

Fig. 29 (a) Representative HRTEM image of small particles from Au–Pd/AC and (b) overall EDX spectrum and the representative one for individual single particles for Au–Pd/AC. Reproduced with permission from ref. 342. Copyright 2006, Elsevier Inc.

The effect of Au–Pd molar ratio (1 : 7–7 : 1) in terms of catalytic activity was investigated for the liquid phase oxidation of benzyl alcohol at solvent-free conditions using colloidal methods.[344] The optimum catalytic performance was observed with Au–Pd 1 : 2 molar ratio and selectivity to benzaldehyde of 67% at 90% conversion. Characterization by STEM-HAADF analysis showed that the Au_x/Pd_y colloidal nanoparticles were in the 3–5 nm range, and when the composition was in the 2 : 1–1 : 2 Au–Pd ratio the particles were random homogeneous Au–Pd alloys with a face-centered cubic (fcc) structure, although variations were observed at high Au–Pd and Pd/Au ratios.

Mechanistic studies were performed for the oxidation of benzyl alcohol using supported Au/Pd alloy nanoparticles synthesized by sol-immobilization method. In the absence of oxygen benzyl alcohol was transformed into benzaldehyde and toluene at initial equal rates.[345] Introduction of oxygen significantly increased the rate of benzyl alcohol disappearance and appearance of benzaldehyde at the expense of toluene formation. It was found that at low partial pressures (below 3 bar of oxygen) rates are dependent on oxygen, suggesting that oxygen can participate in the reaction pathway as an adsorbed species. In subsequent studies the effect in terms of catalytic performance of acidic/basic supported Au/Pd nanoparticles was studied.[346] By varying the support from titania, niobium oxide, zinc oxide and magnesium oxide it was demonstrated the "switch off" of the disproportionation reaction and thereby the significant improvement in the selectivity to benzaldehyde (99%) at the expense of toluene could be achieved. The most suitable support to minimize the disproportionation reaction was magnesium oxide and zinc oxide.[347]

The utilization of microstructured reactors was investigated by Gavriilidis and co-workers in the liquid phase oxidation of benzyl alcohol at mild conditions (80–120 °C) using $Au/Pd/TiO_2$ catalysts.[356] The authors demonstrated that the continuous oxidation of benzyl alcohol is feasible and by optimizing reaction parameters 96% conversion with selectivity to benzaldehyde of 78% were obtained at 120 °C and 5 bar oxygen pressure. Moreover, they demonstrated the prospect of monitoring reactant/product species by using *in situ* Raman spectroscopy.

The effect of alloy or core–shell structure was investigated by synthesizing bimetallic Au/Pd colloids involving the sequential addition and reduction of the metal and deposition of the bimetallic colloids on carbon and titania.[89] STEM-HAADF imaging (Fig. 30) was employed for evaluating the particle size distribution as well as to monitor the spatial distribution within individual particles and it was concluded from these studies the formation of alloy Au/Pd particles when Au and Pd were mixed together where a core–shell structure was developed when the sequential addition and reduction of metals were used.

STEM-HAADF studies revealed that the supported Au/Pd nanoparticles consisted of a mixture of icosahedral, decahedral and cub-octahedral particles. In terms of catalytic activity the aerobic oxidation of benzyl alcohol could be achieved at mild conditions (80 °C, P_{O_2} = 10 bar) and the order of metal addition

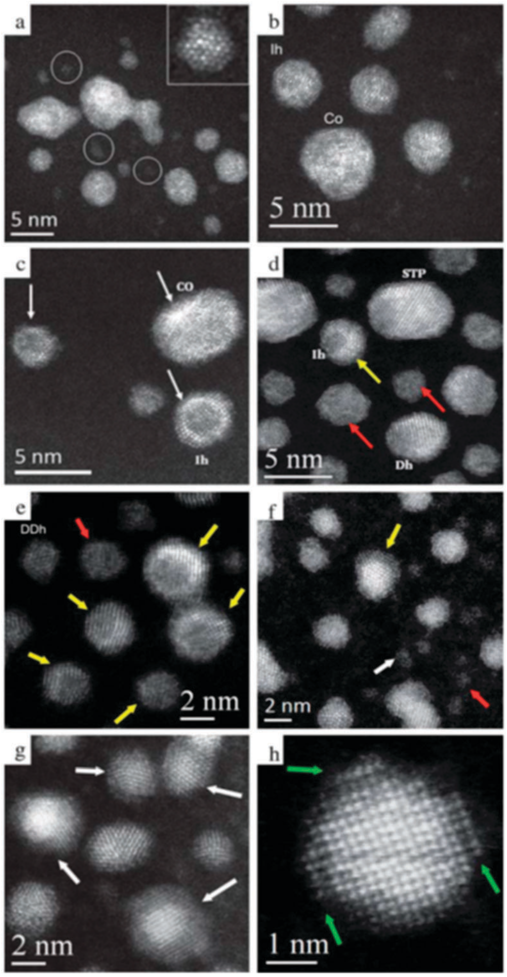

Fig. 30 Representative STEM-HAADF images of the starting colloids (a and b) a Au/Pd random alloy, (c–e) Pd core/Au shell particles and (f–h). Au_{core}/Pd_{shell} particles Reproduced with permission from ref. 89 Copyright 2011, The Royal Society of Chemistry.

had a marked effect. The most effective catalysts were in the presence of a Au_{core}/Pd_{shell} structure and TOFs up to 45 000 h^{-1} were reported at mild conditions (*e.g.* 80 °C). In subsequent studies the effect of heat treatment on the stability of these structures and catalytic performance were investigated.[348]

It was found that a mild calcination treatment (*e.g.* 200 °C) improved the catalytic activity due to the removal of the polymer layer around the Au/Pd particles, whereas a calcination treatment above 200 °C affected the final morphology of the Au/Pd particles dependent on the initial structure of the particles (alloy or core–shell) and the choice of support and led to a significant decrease in terms of activity. For example, Au/Pd particles with a random alloy structure did not show phase separation, whereas Pd_{core}–Au_{shell} and Au_{core}–Pd_{shell} started to show phase separation and the simultaneous presence of the initial structure and Au-rich particles with PdO particles. The authors concluded that in terms of optimizing catalytic performance it seems that not only an optimum particle size was required to achieve a good compromise between activity and selectivity but also an optimum ratio between PdO/Pd species was important. The beneficial interaction of Au and Pd in bimetallic catalysts was also demonstrated by Baiker and Marx by synthesizing bimetallic catalysts using a colloidal route, where the admixing of Pd to Au resulted in the synthesis of bimetallic nanoparticles in a narrow range (2.4–3.7 nm) and a Au rich core and a Pd rich shell.[349] The synthesized Au–Pd nanoparticles supported on polyaniline showed high activity in the liquid phase oxidation of benzyl alcohol and high selectivity to benzaldehyde (98%) in the presence of toluene as solvent and aqueous solution of NaOH.

Qiao and co-workers reported the synthesis of Au–Pd/SBA-15 material by impregnation and grafting methods.[350] By using the grafting method metal nanoparticles (5 nm mean particle size) were highly dispersed in mesoporous channels of SBA-15, showing high catalytic performance in the selective oxidation of benzyl alcohol to benzaldehyde at mild reaction conditions (80 °C, water as solvent and Na_2CO_3). It was demonstrated that agglomeration and leaching of metal nanoparticles was avoided by restricting the nanoparticles inside the mesopores of SBA-15, therefore leading to enhanced stability and reusability of Au–Pd/SBA-15. The effective confinement of Au–Pd nanoparticles was also reported by Y. Yang and co-workers, using SBA-16 as support. Au–Pd nanoparticles were supported on SBA-16 using an adsorption method. The authors demonstrated the synergistic effect of the bimetallic Au/Pd supported nanoparticles by showing enhanced catalytic performance of the Au–Pd catalyst compared to the Au and Pd monometallic catalysts. STEM and EDX studies were carried out and the alloyed structure of the bimetallic nanoparticles with Pd rich shell and Au core structure was shown.[351] A new methodology for synthesizing Au–Pd bimetallic catalysts was reported by Evangelisti and co-workers.[352] The methodology is based on the utilization of Au and Pd vapours as reagents either by simultaneous condensation or by separate evaporation of the two metals and subsequent mixing. The catalytic performance of the supported Au–Pd catalysts was tested in the aerobic oxidation of benzyl alcohol at mild conditions (60–100 °C, 1–5 bar of molecular oxygen) in organic solvent and solvent-free conditions. Au–Pd bimetallic catalysts synthesized by the simultaneous condensation method showed improved activity (98% conversion) than the corresponding monometallic catalysts (2–4% conversion) as well as the Au–Pd catalyst obtained by separate evaporation of the two metals (11–12% conversion with selectivities around 90% towards benzaldehyde). The authors carried out extensive characterizations by means of XAFS studies and observed that for the most active Au/Pd catalyst a clear charge transfer from Pd to Au by XANES data. Additional EXAFS data also showed that the Au–Pd bimetallic nanoparticles composed of an Au rich core surrounded by a Au–Pd alloyed shell. A new methodology for the synthesis of highly faceted, icosahedral Au–Pd core–shell nanoparticles was reported by Tilley and co-workers.[353] Their strategy was based on the utilization of a seed-mediated methodology, which allows independent control of nucleation and growth stage. In this way, the synthesis of Au–Pd core–shell nanoparticles with a variation of Pd thickness around the Au core particle was achieved. The synthesized nanoparticles were deposited onto activated carbon and their catalytic performance was carried out in the solvent-free aerobic oxidation of benzyl alcohol. The maximum activity occurred at a Pd shell thickness of 2.2 nm and they concluded that increasing the faceting of the particles an enhancement of activity as selectivity to benzaldehyde over 70% could be observed. The concept of this work relies on the fact that a very slow shell growth can be beneficial for future nanocrystal catalyst design.

An improved methodology for the synthesis of supported Au–Pd nanoalloys was reported by Hutchings and co-workers.[354–356] By using a simple excess anion modification of the impregnation method the synthesis of bimetallic nanoparticles with good control of particle size and composition was reported. In the new methodology, the presence of excess chloride ions facilitates the elimination of the larger ''Au-rich'' particles, increases the Au concentration of Au in the bimetallic particles and there is no size-dependent compositional variation in the individual bimetallic nanoparticles. Catalytic performance of the supported bimetallic catalysts with the new preparation method was carried out in the oxidation of benzyl alcohol oxidation. Comparison of catalytic activity with other well-known preparation methods, such as colloidal and impregnation methods showed the improved activity of the new supported Au–Pd catalyst by a factor of 1.3 and 6.5 respectively. The improved activity was mainly attributed due to the absence of ligand (stabiliser), removal of Cl and more precise control over the composition of Au and Pd in the nanoalloy particle. Catalytic stabilities of the supported Au–Pd nanoparticles prepared by the colloidal and modified impregnation methods were carried out using continuous flow systems and it was reported that the stability of the catalysts was depending on the experimental conditions used. For example the catalyst prepared by a colloidal method showed high sensitivity to reaction conditions. Deactivation of the catalyst was observed but by proper tuning the reaction conditions a reactivation protocol was established. In the case of the modified impregnated catalyst there was no deactivation profile.

M. Rossi and co-workers[357] studied the effect of Au–Pd atomic composition in the oxidation of benzyl alcohol by using a seed growth method for the synthesis of Au–Pd bimetallic nanoparticles. The preparation of bimetallic Au–Pd nanoparticles was based on the reduction of varying amounts of Pd over supported Au nanoparticles, a common methodology used by many research groups in the area of nanoparticle synthesis. The synthesised bimetallic nanoparticles were supported on Fe_3O_4 and SiO_2. Catalytic data showed that the catalytic activity was depending on the amount of Pd added as shell metal. The highest conversion of benzyl alcohol was achieved by using Au–Pd molar ratio of 10/1 (1 ML of Pd) with selectivity to benzaldehyde up to 80% at 60% conversion. Recyclability tests showed the good stability of the catalyst. Computational studies were carried out to explain the improvement of catalytic activity when Pd is added as a shell on a Au core metal. The computational studies showed that the adsorption of alcohol is improved with the utilisation of a Au_{core}–Pd_{shell} system (1 ML), therefore explaining the high catalytic activity observed with the synthesised Au_{core}–Pd_{shell} nanoparticles.

Li and co-workers[358] reported a novel green bioreductive approach for the synthesis of Au–Pd nanoparticles supported on TiO_2. They used cacumen platycladi (CP) as a bio-reducing agent, an example of plant extract as a natural factory for the biosynthesis of nanoparticles and without additional chemicals. The catalytic performance of a series of Au/Pd catalysts with different Au–Pd molar ratio was carried out for the solvent free oxidation of benzyl alcohol. Characterisation by TEM showed that the particle size was in the ranged of 8–18 nm and it was depending on the Au–Pd molar ratio. By increasing the Pd precursor concentration, the smaller the bimetallic particles formed. The nature of the bimetallic nanoparticles was verified by means of STEM and EDXS and the individual nanoparticles were alloy regardless of different Au–Pd molar ratio. In terms of oxidation state XPS analysis showed that both metals were completely reduced. The effect of Au–Pd molar ratio was studied and it was reported that higher conversion up to 70% than the monometallic Au/TiO_2 and Pd/TiO_2 was obtained with $Au–Pd/TiO_2$ catalysts with Au–Pd molar ratio in the range 1 : 2–2 : 1 and high selectivity to benzaldehyde around 90%. Reusability of the catalysts was carried out and the activity was remained constant after 7 cycles, indicating the high stability of the alloy catalysts. The same group in following studies reported the synthesis of 40 nm flower-shaped Au/Pd bimetallic nanoparticles supported on MgO by using a simultaneous bioreduction of Au and Pd metal precursors in the presence of ascorbic acid and cacumen platycladi leaf extract.[359] The role of ascorbic acid was to facilitate the formation flower-shaped NPs. TEM analysis and calculation of *d*-spacing from the lattice planes measured on single nanoparticles revealed value of 2.3 Å which is the mean value of the (111) planes of face-centered cubic (fcc) Au (2.36 Å) and Pd (2.25 Å) suggesting the formation of Au/Pd alloy nanoparticles. The catalytic performance of Au/Pd/MgO catalysts with a variation of Au–Pd molar ratio was studied and it was reported that the most active catalyst was the one with initial Au–Pd molar ratio of 1/1 with 72% conversion and 69% yield to benzaldehyde. As in the previous case, reusability tests were performed and a good stability was reported after 6 consecutive recycles.

Liu and co-workers[360] reported the synthesis of plasmonic photo-catalysts composed of bimetallic Au–Pd alloy nanoparticles on TiO_2 nanobelts and the catalytic performance for the aerobic oxidation of benzyl alcohol under visible light irradiation. The synthesis of TiO_2 nanobelts was carried out by synthesising as a first step $H_2Ti_3O_7$ nanobelts, following by calcination at 400–900 °C for obtaining TiO_2 nanobelts with different structures. The deposition of Au–Pd nanoparticles on the TiO_2 nanobelts was carried out by a deposition–precipitation method by urea followed by calcination. Characterisation by means of TEM showed that the supported Au–Pd nanoparticles were highly dispersed on the surface of the TiO_2 nanobelts with mean particles size of 2.1 nm and narrow particle size distribution. HRTEM analysis and calculation of lattice spacing showed that the particles were well-faceted and the measured lattice spacing was 2.32 Å, between the typical values of Au and Pd, indicating the formation of Au–Pd alloy nanoparticles (Fig. 31).

The catalytic performance of $Au–Pd/TiO_2$ nanobelts with different Au–Pd molar ratio was investigated and it was reported that the most active catalyst was the $Au_{0.75}$–$Pd_{0.25}/TiO_2$ nanobelt and higher than the monometallic Au and Pd supporting the fact that a promoting effect from alloying Au with Pd for aerobic oxidation under visible light irradiation exist. On the basis of the results reported, the authors proposed the following mechanism for the visible-light promoted aerobic oxidation of benzyl alcohol (Fig. 32).

In the first step plasmon activation of Au sites is responsible for the transfer of hot electrons to Pd sites and to the surface of the nanobelts. Then, the hot electrons in the Pd sites and the TiO_2 nanobelts can populate unoccupied orbitals of oxygen molecules and forming O–O-species. These species can cleave the O–H bond of the alcohol forming an alkoxide intermediate. In the second step, a rapid hydride transfer from C–H of the intermediate to the positively charged Au to form benzaldehyde

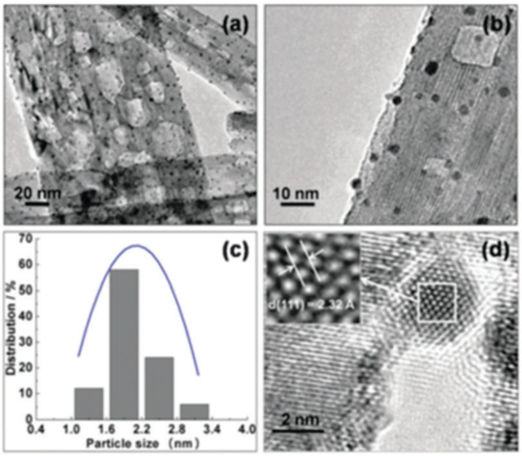

Fig. 31 Representative (a and b) TEM and (d) HRTEM images of $Au_{0.75}$–$Pd_{0.25}/TiO_2$ nanobelts and its corresponding particle size distribution. Reproduced with permission from ref. 360. Copyright 2015, The Royal Society of Chemistry.

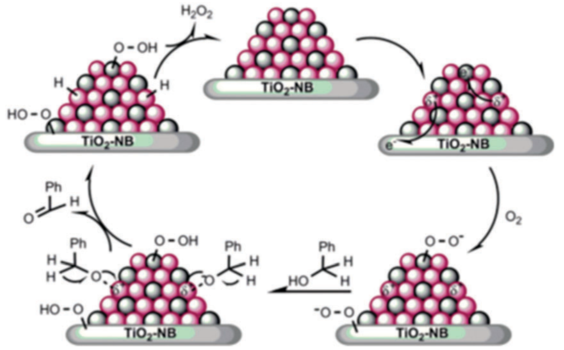

Fig. 32 Proposed mechanism for the aerobic oxidation of benzyl alcohol over the Au–Pd/TiO_2 nanobelts driven by visible light irradiation. Reproduced with permission from ref. 360 Copyright 2015, The Royal Society of Chemistry.

and Au–H species. Finally, *via* the elimination of the Au–H species and the recovery of the active sites the proposed cycle can be completed.

Qiu and co-workers[361] synthesised amphiphilic hollow mesoporous shells for encapsulating Au–Pd nanoparticles. The main advantage of using permeable shell is that allows fast diffusion of reactant and products and protects the core encapsulated nanoparticles from sintering, therefore providing a homogeneous micro-catalytic environment resulting in improvement in terms of catalytic stability and activity.

The synthetic protocol involves as a first step the synthesis of yolk–shell structured Au@Ph-PMO nanoparticles (composed of Ph-bridged periodic mesoporous organosilica shell and a single Au nano-sphere core) followed the growth of Pd nanoparticles on the surface of the Au nanosphere using a seed growth methodology (Scheme 4).

HRTEM and lattice fringe analysis showed the formation of Au_{core}/Pd_{shell} structures encapsulated by the shell. The catalytic performance of the bimetallic encapsulated nanoparticles was carried out using a range of alcohols including benzyl alcohol. High conversion up to 90% and selectivity to benzaldehyde (90%) was reported at mild conditions and reusability tests showed good high stability after 10 cycles without leaching of Au and Pd.

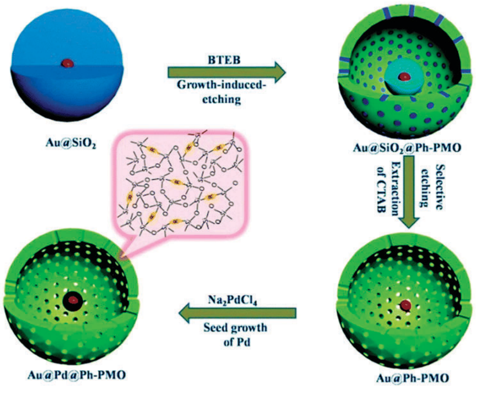

Scheme 4 Schematic illustration of the preparation of the amphiphilic nanoreactor Au@Pd@Ph-PMO. Reproduced with permission from ref. 361 Copyright 2015, The Royal Society of Chemistry.

A novel facile strategy for atomically-precise synthesis of supported Au_{core}–Pd_{shell} nanoparticles was reported by Lu and co-workers.[362] The chosen method for synthesising Au_{core}–Pd_{shell} nanoparticles was based on the combination of wet-chemistry and atomic layer deposition (ALD). Firstly, Au nanoparticles were deposited on SiO_2 using a deposition–precipitation method and then Pd was selectively deposited only on the surface of Au nanoparticles to exclusively form Au_{core}–Pd_{shell} nanoparticles and avoiding segregation of monometallic nanoparticles. Moreover, the thickness of Pd was tuned by varying the number of Pd ALD cycles (Fig. 33).

The selective deposition and uniform formation of the core–shell structures was demonstrated by means of HAADF/STEM analysis. Catalytic performance of the synthesised materials was evaluated using solvent-free aerobic oxidation of benzyl alcohol and it was reported that the catalytic activities showed volcano-type behaviour as a function of Pd shell thickness. The maximum reported activity (27 600 h^{-1}) and high selectivity to benzaldehyde (90%) was obtained with a Au_{core}–Pd_{shell} catalyst with a Pd shell thickness of 0.6–0.8 nm. The authors attributed this enhancement due to the optimised synergistic effect *via* both ensemble and electronic promotion. Recycling tests were performed to clarify the stability of the catalysts and leaching of

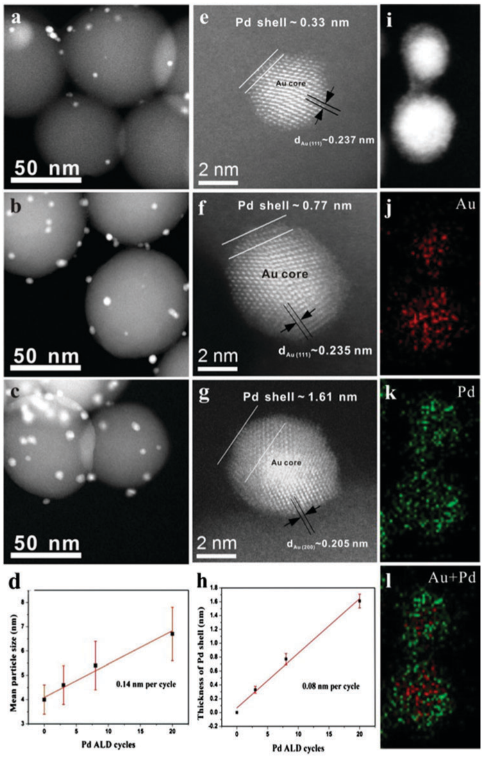

Fig. 33 HAADF-STEM images of different bimetallic catalysts at low and high magnifications: (a) and (e) Au@3Pd/SiO_2; (b) and (f) Au@8Pd/SiO_2; (c) and (g) Au@20Pd/SiO_2. (d) The growth of Au@Pd particle size as a function of Pd ALD cycles. (h) The Pd shell thickness as a function of Pd ALD cycles. (i) A lower magnification HAADF-STEM image of Au@8Pd/SiO_2, and corresponding EDX mapping images: (j) Au Lα1 and (k) Pd Lα1 signals, and (l) the reconstructed Au@Pd bimetallic composition image. Reproduced with permission from ref. 362 Copyright 2015, Elsevier.

metal nanoparticles was observed due to the weak interaction between metal nanoparticles and the inert SiO_2 support.

Hutchings and co-workers[363] synthesised supported Au/Pd nanoparticles on TiO_2 by graphene oxide sheets instead of PVA as a stabiliser when an immobilisation methodology was used (Scheme 5). Characterisation of the synthesised nanoparticles by means of HAADF-STEM analysis showed that the alloyed nanoparticles had a mean size of 5.2 nm and by using X-ray energy dispersive (XEDS) mapping confirmed the metal nanoparticles were Au–Pd alloys.

Catalytic performance of the synthesised materials was carried out in the aerobic oxidation of benzyl alcohol at 393 K and comparison with the analogous $Au–Pd_{PVA}/TiO_2$ catalysts showed a higher conversion (89%) and similar selectivity to benzaldehyde (70%). Moreover, the stability of the catalyst was investigated and minimal deactivation was observed, showing the high stability of the catalyst. The cause of the improved stability was due to the lower chemisorption of the products on the $Au–Pd–GO/TiO_2$ catalyst, indicating the importance of the presence of GO to inhibit the strong chemisorption from chemical species.

Villa and co-workers[251] used operando attenuated total reflectance (ATR) IR spectroscopy to elucidate the different catalytic activity supported of Au and Pd and bimetallic Au–Pd nanoparticles in the liquid-phase oxidation of benzyl alcohol. The evolution of surface species was monitored during the oxidation of benzyl alcohol using a batch-reactor cell and ATR-IR spectroscopy measurements were performed. The authors correlated the improved catalytic stability of the $Au–Pd/TiO_2$ with respect to Pd/TiO_2 with the decreased irreversible adsorption of products observed for the bimetallic AuPd system. The authors concluded that the presence of Au facilitates desorption of the products, especially benzoate species.

In summary it is evident that a large number of Au/Pd catalysts have been developed and reported for alcohol oxidation and especially the selective oxidation of benzyl alcohol. The majority of the bimetallic Au/Pd catalysts reported so far indicate that the majority of the research is focused on the following topics: effect of (i) particle size, (ii) shape, (iv) metal–support interaction, (v) alloy *versus* core–shell morphology and (vi) controlling the acid/base properties of the support. From these studies it is general accepted that the synthesis of nanoparticles of small particle size (2–6 nm) seems to be the most preferred particle size for obtaining high activity. Additionally, the synthesis of Au_{core}/Pd_{shell} nanoparticles can improve activity, however, the stability of the core–shell nanoparticles depends on reaction conditions and support. Few examples have shown the use of a third metal as a promoter to control activity and especially selectivity to benzaldehyde. More intense effort is needed in the following areas: (i) spectroscopic and characterisation studies to study and improve the understanding of the nature of active sites, (ii) mechanistic studies to reveal the formation of the synthesised nanoparticles by using *in situ* techniques (EXAFS/XANES, UV and SAXS), (iii) scaling up supported Au/Pd nanoparticles and (iv) the development of new methodologies based on continuous flow processes. Finally taking into account the successful utilisation of Au–Pd nanoparticles, another area of research that could be developed is the substitution of Au and Pd metals by the utilisation of cheaper and more abundant metals. A final point we should note is that more research should be focused on the prolong lifetime stability of bimetallic nanoparticles under "real" industrial conditions. Finally, it is evident that the examples of the Au–Pd nanoparticles presented in the literature can lead the way of development of novel bimetallic nanoparticles and can lead to the discovery of new materials and new catalytic applications.

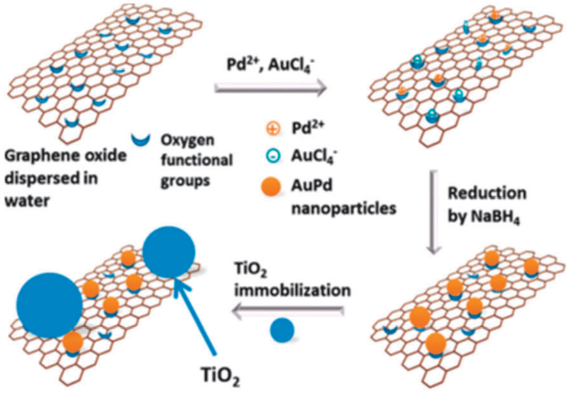

Scheme 5 Illustration of the Method Used for Preparing GO Stabilized Au–Pd nanoparticles on TiO_2 ($Au–Pd–GO/TiO_2$) Using a "ligand-free" sol-immobilization-type approach. Reproduced with permission from ref. 363 Copyright 2015, ACS.

4. Conclusion and perspective

Au has been studied for a long time as a catalyst for gas phase and liquid phase reactions. In the latter case, its catalytic activity has been shown to be advantageous especially in terms of selectivity and durability, compared to Pd or Pt catalysts. Many efforts have been devoted to the design of new Au catalysts able to enhance the activity, the selectivity to the desired product and to limit deactivation phenomena. Particular attentions have been paid the study of real nature of the active sites as it strongly affects catalytic activity and selectivity. Therefore, to understand the representative species different characterization techniques have to be utilised. In this review, we discuss and describe the methods that in our opinion give a representative understanding of the morphology and the surface properties of Au catalysts. Most of the examples reported involve the *ex situ* examination of the catalysts. Therefore, we consider that more effort should be now devoted to the study of the catalytic systems under realistic operating conditions. Most of the techniques we describe can be used under operating conditions. For example this can be carried out by using (i) *in situ*/*operando* extended X-ray absorption fine structure/X-ray absorption near edge structure (EXAFS/XANES), (ii) *in situ* FTIR measurements and finally (iii) by using environmental TEM. Recent developments have shown that XPS can be used at higher pressures.[364] As with *ex situ* characterisation an appropriate combination of techniques will yield the best results. The interest on the environmental TEM technique and combining techniques are rapidly growing due to the possibility of studying the morphology of nanostructured materials under simulated reaction conditions that will aid the understanding of formation of nanoparticles from the initial stage to the final morphology and therefore will lead to the design of better and more efficient catalysts.

References

1 M. Haruta, T. Kobayashi, H. Sano and N. Yamada, *Chem. Lett.*, 1987, 405.

2 M. Haruta, N. Yamada, T. Kobayashi and S. Iijima, *J. Catal.*, 1989, **115**, 301.

3 G. J. Hutchings, *J. Catal.*, 1985, **96**, 292.

4 A. S. K. Hashmi and G. J. Hutchings, *Angew. Chem., Int. Ed.*, 2006, **45**, 7896.

5 A. S. K. Hashmi, *Chem. Rev.*, 2007, **107**, 3180.

6 M. C. Daniel and D. Astruc, *Chem. Rev.*, 2004, **104**, 293.

7 G. C. Bond, C. Louis and D. T. Thompson, *Catalysis by Gold*, Imperial College Press, London, 2007.

8 B. Min and C. M. Friend, *Chem. Rev.*, 2007, **107**, 2709.

9 C. Della Pina, E. Falletta, L. Prati and M. Rossi, *Chem. Soc. Rev.*, 2008, **37**, 2077.

10 A. Corma and H. Garcia, *Chem. Soc. Rev.*, 2008, **37**, 2096.

11 J. C. Fierro-Gonzalez and B. C. Gates, *Chem. Soc. Rev.*, 2008, **37**, 2127.

12 M. Chen and D. W. Goodman, *Chem. Soc. Rev.*, 2008, **37**, 1860.

13 Z. Li, C. Brouwer and C. He, *Chem. Rev.*, 2008, **108**, 3239.

14 Y. Zhang, X. Cui, F. Shi and Y. Deng, *Chem. Rev.*, 2012, **112**, 2467.

15 M. Sankar, N. Dimitratos, P. J. Miedziak, P. P. Wells, C. J. Kiely and G. J. Hutchings, *Chem. Soc. Rev.*, 2012, **41**, 8099.

16 M. S. Chen and D. W. Goodman, *Catal. Today*, 2006, **111**, 22.

17 L. Prati, A. Villa, A. R. Lupini and G. M. Veith, *Phys. Chem. Chem. Phys.*, 2012, **14**, 2969.

18 A. Villa, M. Schiavoni and L. Prati, *Catal. Sci. Technol.*, 2012, **2**, 673.

19 X. Y. Liu, A. Wang, T. Zhang and C. Y. Mou, *Nano Today*, 2013, **8**, 403.

20 A. K. Datye, *J. Catal.*, 2003, **216**, 144.

21 C. Kiley, *Nat. Mater.*, 2010, **9**, 296.

22 J. C. Yang, M. W. Small, R. V. Grieshaber and R. G. Nuzzo, *Chem. Soc. Rev.*, 2012, **41**, 8179.

23 J. H. Sinfelt, G. H. Via and F. W. Lytle, *Catal. Rev.*, 1984, **26**, 81.

24 G. C. Bond, G. Webb and J. Evans, *EXAFS in the study of catalysts*, Royal Society of Chemistry, Cambridge, 1989.

25 J. Ryczkowski, *Catal. Today*, 2001, **68**, 263.

26 F. Zaera, *Chem. Soc. Rev.*, 2014, **43**, 7624.

27 J. L. Lemaitre, P. G. Menon and F. Delannay, in *Characterization of heterogeneous catalysts*, ed. F. Delannay, The measurement of catalyst dispersion, 1984, Marcel Dekker Inc, New York, ch. 7, p. 299.

28 R. Meyer, C. Lemire, S. K. Shaikhutdinov and H. J. Freund, *Gold Bull.*, 2004, **37**, 72.

29 C. S. Seney, B. M. Gutzman and R. H. Goddard, *J. Phys. Chem. C*, 2009, **113**, 74.

30 P. K. Jain, X. Huang, I. H. El-Sayed and M. A. El-Sayed, *Plasmonics*, 2007, **2**, 107.

31 R. Schlögl and S. B. Abd Hamid, *Angew. Chem., Int. Ed.*, 2004, **43**, 1628.

32 B. Freitag, S. Kujawa, P. M. Mul, J. Ringnalda and P. C. Tiemeijer, *Ultramicroscopy*, 2005, **102**, 209.

33 O. L. Krivanek, G. J. Corbin, N. Dellby, B. F. Elston, R. J. Keyse, M. F. Murfitt, C. S. Own, Z. S. Szilagyi and J. W. Woodruff, *Ultramicroscopy*, 2008, **108**, 179.

34 A. K. Datye and D. J. Smith, *Catal. Rev.*, 1992, **34**, 129.

35 W. Zhou and J. M. Thomas, *Curr. Opin. Solid State Mater. Sci.*, 2001, **5**, 75.

36 S. J. Pennycook and D. E. Jesson, *Ultramicroscopy*, 1991, **37**, 14.

37 L. J. Allen, A. J. D'Alfonso, B. Freitag and D. O. Klenov, *MRS Bull.*, 2012, **37**, 47.

38 P. A. Midgley and M. Weyland, *Ultramicroscopy*, 2003, **96**, 413.

39 B. W. Reed, D. G. Morgan, N. L. Okamoto, A. Kulkarni, B. C. Gates and N. D. Browning, *Ultramicroscopy*, 2009, **110**, 48.

40 W. D. Pyrz and D. J. Buttrey, *Langmuir*, 2008, **24**, 11350.

41 O. L. Krivanek, M. F. Chisholm, V. Nicolosi, T. J. Pennycook, G. J. Corbin, N. Dellby, M. F. Murfitt, C. S. Own, Z. S. Szilagyi, M. P. Oxley, S. T. Pantelides and S. J. Pennycook, *Nature*, 2010, **464**, 571.

42 C. R. Henry, *Prog. Surf. Sci.*, 2005, **80**, 92.

43 L. D. Marks, *Rep. Prog. Phys.*, 1994, **57**, 603.

44 P. M. Ajayan and L. D. Marks, *Phase Transitions*, 1990, **24–26**, 229.

45 J. Urban, H. Sack-Kongehl and K. Weiss, *Z. Phys. D*, 1993, **28**, 247.

46 M. J. Yacamán, J. A. Ascencio, H. B. Liu and J. Gardea-Torresdey, *J. Vac. Sci. Technol., B: Microelectron. Nanometer Struct.*, 2001, **19**, 1091.

47 C. L. Johnson, E. Snoeck, M. Ezcurdia, B. Rodríguez-González, I. Pastoriza-Santos, L. M. Liz-Marzán and M. J. Hÿtch, *Nat. Mater.*, 2008, **7**, 120.

48 D. Wang, A. Villa, F. Porta, L. Prati and D. Su, *J. Phys. Chem. C*, 2008, **112**, 8617.

49 K. Koga and K. Sugawara, *Surf. Sci.*, 2003, **529**, 23.

50 T. Akita, K. Tanaka, M. Kohyama and M. Haruta, *Surf. Interface Anal.*, 2008, **40**, 1760.

51 N. Shibata, A. Goto, K. Matsunaga, T. Mizoguchi, S. Findlay, T. Yamamoto and Y. Ikuhara, *Phys. Rev. Lett.*, 2009, **102**, 136105.

52 W. Zhou, I. E. Wachs and C. J. Kiely, *Curr. Opin. Solid State Mater. Sci.*, 2012, **16**, 10.

53 P. J. Miedziak, Z. Tang, T. E. Davies, D. I. Enache, J. K. Bartley, A. F. Carley, A. A. Herzing, C. J. Kiely, S. H. Taylor and G. J. Hutchings, *J. Mater. Chem.*, 2009, **19**, 8619.

54 D. Wang, A. Villa, F. Porta, D. Su and L. Prati, *Chem. Commun.*, 2006, 1956.

55 D. Gajan, K. Guillois, P. Delichère, J.-M. Basset, J.-P. Candy, V. Caps, C. Copéret, A. Lesage and L. Emsley, *J. Am. Chem. Soc.*, 2009, **131**, 14667.

56 M. Haruta, *Gold Bull.*, 2004, **37**, 27.

57 G. J. Hutchings, *Gold Bull.*, 2004, **37**, 3.

58 G. C. Bond and D. T. Thompson, *Catal. Rev.*, 1999, **41**, 319.

59 R. Arrigo, S. Wrabetz, M. E. Schuster, D. Wang, A. Villa, D. Rosenthal, F. Girsgdies, G. Weinberg, L. Prati, R. Schlögl and D. S. Su, *Phys. Chem. Chem. Phys.*, 2012, **14**, 10523.

60 J. A. Singh, S. H. Overbury, N. J. Dudney, M. Li and G. M. Veith, *ACS Catal.*, 2012, **2**, 1138.

61 C. Lemire, R. Meyer, S. Shaikhutdinov and H. J. Freund, *Angew. Chem., Int. Ed.*, 2004, **43**, 118.

62 H. J. Freund and G. Pacchioni, *Chem. Soc. Rev.*, 2008, **37**, 2224.

63 M. López-Haro, J. M. Cíes, S. Trasobares, J. A. Pérez-Omil, J. J. Delgado, S. Bernal, P. Bayle-Guillemaud, O. Stéphan, K. Yoshida, E. D. Boyes, P. L. Gai and J. J. Calvino, *ACS Nano*, 2012, **6**, 6812.

64 L. D. Marks, *Ultramicroscopy*, 1984, **12**, 237.

65 S. Bernal, F. J. Botana, J. J. Calvino, C. López-Cartes, J. A. Pérez-Omil and J. M. Rodríguez-Izquierdo, *Ultramicroscopy*, 1998, **72**, 135.

66 S. Bernal, R. T. Baker, A. Burrows, J. J. Calvino, C. J. Kiely, C. López-Cartes, J. A. Pérez-Omil and J. M. Rodríguez-Izquierdo, *Surf. Interface Anal.*, 2000, **29**, 411.

67 T. Wang, C. Lee and L. D. Schmidt, *Surf. Sci.*, 1985, **163**, 181.

68 D. Wang, A. Villa, D. Su, L. Prati and R. Schlögl, *ChemCatChem*, 2013, **5**, 2717.

69 A. Villa, D. Wang, G. M. Veith, F. Vindigni and L. Prati, *Catal. Sci. Technol.*, 2013, **3**, 3036.

70 K. Jiang, A. Eitan, L. S. Schadler, P. M. Ajayan, R. W. Siegel, N. Grobert, M. Mayne, M. Reyes-Reyes, H. Terrones and M. Terrones, *Nano Lett.*, 2003, **3**, 275.

71 J. Akola and H. Häkkinen, *Phys. Rev. B: Condens. Matter Mater. Phys.*, 2006, **74**, 165404.

72 K. P. McKenna and A. L. Shluger, *J. Phys. Chem. C*, 2007, **111**, 18848.

73 F. Porta, L. Prati, M. Rossi and G. Scari, *J. Catal.*, 2002, **211**, 464.

74 P. Serp and E. Castillejos, *ChemCatChem*, 2010, **2**, 41.

75 J. P. Tessonnier, O. Ersen, G. Weinberg, C. Pham-Huu, D. S. Su and R. Schlögl, *ACS Nano*, 2009, **3**, 2081.

76 X. Pan and X. Bao, *Chem. Commun.*, 2008, 6271.

77 Y. Wang, Z. Rong, Y. Wang, P. Zhang, Y. Wang and J. Qu, *J. Catal.*, 2015, **329**, 95.

78 M. D. Halls and H. B. Schlegel, *J. Phys. Chem. B*, 2002, **106**, 1921.

79 E. E. Santiso, M. K. Kostov, A. M. George, M. B. Nardelli and K. E. Gubbins, *Appl. Surf. Sci.*, 2007, **253**, 5570.

80 J. F. Creemer, S. Helveg, G. H. Hoveling, S. Ullmann, A. M. Molenbroek, P. M. Sarro and H. W. Zandbergen, *Ultramicroscopy*, 2008, **108**, 993.

81 K. L. Klein, I. M. Anderson and N. de Jonge, *J. Microsc.*, 2011, **242**, 117.

82 E. D. Boyes and P. L. Gai, *Ultramicroscopy*, 1997, **67**, 219.

83 J. B. Wagner, F. Cavalca, C. D. Damsgaard, L. D. L. Duchstein and T. W. Hansen, *Micron*, 2012, **43**, 1169.

84 T. Uchiyama, H. Yoshida, Y. Kuwauchi, S. Ichikawa, S. Shimada, M. Haruta and S. Takeda, *Angew. Chem., Int. Ed.*, 2011, **50**, 10157.

85 T. Kawasaki, K. Ueda, M. Ichihashi and T. Tanji, *Rev. Sci. Instrum.*, 2009, **80**, 113701.

86 H. Yoshida, Y. Kuwauchi, J. R. Jinschek, K. Sun, S. Tanaka, M. Kohyama, S. Shimada, M. Haruta and S. Takeda, *Science*, 2012, **335**, 317.

87 M. Tsuji, K. Ikedo, M. Matsunaga and K. Uto, *CrystEngComm*, 2012, **14**, 3411.

88 A. A. Herzing, M. Watanabe, J. K. Edwards, M. Conte, Z.-R. Tang, G. J. Hutchings and C. J. Kiely, *Faraday Discuss.*, 2008, **138**, 337.

89 R. C. Tiruvalam, J. C. Pritchard, N. Dimitratos, J. A. Lopez-Sanchez, J. K. Edwards, A. F. Carley, G. J. Hutchings and C. J. Kiely, *Faraday Discuss.*, 2011, **152**, 63.

90 P. Dash, T. Bond, C. Fowler, W. Hou, N. Coombs and R. W. J. Scott, *J. Phys. Chem. C*, 2009, **113**, 12719.

91 M. Heggen, M. Oezaslan, L. Houben and P. Strasser, *J. Phys. Chem. C*, 2012, **116**, 19073.

92 G. J. Hutchings, *Chem. Commun.*, 2008, 1148.

93 H. Zhang and N. Toshima, *Catal. Sci. Technol.*, 2013, **3**, 268.

94 Q. He, P. J. Miedziak, L. Kesavan, N. Dimitratos, M. Sankar, J. A. Lopez-Sanchez, M. M. Forde, J. K. Edwards, D. W. Knight, S. H. Taylor, C. J. Kiely and G. J. Hutchings, *Faraday Discuss.*, 2013, **162**, 365.

95 A. Villa, D. Wang, D. S. Su and L. Prati, *Catal. Sci. Technol.*, 2015, **5**, 55.

96 D. Ferrer, A. Torres-Castro, X. Gao, S. Sepúlveda-Guzmán, U. Ortiz-Méndez and M. José-Yacamán, *Nano Lett.*, 2007, **7**, 1701.

97 D. Wang, A. Villa, P. Spontoni, D. S. Su and L. Prati, *Chem. – Eur. J.*, 2010, **16**, 10007.

98 R. E. Benfield, A. Filipponi, D. T. Bowron, R. J. Newport and S. J. Gurman, *J. Phys.: Condens. Matter*, 1994, **9**, 8429.

99 D. C. Koningsberger and R. Prins, *X-ray absorption- Principles, Applications, Techniques of EXAFS, SEXAFS and XANES*, John Wiley & Sons, New York, 1988.

100 J. W. Watkins II, R. C. Elder, B. Greene and D. W. Darnall, *Inorg. Chem.*, 1987, **26**, 1147.

101 J. T. Miller, A. J. Kropf, Y. Zha, J. R. Regalbuto, L. Delannoy, C. Louis, E. Bus and J. A. van Bokhoven, *J. Catal.*, 2006, **240**, 222.

102 J. Guzman and B. C. Gates, *J. Catal.*, 2004, **226**, 111.

103 V. Schwartz, D. R. Mullins, W. F. Yan, B. Chen, S. Dai and S. H. Overbury, *J. Phys. Chem. B*, 2004, **108**, 15782.

104 M. Haruta, *Catal. Today*, 1997, **36**, 153.

105 R. Zanella, S. Giorgio, C. R. Henry and C. Louis, *J. Phys. Chem. B*, 2002, **106**, 7634.

106 G. M. Veith, A. R. Lupini, S. N. Rashkeev, S. J. Pennycook, D. R. Mullins, V. Schwartz, C. A. Bridges and N. J. Dudney, *J. Catal.*, 2009, **262**, 92.

107 J. Sá, A. Goguet, S. F. R. Taylor, R. Tiruvalam, C. J. Kiely, M. Nachtegaal, G. J. Hutchings and C. Hardacre, *Angew. Chem., Int. Ed.*, 2011, **50**, 8912.

108 A. Carlsson, A. Puig-Molina and T. V. W. Janssens, *J. Phys. Chem. B*, 2006, **110**, 5286.

109 M. Shekhar, J. Wang, W.-S. Lee, W. D. Williams, S. M. Kim, E. A. Stach, J. T. Miller, W. N. Delgass and F. H. Ribeiro, *J. Am. Chem. Soc.*, 2012, **134**, 4700.

110 M. Shekhar, J. Wang, W.-S. Lee, M. Cem Akatay, E. A. Stach, W. Nicholas Delgass and F. H. Ribeiro, *J. Catal.*, 2012, **293**, 94.

111 R. Carrasquillo-Flores, I. Ro, M. D. Kumbhalkar, S. Burt, C. A. Carrero, A. C. Alba-Rubio, J. T. Miller, I. Hermans, G. W. Huber and J. A. Dumesic, *J. Am. Chem. Soc.*, 2015, **137**, 10317.

112 J. H. Yang, J. D. Henao, M. C. Raphulu, Y. Wang, T. Caputo, A. J. Groszek, M. C. Kung, M. S. Scurrell, J. T. Miller and H. H. Kung, *J. Phys. Chem. B*, 2005, **109**, 10319.

113 E. Bus and J. A. van Bokhoven, *J. Phys. Chem. C*, 2007, **111**, 9761.

114 J. T. Calla and R. J. Davis, *J. Phys. Chem. B*, 2005, **109**, 2307.

115 L. Delannoy, N. Weiher, N. Tsapatsaris, A. M. Beesley, L. Nchari, S. L. M. Schroeder and C. Louis, *Top. Catal.*, 2007, **44**, 263.

116 J. A. Rodriguez, R. Si, J. Evans, W. Xu, J. C. Hanson, J. Tao and Y. Zhu, *Catal. Today*, 2015, **240**, 229.

117 M. Meire, P. Tack, K. De Keukeleere, L. Balcaen, G. Pollefeyt, F. Vanhaecke, L. Vincze, P. Van Der Voort, I. Van Driessche and P. Lommens, *Spectrochim. Acta, Part B*, 2015, **110**, 45.

118 G. M. Veith, A. R. Lupini and N. J. Dudney, *J. Phys. Chem. C*, 2009, **113**, 269.

119 D. E. Ramaker and D. C. Koningsberger, *Phys. Chem. Chem. Phys.*, 2010, **12**, 5514.

120 N. Weiher, E. Bus, L. Delannoy, C. Louis, D. E. Ramaker, J. T. Miller and J. A. van Bokhoven, *J. Catal.*, 2006, **240**, 100.

121 N. Weiher, A. M. Beesley, N. Tsapatsaris, L. Delannoy, C. Louis, J. A. van Bokhoven and S. L. M. Schroeder, *J. Am. Chem. Soc.*, 2007, **129**, 2240.

122 J. A. van Bokhoven, C. Louis, J. T. Miller, M. Tromp, O. V. Safonova and P. Glatzel, *Angew. Chem., Int. Ed.*, 2006, **45**, 4651.

123 J. J. Bravo-Suarez, K. K. Bando, J. Lu, T. Fujitani and S. T. Oyama, *J. Catal.*, 2008, **255**, 114.

124 E. Bus, R. Prins and J. A. van Bokhoven, *Phys. Chem. Chem. Phys.*, 2007, **9**, 3312.

125 A. Maclennan, A. Banerjee, Y. Hu, J. T. Miller and R. W. J. Scott, *ACS Catal.*, 2013, **3**, 1411.

126 A. Zwijnenburg, A. Goossens, W. G. Sloof, M. W. J. Crajé, A. M. van der Kraan, L. J. de Jongh, M. Makkee and J. A. Moulijn, *J. Phys. Chem. B*, 2002, **106**, 9853.

127 E. D. Park and J. S. Lee, *J. Catal.*, 1999, **186**, 1.

128 Q. Fu, H. Saltsburg and M. Flytzani-Stephanopoulos, *Science*, 2003, **301**, 935.

129 M. Comotti, W. C. Li, B. Spliethoff and F. Schüth, *J. Am. Chem. Soc.*, 2006, **128**, 917.

130 S. Arrii, F. Morfin, A. J. Renouprez and J. L. Rousset, *J. Am. Chem. Soc.*, 2004, **126**, 1199.

131 B. Schumacher, V. Plzak, J. Cai and R. J. Behm, *Catal. Lett.*, 2005, **101**, 215.

132 J. Radnik, C. Mohr and P. Claus, *Phys. Chem. Chem. Phys.*, 2003, **5**, 172.

133 S. Schimpf, M. Lucas, C. Mohr, U. Rodemerck, A. Brücker, J. Radnik, H. Hofmeister and P. Claus, *Catal. Today*, 2002, **72**, 63.

134 P. Claus, A. Brückner, C. Mohr and H. Hofmeister, *J. Am. Chem. Soc.*, 2000, **122**, 11430.

135 G. M. Veith, A. R. Lupini, S. J. Pennycook, G. W. Ownby and N. J. Dudney, *J. Catal.*, 2005, **231**, 151.

136 Y. F. Han, Z. Zhong, K. Ramesh, F. Chen and L. Chen, *J. Phys. Chem. C*, 2007, **111**, 3163.

137 M. P. Casaletto, A. Longo, A. Martorana, A. Prestianni and A. M. Venezia, *Surf. Interface Anal.*, 2006, **38**, 215.

138 M. P. Casaletto, A. Longo, A. M. Venezia, A. Martorana and A. Prestianni, *Appl. Catal., A*, 2006, **302**, 309.

139 L. C. Wang, Y. M. Liu, M. Chen, Y. Cao, H. Y. He and K. N. Fan, *J. Phys. Chem. C*, 2008, **112**, 6981.

140 A. Villa, C. E. Chan-Thaw, G. M. Veith, K. L. More, D. Ferri and L. Prati, *ChemCatChem*, 2011, **3**, 1612.

141 D. Horváth, L. Toth and L. Guczi, *Catal. Lett.*, 2000, **67**, 117.

142 M. G. Mason, *Phys. Rev. B: Condens. Matter Mater. Phys.*, 1983, **27**, 748.

143 B. Richter, H. Kuhlenbeck, H.-J. Freund and P. S. Bagus, *Phys. Rev. Lett.*, 2004, **93**, 026805.

144 D. C. Lim, I. Lopez-Salido, R. Dietsche, M. Bubek and Y. D. Kim, *Chem. Phys.*, 2006, **330**, 441.

145 D. E. Ramaker, M. Teliska, Y. Zhang, A. Y. Stakheev and D. C. Koningsberger, *Phys. Chem. Chem. Phys.*, 2003, **5**, 4492.

146 D. C. Koningsberger, J. de Graaf, B. L. Mojet, D. E. Ramaker and J. T. Miller, *Appl. Catal., A*, 2000, **191**, 205.

147 S. Zafeiratos and S. Kennou, *Surf. Sci.*, 1999, **443**, 238.

148 G. Moretti, *J. Electron Spectrosc. Relat. Phenom.*, 1998, **95**, 95.

149 G. K. Wertheim, *Phys. Rev. B: Condens. Matter Mater. Phys.*, 1987, **36**, 9559.

150 D. Teschner, J. Borsodi, A. Wootsch, Z. Révay, M. Hävecker, A. Knop-Gericke, S. D. Jackson and R. Schlögl, *Science*, 2008, **320**, 86.

151 D. E. Starr, Z. Liu, M. Hävecker, A. Knop-Gericke and H. Bluhm, *Chem. Soc. Rev.*, 2013, **42**, 5833.

152 E. J. Crumlin, Z. Liu, H. Bluhm, W. Yang, J. Guo and Z. Hussain, *J. Electron Spectrosc. Relat. Phenom.*, 2015, **200**, 264.

153 P. Jiang, S. Porsgaard, F. Borondics, M. Köber, A. Caballero, H. Bluhm, F. Besenbacher and M. Salmeron, *J. Am. Chem. Soc.*, 2010, **132**, 2858.

154 A. Y. Klyushin, T. C. R. Rocha, M. Hävecker, A. Knop-Gericke and R. Schlögl, *Phys. Chem. Chem. Phys.*, 2014, **16**, 7881.

155 E. A. Willneff, S. Braun, D. Rosenthal, H. Bluhm, M. Hävecker, E. Kleimenov, A. Knop-Gericke, R. Schlögl and S. L. M. Schroeder, *J. Am. Chem. Soc.*, 2006, **128**, 12052.

156 B. Henderson and G. F. Imbusch, *Optical Spectroscopy of Inorganic Solids*, Clarendon Press, Oxford, 1989.

157 E. Matijevic, *Curr. Opin. Colloid Interface Sci.*, 1996, **1**, 176.

158 W. Haiss, N. T. K. Thanh, J. Aveyard and D. G. Fernig, *Anal. Chem.*, 2007, **79**, 4215.

159 M. Zimbone, L. Calcagno, G. Messina, P. Baeri and G. Compagnini, *Mater. Lett.*, 2011, **65**, 2906.

160 H. Tsunoyama, N. Ichikuni, H. Sakurai and T. Tsukuda, *J. Am. Chem. Soc.*, 2009, **131**, 7086.

161 W. Guo, R. Pleixats and A. Shafir, *Chem. – Asian J.*, 2015, **10**, 2437.

162 W. Deng, C. Carpenter, N. Yi and M. Flytzani-Stephanopoulos, *Top. Catal.*, 2007, **44**, 199.

163 P. Marturano, L. Drozdovâ, G. D. Pirngruber, A. Kogelberger and R. Prins, *Phys. Chem. Chem. Phys.*, 2001, **2**, 5585.

164 A. N. Pestryakov, V. V. Lunin, A. N. Kharlanov, D. I. Kochubey, N. Bogdanchikova and A. Y. Stakheev, *J. Mol. Struct.*, 2002, **642**, 129.

165 K. Esumi, A. Suzuki, A. Yamahira and K. Torigoe, *Langmuir*, 2000, **16**, 2604.

166 C. L. Bianchi, P. Canton, N. Dimitratos, F. Porta and L. Prati, *Catal. Today*, 2005, **102–103**, 203.

167 A. Villa, C. E. Chan-Thaw and L. Prati, *Appl. Catal., B*, 2010, **96**, 541.

168 L. H. S. Gasparotto, A. C. Garcia, J. F. Gomes and G. Tremiliosi-Filho, *J. Power Sources*, 2012, **218**, 73.

169 J. Lin, W. Li, C. Liu, P. Huang, M. Zhu, Q. Gec and G. Li, *Nanoscale*, 2015, **7**, 13663.

170 T. Huang, F. Meng and L. Qi, *J. Phys. Chem. C*, 2009, **113**, 13636.

171 C. J. Murphy, T. K. Sau, A. M. Gole, C. J. Orendorff, J. Gao, L. Gou, S. E. Hunyadi and T. Li, *J. Phys. Chem. B*, 2005, **109**, 13857.

172 S. Lin, M. Li, E. Dujardin, C. Girard and S. Mann, *Adv. Mater.*, 2005, **17**, 2553.

173 C. Lin, K. Tao, D. Hua, Z. Ma and S. Zhou, *Molecules*, 2013, **18**, 12609.

174 A. M. Alkilany, A. I. Bani Yaseen and M. H. Kailani, *J. Nanomater.*, 2015, **16**, 1.

175 R. Fenger, E. Fertitta, H. Kirmse, A. F. Thünemann and K. Rademann, *Phys. Chem. Chem. Phys.*, 2012, **14**, 9343.

176 W.-G. Jia, Y.-C. Dai, H. N. Zhang, X. Lu and E.-H. Sheng, *RSC Adv.*, 2015, **5**, 29491.

177 K. Y. Lee, Y. W. Lee, J. H. Lee and S. W. Han, *Colloids Surf., A*, 2010, **372**, 146.

178 M. Nemanashi and R. Meijboom, *Langmuir*, 2015, **31**, 9041.

179 A. Primo, T. Marina, A. Corma, R. Molinari and H. García, *J. Am. Chem. Soc.*, 2011, **133**, 6930.

180 X. Ke, X. Zhang, J. Zhao, S. Sarina, J. Barry and H. Zhu, *Green Chem.*, 2013, **15**, 236.

181 B. M. Weckhuysen and R. A. Schoonheydt, *Catal. Today*, 1999, **49**, 441.

182 P. Saikia, A. T. Miah, B. Malakar and A. Bordoloi, *Indian Journal of Materials Science*, 2015, **2015**, DOI: 10.1155/2015/658346.

183 S. Tsunekawa, T. Fukuda and A. Kasuya, *J. Appl. Phys.*, 2000, **87**, 1318.

184 Y. Liu, H. Tsunoyam, T. Akita and T. Tsukuda, *Chem. Commun.*, 2010, **46**, 550.

185 X. Wang, C. E. Egan, M. Zhou, K. Prince, D. R. G. Mitchell and R. A. Caruso, *Chem. Commun.*, 2007, 3060.

186 A. Villa, N. Dimitratos, C. E. Chan-Thaw, C. Hammond, L. Prati and G. J. Hutchings, *Acc. Chem. Res.*, 2015, **48**, 1403.

187 C. Li and Y. Yamauchi, *Phys. Chem. Chem. Phys.*, 2013, **15**, 3490.

188 M.-L. Wu, D.-H. Chen and T.-C. Huang, *Langmuir*, 2001, **17**, 3877.

189 N. Toshima and T. Yonezawa, *New J. Chem.*, 1998, 1179.

190 G. Schmid, H. West, J.-O. Malm, J.-O. Bovin and C. Grenthe, *Chem. – Eur. J.*, 1996, **2**, 1099.

191 A. Calagua, H. Alarcon, F. Paraguay and J. Rodriguez, *Adv. Nanopart.*, 2015, **4**, 116.

192 C. Wang, S. Peng, R. Chan and S. Sun, *Small*, 2009, **5**, 567.

193 P. R. Griffiths and J. A. de Haseth, *Fourier Transform Infrared Spectrometry*, John Wiley & Sons, New York, 1986.

194 G. P. Williams, *J. Phys.: Condens. Matter*, 2001, **13**, 11367.

195 D. S. Bethune, M. D. Williams and C. Luntz, *J. Chem. Phys.*, 1988, **88**, 3322.

196 M. Mihaylov, H. Knozinger, K. Hadjiivanov and B. C. Gates, *Chem. Ing. Tech.*, 2007, **79**, 795.

197 G. M. Lari, E. Nowicka, D. J. Morgan, S. A. Kondrat and G. J. Hutchings, *Phys. Chem. Chem. Phys.*, 2015, **17**, 23236.

198 P. Hollins, *Surf. Sci. Rep.*, 1992, **16**, 51.

199 K. I. Hadjiivanov and G. N. Vayssilov, *Adv. Catal.*, 2002, **47**, 307.

200 P. Concepcion, S. Carrettin and A. Corma, *Appl. Catal., A*, 2006, **307**, 42.

201 M. Moskovits and J. E. Hulse, *Surf. Sci.*, 1978, **78**, 397.

202 F. Boccuzzi, A. Chiorino, M. Manzoli, P. Lu, T. Akita, S. Ichikawa and M. Haruta, *J. Catal.*, 2001, **202**, 256.

203 G. Martra, *Appl. Catal., A*, 2000, **200**, 275.

204 F. Boccuzzi, A. Chiorino, S. Tsubota and M. Haruta, *J. Phys. Chem.*, 1996, **100**, 3625.

205 J. D. Grunwaldt and A. Baiker, *J. Phys. Chem. B*, 1999, **103**, 1002.

206 G. Z. Wulff, *Z. Kristallogr.*, 1901, **34**, 449.

207 G. C. Bond and D. T. Thompson, *Gold Bull.*, 2000, **33**, 41.

208 H. Huber, D. McIntosh and G. A. Ozin, *Inorg. Chem.*, 1977, **16**, 975.

209 A. Chiorino, M. Manzoli, F. Menegazzo, M. Signoretto, F. Vindigni, F. Pinna and F. Boccuzzi, *J. Catal.*, 2009, **262**, 169.

210 F. Menegazzo, M. Manzoli, A. Chiorino, F. Boccuzzi, T. Tabakova, M. Signoretto, F. Pinna and N. Pernicone, *J. Catal.*, 2006, **237**, 431.

211 F. Menegazzo, F. Pinna, M. Signoretto, V. Trevisan, F. Boccuzzi, A. Chiorino and M. Manzoli, *Appl. Catal., A*, 2009, **356**, 31.

212 V. A. Bondzie, S. C. Parker and C. T. Campbell, *Catal. Lett.*, 1999, **63**, 143.

213 F. Menegazzo, F. Pinna, M. Signoretto, V. Trevisan, F. Boccuzzi, A. Chiorino and M. Manzoli, *ChemSusChem*, 2008, **1**, 320.

214 T. Tabakova, F. Boccuzzi, M. Manzoli and D. Andreeva, *Appl. Catal., A*, 2003, **252**, 385.

215 M. Valden, X. Lai and D. W. Goodman, *Science*, 1998, **281**, 1647.

216 D. Tibiletti, A. Amieiro-Fonseca, R. Burch, Y. Chen, J. M. Fisher, A. Goguet, C. Hardacre, P. Hu and D. Thompsett, *J. Phys. Chem. B*, 2005, **109**, 22553.

217 P. S. Bagus and G. Pacchioni, *J. Phys.: Conf. Ser.*, 2008, **117**, 012003.

218 C. Binet, M. Daturi and J. C. Lavalley, *Catal. Today*, 1999, **50**, 207.

219 A. Goguet, R. Burch, Y. Chen, C. Hardacre, P. Hu, R. W. Joyner, F. C. Meunier, B. S. Mun, A. Thompsett and D. Tibiletti, *J. Phys. Chem. C*, 2007, **111**, 16927.

220 T. Akita, M. Okumura, K. Tanaka, M. Kohyama and M. Haruta, *Catal. Today*, 2006, **117**, 62.

221 V. V. Pushkarev, V. I. Kovalchuk and J. L. d'Itri, *J. Phys. Chem. B*, 2004, **108**, 5341.

222 M. Manzoli, G. Avgouropoulos, T. Tabakova, J. Papavasiliou, T. Ioannides and F. Boccuzzi, *Catal. Today*, 2008, **138**, 239.

223 M. Nolan, V. S. Verdugo and H. Metiu, *Surf. Sci.*, 2008, **602**, 2734.

224 F. Vindigni, M. Manzoli, A. Chiorino, T. Tabakova and F. Boccuzzi, *J. Phys. Chem. B*, 2006, **110**, 23329.

225 W. Deng and M. Flytzani-Stephanopoulos, *Angew. Chem., Int. Ed.*, 2006, **45**, 2285.

226 M. Manzoli, F. Boccuzzi, A. Chiorino, F. Vindigni, W. Deng and M. Flytzani-Stephanopoulos, *J. Catal.*, 2007, **245**, 308.

227 X. Wu, L. Senapati, S. K. Nayak, A. Selloni and M. Hajaligol, *J. Chem. Phys.*, 2002, **117**, 4010.

228 A. Fielicke, G. von Helden, G. Meijer, D. B. Pedersen, B. Simard and D. M. Rayner, *J. Am. Chem. Soc.*, 2005, **127**, 8416.

229 J. K. Edwards and G. J. Hutchings, *Angew. Chem., Int. Ed.*, 2008, **47**, 9192.

230 J. K. Edwards, S. J. Freakley, R. J. Lewis, J. C. Pritchard and G. J. Hutchings, *Catal. Today*, 2015, **248**, 3.

231 J. A. Lopez-Sanchez, N. Dimitraos, N. Glanville, L. Kesavan, C. Hammond, J. K. Edwards, A. F. Carley, C. J. Kiely and G. J. Hutchings, *Appl. Catal., A*, 2011, **391**, 400.

232 G. J. Hutchings, *Chem. Commun.*, 2008, 1133.

233 N. Gemo, P. Biasi, P. Canu, F. Menegazzo, F. Pinna, A. Samikannu, K. Kordas and T. Salmi, *Top. Catal.*, 2013, **56**, 540.

234 F. Menegazzo, P. Burti, M. Signoretto, M. Manzoli, S. Vankova, F. Boccuzzi, F. Pinna and G. Strukul, *J. Catal.*, 2008, **257**, 369.

235 G. Bernardotto, F. Menegazzo, F. Pinna, M. Signoretto, G. Cruciani and G. Strukul, *Appl. Catal., A*, 2009, **358**, 129.

236 G. Centi and S. Perathoner, *Catal. Today*, 2009, **143**, 145.

237 F. Menegazzo, M. Manzoli, M. Signoretto, F. Pinna and G. Strukul, *Catal. Today*, 2015, **248**, 18.

238 E. Ozensoy and D. W. Goodman, *Phys. Chem. Chem. Phys.*, 2004, **6**, 3765.

239 K. Wolter, O. Seiferth, J. Libuda, H. Kuhlenbeck, M. Bäumer and H.-J. Freund, *Surf. Sci.*, 1998, **402–404**, 428.

240 J. B. Giorgi, T. Schroeder, M. Bäumer and H.-J. Freund, *Surf. Sci.*, 2002, **498**, L71.

241 C. Morterra, V. Bolis, B. Fubini and L. Orio, *Surf. Sci.*, 1991, **251–252**, 540.

242 T. Schalow, B. Brandt, M. Laurin, S. Schauermann, S. Guimond, H. Kuhlenbeck, J. Libuda and H. J. Freund, *Surf. Sci.*, 2006, **600**, 2528.

243 J. A. Hinojosa, H. H. Kan and J. F. Weaver, *J. Phys. Chem. C*, 2008, **112**, 8324.

244 E. A. Sales, J. Jove, M. de Jesus Mendes and F. Bozon-Verduraz, *J. Catal.*, 2000, **195**, 88.

245 J. A. Rodriguez, *Prog. Surf. Sci.*, 2006, **81**, 141.

246 D. Yuan, X. Gong and R. Wu, *Phys. Rev. B: Condens. Matter Mater. Phys.*, 2008, **78**, 035441.

247 L. Ouyang, P. Tian, G. Da, X. Xu, C. Ao, T. Chen, R. Si, J. Xu and Y. Han, *J. Catal.*, 2015, **321**, 70.

248 J. K. Edwards, A. F. Carley, A. A. Herzing, C. J. Kiely and G. J. Hutchings, *Faraday Discuss.*, 2008, **138**, 225.

249 J. K. Edwards, S. J. Freakley, A. F. Carley, C. J. Kiely and G. J. Hutchings, *Acc. Chem. Res.*, 2014, **47**, 845.

250 F. Menegazzo, M. Signoretto, M. Manzoli, F. Boccuzzi, G. Cruciani, F. Pinna and G. Strukul, *J. Catal.*, 2009, **268**, 122.

251 A. Villa, D. Ferri, S. Campisi, C. E. Chan-Thaw, Y. Lu, O. Kröcher and L. Prati, *ChemCatChem*, 2015, **7**, 2534.

252 P. Kaminski, M. Ziolek, B. Campo and M. Daturi, *Catal. Today*, 2015, **243**, 218.

253 A. Villa, G. M. Veith, D. Ferri, A. Weidenkaff, K. A. Perry, S. Campisi and L. Prati, *Catal. Sci. Technol.*, 2013, **3**, 394.

254 G. C. Bond, *Molecules*, 2012, **17**, 1716.

255 O. D. Gonzales and G. Parravano, *J. Am. Chem. Soc.*, 1956, **78**, 4533.

256 T. Fukushima, S. Galvagno and G. Parravano, *J. Catal.*, 1979, **57**, 177.

257 H. Berndt, I. Pitsch, S. Evert, K. Struve, M.-M. Pohl, J. Radnik and A. Martin, *Appl. Catal., A*, 2003, **244**, 169.

258 A. G. Shastri and J. Schwank, *J. Catal.*, 1985, **95**, 271.

259 S. S. Pansare, A. Sirijaruphan and J. G. Goodwin Jr., *J. Catal.*, 2005, **234**, 151.

260 E. Bus, J. T. Miller and J. A. van Bokhoven, *J. Phys. Chem. B*, 2005, **109**, 14581.

261 M. Boronat, P. Concepción, A. Corma, S. González, F. Illas and P. Serna, *J. Am. Chem. Soc.*, 2007, **129**, 16230.

262 S. Lin and M. A. T. Vannice, *Catal. Lett.*, 1991, **10**, 47.

263 J. Jia, K. Haraki, J. N. Kondo, K. Domen and K. Tamaru, *J. Phys. Chem. B*, 2000, **104**, 11153.

264 A. G. Shastri, A. K. Datye and J. Schwank, *J. Catal.*, 1984, **87**, 265.

265 Y. Iizuka, H. Fujiki, N. Yamauchi, T. Chijiiwa, S. Arai, S. Tsubota and M. Haruta, *Catal. Today*, 1997, **36**, 115.

266 J. L. Margitfalvi, A. Fasi, M. Hegedus, F. Lonyi, S. Gobolos and N. Bogdanchikova, *Catal. Today*, 2002, **72**, 157.

267 J. A. Rodriguez, J. Dvorak, T. Jirsak, G. Liu, J. Hrbek, Y. Aray and C. Gonzalez, *J. Am. Chem. Soc.*, 2003, **125**, 276.

268 J. Gottschalck and B. Hammer, *J. Chem. Phys.*, 2002, **116**, 784.

269 S. Vericat, M. E. Vela, G. Andreasen, R. C. Salvarezza, L. Vazquez and J. A. Martin-Gago, *Langmuir*, 2001, **17**, 4919.

270 R. G. Nuzzo, B. R. Zegarski and L. H. Dubois, *J. Am. Chem. Soc.*, 1987, **109**, 733.

271 G. Liu, J. A. Rodriguez, J. Dvorak, J. Hrbek and T. Jirsak, *Surf. Sci.*, 2002, **505**, 295.

272 J. C. Love, L. A. Estroff, J. K. Kriebel, R. G. Nuzzo and G. M. Whitesides, *Chem. Rev.*, 2005, **105**, 1103.

273 B. Panthi, A. Mukhopadhyay, L. Tibbitts, J. Saavedra, C. J. Pursell, R. M. Rioux and B. D. Chandler, *ACS Catal.*, 2015, **5**, 2232.

274 H. L. Abbott, A. Aumer, Y. Lei, C. Asokan, R. J. Meyer, M. Sterrer, S. Shaikhutdinov and H.-J. Freund, *J. Phys. Chem. C*, 2010, **114**, 17099.

275 S. Shaikhutdinov, M. Heemeier, J. Hoffmann, I. Meusel, B. Richter, M. Bäumer, H. Kuhlenbeck, J. Libuda, H.-J. Freund, R. Oldman, S. D. Jackson, C. Konvicka, M. Schmid and P. Varga, *Surf. Sci.*, 2002, **501**, 270.

276 X. P. Xu and D. W. J. Goodman, *J. Phys. Chem.*, 1993, **97**, 7711.

277 W.-Y. Yu, G. M. Mullen and C. B. Mullins, *J. Phys. Chem. C*, 2013, **117**, 19535.

278 M. Pan, D. W. Flaherty and C. B. Mullins, *J. Phys. Chem. Lett.*, 2011, **2**, 1363.

279 Z. J. Behm, *Z. Phys. Chem.*, 2009, **223**, 9.

280 J. W. Niemantsverdriet, *Spectroscopy in Catalysis*, Wiley-VCH, 2007, ISBN: 970-3-527-31651-9.

281 F. Fan, Z. Feng and C. Li, *Chem. Soc. Rev.*, 2010, **39**, 4794.

282 A. Smekal, *Naturwissenschaften*, 1923, **11**, 873.

283 G. Landsberg and L. Mandelstam, *Naturwissenschaften*, 1928, **16**, 557.

284 I. E. Wachs and C. A. Roberts, *Chem. Soc. Rev.*, 2010, **39**, 5002.

285 H. Knözinger and G. Mestl, *Top. Catal.*, 1999, **8**, 45.

286 J. F. Haw, *In Situ Spectroscopy in Heterogeneous Catalysis*, Wiley-VCH, 2002, ISBN: 3-52730248-4.

287 H. Kim, K. M. Kosuda, R. P. Van Duyne and P. C. Stair, *Chem. Soc. Rev.*, 2010, **39**, 4820.

288 S. Schlücker, *Angew. Chem.*, 2014, **53**, 4756.

289 C. E. Harvey and B. M. Weckhuysen, *Catal. Lett.*, 2015, **145**, 40.

290 B. S. Yeo and A. T. Bell, *J. Am. Chem. Soc.*, 2011, **133**, 5587.

291 B. S. Yeo and A. T. Bell, *J. Phys. Chem. C*, 2012, **116**, 8394.

292 A. C. Ferrari and J. Robertson, *Phys. Rev. B: Condens. Matter Mater. Phys.*, 2001, **64**, 1.

293 M. S. Dresselhaus, G. Dresselhaus, R. Saito and A. Jorio, *Phys. Rep.*, 2005, **409**, 47.

294 Q. Cheng, J. Tang, J. Ma, H. Zhang, N. Shinya and L.-C. Qin, *Phys. Chem. Chem. Phys.*, 2011, **13**, 17615.

295 A. K. Geim, *Science*, 2009, **324**, 1530–1534.

296 A. K. Geim, *Nat. Mater.*, 2007, **6**, 183.

297 E. T. Thostenson, Z. Ren and T. W. Chou, *Comp. Sci. Technol.*, 2001, **61**, 1899.

298 J. P. Tessonnier, D. Rosenthal, T. W. Hanse, C. Hess, M. E. Schuster, R. Blume, F. Girgsdies, N. Pfänder, O. Timpe, D. S. Su and R. Schlögl, *Carbon*, 2009, **47**, 1779.

299 A. P. Kozlova, S. Sugiyama, A. I. Kozlov, H. Asahura and Y. Iwasawa, *J. Catal.*, 1998, **176**, 426.

300 H. Zhu, Z. Pan, B. Chen, B. Lee, S. M. Mahurin, S. H. Overbury and S. Dai, *J. Phys. Chem. B*, 2004, **108**, 20038.

301 D. Andreeva, T. Tabakova, L. Ilieva, A. Naydenov, D. Mehanjiev and M. V. Abrashev, *Appl. Catal., A*, 2001, **209**, 291.

302 D. Andreeva, R. Nedyalkova, L. Ilieva and M. V. Abrashev, *Appl. Catal., A*, 2003, **246**, 29.

303 D. Andreeva, R. Nedyalkova, L. Ilieva and M. V. Abrashev, *Appl. Catal., B*, 2004, **52**, 157.

304 D. Andreeva, I. Ivanov, L. Ilieva and M. V. Abrashev, *Appl. Catal., A*, 2006, **302**, 127.

305 S. Carrettin, Y. Hao, V. Aguilar-Guerrero, B. C. Gates, S. Trasobares, J. J. Calvino and A. Corma, *Chem. – Eur. J.*, 2007, **13**, 7771.

306 Y. Lee, G. He, A. J. Akey, R. Si, M. Flytzani-Stephanopoulos and I. P. Herman, *J. Am. Chem. Soc.*, 2011, **133**, 12952.

307 W. Y. Hernandez, F. Romero-Sarria, M. A. Centeno and J. A. Odriozola, *J. Phys. Chem. C*, 2010, **114**, 10857.

308 M. G. Sanchez and G. L. Gazquez, *J. Catal.*, 1987, **104**, 120.

309 O. H. Laguna, A. Perez, M. A. Centeno and J. A. Odriozola, *Appl. Catal., B*, 2015, **176–177**, 386.

310 H. Yang, D. Tang, X. Lu and Y. Yuan, *J. Phys. Chem. C*, 2009, **113**, 8186.

311 L. Li, A. Wang, B. Qiao, J. Lin, Y. Huang, X. Wang and T. Zhang, *J. Catal.*, 2013, **299**, 90.

312 M. Li, Z. Wu, Z. Ma, V. Schwartz, D. R. Mullins, S. Dai and S. H. Overbury, *J. Catal.*, 2009, **266**, 98.

313 J. A. Lopez-Sanchez, N. Dimitratos, C. Hammond, G. L. Brett, L. Kesavan, S. White, P. Miedziak, R. Tiruvalam, R. L. Jenkins, A. F. Carley, D. Knight, C. J. Kiely and G. J. Hutchings, *Nat. Chem.*, 2011, **3**, 551.

314 S. M. Ansar, F. S. Ameer, W. Hu, S. Zou, C. U. Pittman Jr. and D. Zhang, *Nano Lett.*, 2013, **13**, 1226.

315 R. Zanella, L. Delannoy and C. Louis, *Appl. Catal., A*, 2005, **291**, 62.

316 L. Delannoy, N. El Hassan, A. Musi, N. N. L. To, J.-M. Krafft and C. Louis, *J. Phys. Chem. B*, 2006, **110**, 22471.

317 K. N. Heck, B. G. Janesko, G. E. Scuseria, N. J. Halas and M. S. Wong, *J. Am. Chem. Soc.*, 2008, **130**, 16592.

318 K. N. Heck, B. G. Janesko, G. E. Scuseria, N. J. Halas and M. S. Wong, *ACS Catal.*, 2013, **3**, 2430.

319 V. Joseph, C. Engelbrekt, J. Zhang, U. Gernert, J. Ulstrup and J. Kneipp, *Angew. Chem.*, 2012, **51**, 7592.

320 J. Huang, Y. Zhu, M. Lin, Q. Wang, L. Zhao, Y. Yang, K. X. Yao and Y. Han, *J. Am. Chem. Soc.*, 2013, **135**, 8552.

321 T. Mallat and A. Baiker, *Catal. Today*, 1994, **19**, 247.

322 M. Besson and P. Gallezot, *Catal. Today*, 2000, **57**, 127.

323 F. Cavani, *J. Chem. Technol. Biotechnol.*, 2010, **85**, 1175.

324 T. Mallat and A. Baiker, *Chem. Rev.*, 2004, **104**, 3037.

325 T. Matsumoto, M. Ueno, N. Wang and S. Kobayashi, *Chem. – Asian J.*, 2008, **3**, 196.

326 C. P. Vinod, K. Wilson and A. F. Lee, *J. Chem. Technol. Biotechnol.*, 2011, **86**, 161.

327 J. M. Campelo, D. Luna, R. Luque, J. M. Marinas and A. A. Romero, *ChemSusChem*, 2009, **2**, 18.

328 T. Balcha, J. R. Strobl, C. Fowler, P. Dash and R. W. J. Scott, *ACS Catal.*, 2011, **1**, 425.

329 N. Dimitratos, J. A. Lopez-Sanchez and G. J. Hutchings, *Chem. Sci.*, 2012, **3**, 20.

330 L. Prati and A. Villa, *Acc. Chem. Res.*, 2014, **47**, 855.

331 L. C. Lee, C. Xiao, W. Huang and Y. Zhao, *New J. Chem.*, 2015, **39**, 2459.

332 R. W. J. Scott, *Can. J. Chem. Eng.*, 2015, **93**, 623.

333 D. Nepak and S. Darbha, *Catal. Commun.*, 2015, **58**, 149.

334 L. T. Murciano, T. Villager and D. Chatwick, *ChemCatChem*, 2015, **7**, 925.

335 B. Puertolas, A. K. Hill, T. Garcia, B. Solsona and L. T. Murciano, *Catal. Today*, 2015, **248**, 115.

336 Y. Yu, B. Lu, X. Wang, J. Zhao, X. Wang and Q. Cai, *Chem. Eng. J.*, 2010, **162**, 738.

337 V. R. Choudhary, P. A. Chaudhari and S. V. Narkhede, *Catal. Commun.*, 2003, **4**, 171.

338 D. I. Enache, J. K. Edwards, P. Landon, B. Solsona-Espriu, A. F. Carley, A. A. Herzing, M. Watanabe, C. J. Kiely, D. W. Knight and G. J. Hutchings, *Science*, 2006, **311**, 362.

339 D. I. Enache, D. Barker, J. K. Edwards, S. H. Taylor, D. W. Knight, A. F. Carley and G. J. Hutchings, *Catal. Today*, 2007, **122**, 407.

340 J. A. Lopez-Sanchez, N. Dimitratos, P. Miedziak, E. Ntainjua, J. K. Edwards, D. Morgan, A. F. Carley, R. Tiruvalam, C. J. Kiely and G. J. Hutchings, *Phys. Chem. Chem. Phys.*, 2008, **10**, 1921.

341 N. Dimitratos, J. A. Lopez-Sanchez, J. M. Anthonykutty, G. Brett, A. F. Carley, R. C. Tiruvalam, A. A. Herzing, C. J. Kiely, D. W. Knight and G. J. Hutchings, *Phys. Chem. Chem. Phys.*, 2009, **11**, 4952.

342 N. Dimitratos, A. Villa, D. Wang, F. Porta, D. Su and L. Prati, *J. Catal.*, 2006, **244**, 113.

343 A. Villa, N. Janjic, P. Spontoni, D. Wang, D. S. Su and L. Prati, *Appl. Catal., A*, 2009, **364**, 221.

344 J. Pritchard, L. Kesavan, M. Piccinini, Q. He, R. Tiruvalam, N. Dimitratos, J. A. Lopez-Sanchez, A. F. Carley, J. K. Edwards, C. J. Kiely and G. J. Hutchings, *Langmuir*, 2010, **26**, 16568.

345 S. Meenakshisundaram, E. Nowicka, P. J. Miedziak, G. L. Brett, R. L. Jenkins, N. Dimitratos, S. H. Taylor, D. W. Knight, D. Bethell and G. J. Hutchings, *Faraday Discuss.*, 2010, **145**, 341.

346 M. Sankar, E. Nowicka, R. Tiruvalam, Q. He, S. H. Taylor, C. J. Kiely, D. Bethell, D. W. Knight and G. J. Hutchings, *Chem. – Eur. J.*, 2011, **17**, 6524.

347 E. Cao, M. Sankar, E. Nowicka, Q. He, M. Morad, P. J. Miedziak, S. H. Taylor, D. W. Knight, D. Bethell, C. J. Kiely, A. Gavriilidis and G. J. Hutchings, *Catal. Today*, 2013, **203**, 146.

348 J. Pritchard, M. Piccinini, R. Tiruvalam, Q. He, N. Dimitratos, J. A. Lopez-Sanchez, D. J. Morgan, A. F. Carley, J. K. Edwards, C. J. Kiely and G. J. Hutchings, *Catal. Sci. Technol.*, 2013, **3**, 308.

349 S. Marx and A. Baiker, *J. Phys. Chem. C*, 2009, **113**, 6191.

350 C. Y. Ma, B. J. Dou, J. J. Li, J. Cheng, Q. Hu, Z. P. Hao and S. Z. Qiao, *Appl. Catal., B*, 2009, **92**, 202.

351 Y. T. Chen, H. M. Lim, Q. H. Tang, Y. T. Gao, T. Sun, Q. Y. Yan and Y. H. Yang, *Appl. Catal., A*, 2010, **380**, 55.

352 C. Evangelisti, E. Schiavi, L. A. Aronica, A. M. Caporusso, G. Vitulli, L. Bertinetti, G. Martra, A. Balerma and S. Mobilio, *J. Catal.*, 2012, **286**, 224.

353 A. M. Henning, J. Watt, P. J. Miedziak, S. Cheong, M. Santonastaso, M. H. Song, Y. Takeda, A. I. Kirkland, S. H. Taylor and R. D. Tilley, *Angew. Chem., Int. Ed.*, 2013, **52**, 1477.

354 M. Sankar, Q. He, M. Morad, J. Pritchard, S. J. Freakley, J. K. Edwards, S. H. Taylor, D. J. Morgan, A. F. Carley, D. W. Knight, C. J. Kiely and G. J. Hutchings, *ACS Nano*, 2012, **6**, 6600.

355 M. Morad, M. Sankar, E. Cao, E. Nowicka, T. E. Davies, P. J. Miedziak, D. J. Morgan, D. W. Knight, D. Bethell, A. Gavriilidis and G. J. Hutchings, *Catal. Sci. Technol.*, 2014, **4**, 3120.

356 G. Wu, A. Constantinou, E. Cao, S. Kuhn, M. Morad, M. Sankar, D. Bethell, G. J. Hutchings and A. Gavriilidis, *Ind. Eng. Chem. Res.*, 2015, **54**, 4183.

357 T. A. G. Silva, E. T-Neto, N. Lopez and L. M. Rossi, *Sci. Rep.*, 2014, **4**, 5766.

358 Y. Hong, X. Jing, J. Huang, D. Sun, T. O-Wubah, F. Yang, M. Du and Q. Li, *ACS Sustainable Chem. Eng.*, 2014, **2**, 1752.

359 D. Sun, G. Zhang, X. Jiang, J. Huang, X. Jing, Y. Zheng, J. He and Q. Li, *J. Mater. Chem. A*, 2014, **2**, 1767.

360 T. Jiang, C. Jia, L. Zhang, S. He, Y. Sang, H. Li, Y. Li, X. Yu and H. Liu, *Nanoscale*, 2015, **7**, 209.

361 H. Zou, R. Wang, J. Dai, Y. Wang, X. Wang, Z. Zhang and S. Qiu, *Chem. Commun.*, 2015, **51**, 14601.

362 H. Wang, C. Wang, H. Yan, H. Yi and J. Lu, *J. Catal.*, 2015, **324**, 59.

363 J. Wang, S. A. Kondrat, Y. Wang, G. L. Brett, C. Giles, J. K. Bartley, L. Lu, Q. Liu, C. J. Kiely and G. J. Hutchings, *ACS Catal.*, 2015, **4**, 3575.

364 J. Schnadt, J. Knudsen, J. N. Andersen, H. Siegbahn, A. Pietzsch, F. Hennies, N. Johansson, N. Martensson, G. Ohrwall, S. Bahr, S. Mahld and O. Schaff, *J. Synchrotron Radiat.*, 2012, **19**, 701.